Microwave Brightness Temperature and its Relation to Atmospheric General circulation Features

By
Theodore T. Vroman and Graeme L. Stephens

Department of Atmospheric Science
Colorado State University
Fort Collins, Colorado

Research supported by NSF grant ATM-8617856

Paper No. 545

Microwave Brightness Temperature and its Relation to Atmospheric General Circulation Features

by Theodore T. Vroman and Graeme L. Stephens

NSF Grant ATM-8617856

454

ABSTRACT

Microwave Sounding Unit (MSU) global brightness temperature fields are compared with observed atmospheric general circulation features for the purpose of determining the extent to which MSU brightness temperature relates to observed atmospheric circulation. A six-week MSU data set covering 8 Jan 87 – 18 Feb 87 is analyzed. Global and hemispheric projections of MSU Channel 2 (53.74 GHz), Channel 3 (54.96 GHz), and Channel 4 (57.95 GHz) brightness temperature fields are presented in two divisions; 8-31 Jan and 1- 18 Feb 87. Complementary data sets of temperature, zonal wind, geopotential height, and streamfunction are developed using model analyses from the European Centre for Medium Range Weather Forecasts (ECMWF) and the National Meteorological Center (NMC) for the purpose of a comparative study. MSU thermal fields may be considered an estimate of atmospheric mean-layer temperature through levels determined by each channel's weighting function. Using thermal wind theory MSU meridional temperature gradients are shown related to zonal wind, geopotential height, and steamfunction fields. Results of pattern comparison and random numerical calculations show MSU thermal fields give a unique insight into atmospheric general circulations. The MSU observations are also shown to provide important information about the lower stratospheric thermal structure. Specifically, MSU Channels 3 and 4 detected a warming northward of 50°N between the 8-31 Jan and 1-18 Feb data sets. This warming was also detected in the ECMWF data sets and at higher levels in the NMC data. Applications of this research for the future may include weather and climate model initialization and verification.

ACKNOWLEDGEMENTS

We wish to acknowledge various people who have contributed in different ways to this research. Among those are Dr. James Purdom, Dr. Paul Mielke, and Dr. Thomas Vonder Haar for their participation and evaluation of this paper.

Takmeng Wong has also worked with Microwave Sounding Unit data and provided many helpful programming suggestions for interfacing with the NCAR Graphics System. We would also like to thank Deb Lubich for her assistance in obtaining the MSU data set and her interest through all phases of this study. We also gratefully acknowledge the efforts of Sue Lini, who helped in preparing this paper.

This research was supported by the Atmospheric Sciences Section of the National Science Foundation under Contract ATM-8617856.

TABLE OF CONTENTS

1. INTRODUCTION

2. MICROWAVE RADIATION AND THE MICROWAVE SOUNDING UNIT

3. ECMWF ANALYSIS FIELDS

4. COMPARISON OF MSU FIELDS WITH OBSERVED CIRCULATIONS

5. **SUMMARY, CONCLUSIONS, AND RECOMMENDATIONS**

LIST OF FIGURES

LIST OF TABLES

CHAPTER 1

INTRODUCTION

1.1 BACKGROUND

Microwave observations of the earth's emitted radiation are a valuable tool for studying various properties of the earth's surface and atmosphere on a global basis. Since the first microwave radiometer was flown aboard the planetary mission Mariner 2 in 1962, microwave instruments have evolved into a powerful technique for remote sensing of the earth's surface characteristics through imagers, and the atmosphere's thermal and moisture structure through sounders. An interesting history of microwave radiometry on spacecraft was prepared by Njoku, 1982. Passive microwave remote sensing offers distinct advantages over measurements taken in the visible and infrared wavelengths. The unique ability of microwave radiation to penetrate most clouds with little attenuation (with the exception of large cloud droplets and rain), makes microwave remote sensing a near weather-independent measurement technique. Microwave radiation provides the satellite based technique for remote sensing of atmospheric temperature in the presence of clouds. The Microwave Sounding Unit (MSU) was designed primarily as an atmospheric temperature sounder to provide soundings in the presence of clouds. For example, Kidder, 1979 used MSU data to measure upper tropospheric temperature anomalies to infer tropical cyclone surface pressure and winds. Lubich and Zehr, 1988 also used MSU brightness temperature data to study the vertical temperature structure of tropical storms in cloud cluster regions. Grody and Shen, 1982, studied Hurricane David (1979) using MSU brightness temperature measurements with the aim of distinguishing precipitating from non-preciptating areas. Grody, 1983 also used MSU data with the objective of distinguishing precipitating from non-preciptating regions by studying the thermal structure of convective storms over the central United States. The MSU was first flown aboard the polar-orbiting Tiros-N satellite launched in 1978, and since has flown on the NOAA A-G polar-orbiting series. Thus, the MSU data set currently provides an extensive record of radiometric data that may help to reveal the thermal structure of the atmosphere day or night on a global or regional basis, even in the presence of clouds.

Microwave Sounding Unit observations measure the emission from different layers in the atmosphere, the altitude of which depends on frequency. These emissions are a result of line absorption and emission from molecular oxygen at four frequencies (channels) in the 5-mm wavelength region. Channel 1 (50.30 GHz) is highly transparent and largely measures the surface emission, Channel 2 (53.74 GHz) senses the lower troposphere, Channel 3 (54.96 GHz) the upper troposphere, and Channel 4 (57.95) the lower stratosphere. The time invariant and near uniform mixing ratio of molecular oxygen through the troposphere (Liou, 1980) allows opportunity for estimations of atmospheric temperature profiles from the 50-60 GHz region, (Staelin, 1969). Thus the atmospheric temperature measurements from the MSU provides a unique view of the broad thermal structure of the troposphere and lower stratosphere on a global scale. A knowledge of global atmospheric temperature fields from the MSU may also reveal many general circulation features in the atmosphere, and provide an analysis tool for current research in global climate trend studies. In the future, the Advanced Microwave Sounding Unit (AMSU) will offer better vertical resolution (11 channels in the 50 - 60 GHz oxygen band), however this instrument is not expected to fly until the mid 1990's (Murphy, 1987). Thus, for most of the next decade the MSU will provide a unique data set for studies of the global atmosphere.

1.2 STATEMENT AND SCOPE OF PROBLEM

Computer models which simulate the present state and future motion of the atmosphere and climate are continually being modified with theoritical and computer engineering advances. The numerical modeling of weather and climate is one of the fastest growing disciplines in the atmospheric sciences today. Even with the incorporation of the best available physics and mathematics, a model can only be sucessful in predicting the future by first sucessfully capturing the initial state of the atmosphere and by second having a high confidence data set for verification purposes. Microwave thermal data may perhaps contribute in part to both needs. It not only offers a source of initialization for climate models, but can also be of tremendous value for verification purposes. MSU data sets can provide a global data collection system for numerical weather prediction interests. Vast regions of the globe are covered by poor or non-existent data collection systems. Oceans cover 81 percent of the southern hemisphere and 61 percent of the northern hemisphere (Sellers, 1965). Satellite remote sensing appears to be the solution to meteorological data collection problems both temporally and spatially, with microwaves providing the capability of an all-weather look into the atmosphere's thermal structure.

The principle quest of this study is to determine the extent to which MSU brightness temperature measurements relate to gross characteristics of atmospheric circulation. Surface emissivity is an important term in the microwave radiative transfer equation, we wish to determine what effect it has on MSU brightness temperature measurements from the various channels. Since MSU brightness temperature is essentially a vertically integrated or mean-layer temperature, to what extent does it relate to ECMWF observed zonal wind, geopotential, and streamfunction fields? Are lower stratospheric phenomenon detectable using MSU? Answers to these questions may show whether MSU data has the ability to discern circulations characteristics in the earth's atmosphere and the capability to provide model initialization and verification information.

1.3 RESEARCH OBJECTIVES AND STRUCTURE OF THIS THESIS

The objectives of this study were three-fold:

- First, to develop a method and produce global brightness temperature fields from MSU radiometric data available on magnetic tape. 8 January - 18 February 1987 was chosen as the test-case period due to the immediate availability of the MSU data set through the Cooperative Institute for Research in the Atmosphere (CIRA) at Colorado State University. Chapter 2 covers this objective in three parts. First, a discussion of microwave radiative transfer including the derivation of brightness temperature is presented. Second, the Microwave Sounding Unit is discussed; its satellite platform, instrument operation, along with the conversion procedure used to obtain a brightness temperature value from raw thermal data counts. Lastly, Chapter 2 includes the methods developed to process MSU brightness temperature files into global fields and presents samples of MSU Channels 2, 3, and 4. Processing and displaying brightness temperature fields in this time-averaged global format is a relatively new approach to application of MSU data.

- The second objective was to compile a complementary set of meteorological observations of the earth's atmosphere for a comparative study designed to identify if general circulation features such as tropospheric wind and thermal patterns were reflected in MSU thermal fields. Model analyses from the European Centre for Medium Range Weather Forecasts (ECMWF) provide an observational data set to compare with MSU brightness temperature fields. ECMWF global analyses from 1979-1987 are stored in numerical form on mass store at the National Center for Atmospheric Research (NCAR) in Boulder, CO., (Trenberth and Olson, 1988). Analysis data sets are available at 1000, 850, 700, 500, 300, 200, and 100 mb levels. The ECMWF data sets are organized to run on the NCAR Community Climate Model (CCM) Processor, a software package designed at NCAR (Wolski, 1987), which performs user-specified functions, such as time-averaging. Processor results can be displayed in either numerical or graphical form. ECMWF analyses combined with the capabilities of the CCM Processor, allowed the opportunity to temporally and spatially match ECMWF data with available MSU data sets for a comparative study.

Chapter 3 discusses the development of ECMWF fields of temperature, zonal wind, geopotential height and thickness, and streamfunction for the periods of 8-31 Jan and 1-18 Feb. ECMWF fields provide a look at the climatology of the January and February months plus specific features that existed during 8 Jan -18 Feb 87, the time period coincident with the MSU data set. This study represents a pioneering effort to process ECMWF data sets from the mass store at NCAR for an observational study with passive microwave remote sensing data.

- The third objective was to determine the extent to which MSU brightness temperature fields relate to observed atmospheric circulations. This comparative study is presented as Chapter 4. The first comparison, Section 4.1, performed was between MSU brightness temperature fields for Channels 2, 3,and 4 and ECMWF temperature fields. MSU Channels 2, 3, and 4 thermal patterns are shown best represented by ECMWF temperature fields at 500, 300, and 100 mb, respectively. A second comparison was made between MSU meridional temperature gradients and ECMWF zonal wind based on the thermal wind concept. MSU brightness temperature fields are assumed to be representative of mean-layer temperature of an atmospheric layer determined by the channel's weighting function. ECMWF zonal wind fields are shown to be proportional to MSU meridional temperature gradients as presented in Section 4.3 To further investigate this relationship MSU temperature anomaly fields were constructed in Section 4.4 in an effort to determine jet stream location using MSU brightness temperature fields. The jet stream is assumed to be located in the region where the sign of the MSU temperature gradient reverses. ECMWF zonal wind data is presented as a basis for evaluation for determining the MSU anomaly field's accuracy. Section 4.5 extends the thermal wind concept to a comparison between ECMWF geopotential thickness gradient and MSU brightness temperature gradient. Since both are related to mean-layer temperature pattern, correlation between fields should be evident. Likewise, the MSU thermal field itself should be representative of ECMWF geopotential thickness. MSU brightness temperature fields are also compared to ECMWF derived streamfunction fields in Section 4.6. Results of the comparisons in Chapter 4 show excellent correlations between MSU and atmospheric circulation properties, and demonstrate the potential of MSU thermal data for studying the global general circulation of the atmosphere.

One unexpected finding during the analysis of the MSU data sets provided an interesting extra topic for investigation. Section 4.7 discusses a northern hemispheric warming observed above 50^{o} latitude between the 8-31 Jan and 1-18 Feb data sets. ECMWF data up to 100 mb and stratospheric NMC data are used to determine if a stratospheric warming may have occured during this period. Most of MSU Channel 4 and portions of Channel 3's weighting function are located in the lower stratosphere.

This thesis concludes by summarzing the results of comparisons between MSU and ECMWF fields in Chapter 5. Recommendations are also presented for anyone considering further study of topics discussed in this thesis, or anyone working with the MSU data set in another application.

Chapter 2

MICROWAVE RADIATION AND THE MICROWAVE SOUNDING UNIT

2.1 INTRODUCTION

The application of radiometric information from the microwave region of the electromagnetic spectrum to research studies in the atmospheric sciences has greatly increased in the last decade. The ability of microwaves to penetrate clouds provides atmospheric scientists with a unique look into the earth's atmospheric structure in and around cloud systems. The breadth of possible uses of microwave remote sensing information has recently becoming realized. The inclusion of the High Resolution Multifrequency Microwave Radiometer aboard NASA's future Earth Observing System for the 1990's is evidence of this realization. Several of its suggested applications include measuring soil moisture content, snow depth, sea surface temperature, sea ice extent and age, sea surface wind speed, atmospheric water vapor and temperature profiles, and the detection of precipitating cloud systems.

This chapter reviews some fundamentals of microwave radiative transfer and overviews the Microwave Sounding Unit (MSU), from which brightness temperature fields were obtained for this study. The concept of thermal radiation, a review of the radiative transfer equation applied in the microwave region, and a discussion of the effects of the atmosphere and surface on radiative transfer are contained in Section 2.2. The Microwave Sounding Unit was carried aboard the TIROS-N/NOAA A-G satellite series beginning in 1978. A brief review of this polar-orbiting satellite series is provided in Section 2.3. In Section 2.4, the scan, antenna, and radiometer systems of the Microwave Sounding Unit are discussed along with a summary of MSU radiometric data- calibration and conversion methods. The final section, Section 2.5, contains a collection of brightness temperature fields derived from the MSU data sets. It includes data preparation and mapping methods, and presents the resulting MSU temperature fields.

2.2 MICROWAVE RADIATIVE TRANSFER

The emission of electromagnetic radiation is the fundamental quantity measured by the Microwave Sounding Unit and is sensed in four spectral bands which coincide with an absorption band of molecular oxygen.

2.2.1 Thermal Radiation

Electromagnetic radiation is emitted by all substances with a finite absolute temperature. Molecules may absorb electromagnetic radiation and transition to a higher energy level, or emit radiation and transition to a lower energy level. The absorption-emission properties of a molecule can be represented by a line spectrum showing the frequencies where absorption-emission do and do not occur. In the microwave region (3-300 GHz), energy level changes tend to be small and associated with rotational changes (Goody and Walker, 1970). In the microwave region, thermal emission is the only source of radiation and is dependent on the absolute temperature of the substance as determined by the Planck function.

The relationship between absolute temperature and radiation emitted is given by Planck's Law for a hypothetical blackbody (a body which fully absorbs and emits in all parts of the electromagnetic spectrum), the Planck function written in wavenumber form (Chandrasekhar, 1960) is

$$B_v(T) = \frac{2hv^3}{c^2} \frac{1}{e^{\frac{hv}{\kappa T}} - 1} \tag{2.1}$$

where B_v is the spectral radiance at frequency v and absolute temperature T,

$k = 1.38 \times 10^{-23}$ J^oK^{-1} Boltzmann's Constant
$c = 3.0 \times 10^8$ ms^{-1} the speed of light, and
$h = 6.63 \times 10^{-34}$ Js^{-1} Planck's constant.

In the microwave region of 3 - 300 GHz (1 GHz = 10^9 cycles/sec, and 1 cm = 30 GHz) the Rayleigh-Jean's approximation, $hv/kT << 1$, can be applied to simplify Planck's Law. The resulting approximation is called the Rayleigh-Jean's law and is written as

$$B_v(T) = \left[\frac{2\kappa v^3}{c^2}\right]T \tag{2.2}$$

Equation 2.2 shows the relationship of blackbody spectral radiance to absolute temperature T as a linear function in the microwave region (Rayleigh-Jean's law), as shown in Figure 2.1. Rayleigh-Jean's law is shown to be a good approximation of Planck's law in the microwave region (10^8 thru 10^{12} Hz).

The radiometric quantity most commonly used in the analysis of microwave remote sensing data, and in this study, is equivalent brightness temperature.

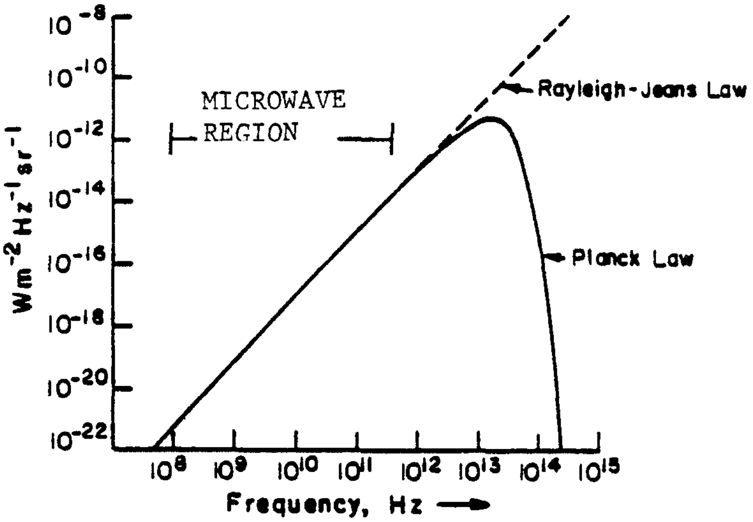

Figure 2.1: Comparison of Planck's law with Rayleigh-Jean's Law at T = 300 K (From Tsang et al., 1985).

According to Equation 2.2, equivalent brightness temperature is simply proportional to the intensity of radiation. Equation 2.3 shows this relation by expressing the radiance L_V emitted by a blackbody as a function of its absolute temperature

$$L_\nu(T)=\left[\frac{2\kappa\nu^3}{c^2}\right]T_B(\nu) \tag{2.3}$$

where T_B is hereafter refered to as the brightness temperature, and is a function of frequency.

2.2.2 The Radiative Transfer Equation

To better understand microwave remote sensing in the context of what the satellite instrumentation actually detects, a brief review of the solution of the radiative transfer equation in the microwave region is presented. Since only large cloud droplets and rain have attenuation cross-sections large enough to attenuate electromagnetic radiation in the microwave region significantly, a non-scattering atmosphere can generally be assumed. The solution of the radiative transfer equation under this assumption and that of local thermodynamic equilibrium, can be written in the form (Liou, 1980):

$$L_v(0) = L_v(p_s)T_v(p_s,0) + \int_{P_s}^{0} B_v[T(p)]\frac{\partial T_v(p,0)}{\partial P}dP \tag{2.4}$$

where v denotes the frequency, $L_v(0)$ represents outgoing radiance at the top of the atmosphere, $L_v(p_s)$ the radiance contribution from the surface, and $T_v(p,0)$ the transmittance from pressure level p to the top of the atmosphere. The radiance contribution from the surface results from two physical processes shown schematically in Figure 2.2, and mathmatically in Equation 2.5.

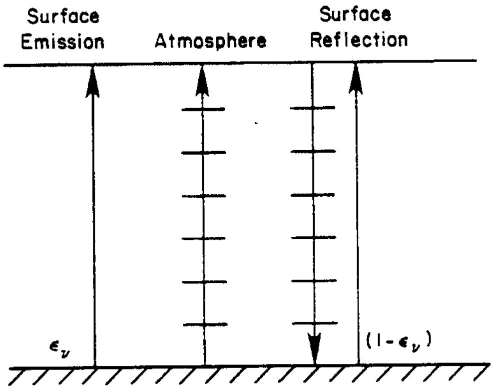

Figure 2.2: Contribution of radiance at the top of a clear atmosphere (From Liou, 1980).

$$L_v(p_s) = \varepsilon B_v(T_s)T_v(p_s,0) + (1-\varepsilon_v)\int_0^{p_s} B_v[T(p)]\frac{\partial T_v(p_s,p)}{\partial P}dP \tag{2.5}$$

The first term on the right-hand side of Equation 2.5 represents the surface emission contribution, while the second term represents emission from the atmosphere which is reflected by the surface back to the atmosphere. By substituting Equation 2.5 into 2.4 the reflection component can be seperated from the contributions by atmospheric emission, resulting in three contributions to upwelling radiance at the top of the atmosphere as defined in Equation 2.6.

The surface emission term is a product of surface emissivity, Planck radiance (a function of surface temperature), and atmospheric transmittance through the total atmosphere. The surface reflection term is a product of the surface reflectance ratio and the vertically integrated weighting function multiplied by the atmospheric temperature profile. The third radiance contribution to brightness temperature measured at the top of the atmosphere is the atmospheric emission term, a function of the atmospheric temperature profile and atmospheric transmittance from pressure level p to the top of the atmosphere. This term is also vertically integrated to obtain a total atmospheric contribution. By substituting the Rayleigh-Jean's law into this radiative transfer equation the expression for equivalent brightness temperature can be written (Liou, 1980):

$$T_B(\nu) = \varepsilon_\nu T_s T_\nu(p_s,0) + (1-\varepsilon)T_\nu(p_s,0)\int_0^{p_s} T(p)\frac{\partial T_\nu(p_s,p)}{\partial P}dP + \int_{P_s}^{0} T(p)\frac{\partial T_\nu(p,0)}{\partial P}dP \tag{2.6}$$

This relationship shows the three contributions to equivalent brightness temperature at the top of the atmosphere in mathematical form. Since $T_V(p_S,p) = T_V(p_S,0)/T_V(p,0)$ Equation 2.6 can be rewritten as (Liou, 1980):

$$T_B(\nu) = \varepsilon_\nu T_s T_\nu(p_s) + \int_{P_s}^{0} J_\nu(p)\frac{\partial T}{\partial P}dP \tag{2.7}$$

where the atmospheric source term is given by,

$$J_\nu(P) = \left\{1 + (1-\varepsilon_\nu)\left[\frac{T_\nu(p_s)}{T_\nu(p)}\right]^2\right\}T(P) \tag{2.8}$$

and where, $T_V(p_S)$ denotes transmission from the surface to the top of the atmosphere and $T_V(p)$ transmission from pressure p to the top of the atmosphere. The large variation of surface emissivity in the microwave region between dry and wet surfaces, vegated and non-vegetated surfaces has a significant effect on brightness temperature and should be considered in any data analysis.

2.2.3 Atmospheric and Surface Effects

Atmospheric gases and surface characteristics both have a significant effect on radiative transfer in the microwave region. Atmospheric gas molecules undergo energy level transitions upon interaction with electromagnetic radiation in the microwave region and subsequently influence the atmospheric emissions. Varying surface characteristics such as topography and moisture content also effect surface emissivity values.

Water vapor and molecular oxygen, as shown in Figure 2.3, are the two major atmospheric gases that affect transmission in the microwave region. The four channels of the Microwave Sounding Unit reside in that part of the spectrum that contains the 50 - 60 GHz (0.5 cm) oxygen absorption band.

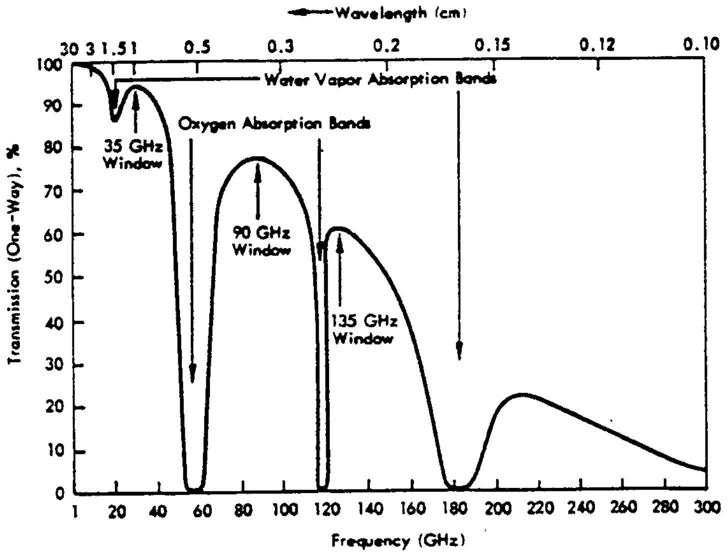

Figure 2.3: Percent Transmission through the Earth's Atmosphere, along the vertical, under clear sky conditions (Ulaby, 1981)

The absorption band of molecular oxygen near 60 GHz results from a rotational transition caused by a change in the spin orientation of its electrons. Another absorption line for molecular oxygen is shown near 120 GHz, and water vapor absorption lines occur near 31 and 183 GHz. Other microwave remote sensing instruments have taken advantage of these water vapor bands and "windows". For example, Prabhakara, et. al. 1982 and 1983, studied the remote sensing of precipitable water over the oceans, surface wind speed, sea surface temperature, and atmospheric liquid-water content using data from the Scanning Multichannel Microwave Radiometer (SMMR) flown on Nimbus-7.

Surface emissivity in the microwave region typically range from near unity over dry land to .6 over wet soils to .4 over ocean surfaces (Wang and Schmugge, 1980; Schmugge, 1985). Snow and ice surfaces in regions of elevated terrain also act to lower emissivity and consequently effect measurements from MSU Channel 2. Moisture content can act to lower soil emissivity values as low as .60, while the presence of ice or foam, or the degree of surface roughness alters ocean surface emissivity. Surface emissivity is contained in both the surface emission and surface reflection terms of Equation 2.6.

2.2.4 The Microwave Sounding Unit Weighting Function

The temperature weighting function defines the contribution of emission from different pressure levels to the observed brightness temperature. This weighting function can be expressed as

$$-\frac{dT_v(P)}{d(\ln P)} \tag{2.9}$$

The weighting function term is included in both atmospheric emission terms, the surface reflection and direct atmospheric emisson, of Equation 2.6. Figure 2.4 shows the MSU weighting function for its four channels (50.30, 53.74,54.96, and 57.95 GHz). The dashed lines show the weighting functions at the MSU scan limit along a path inclined 57° from satellite nadir angle, peaking higher in the atmosphere due to the longer observing path length. Solid lines show the weighting function overhead paths defined by a scan angle of 0°. The effect of angular scanning on the peak of the weighting function is given by (Grody, 1983),

$$P(\theta) = P(0^{\circ}) \times (\cos\theta)^{\frac{1}{2}} \tag{2.10}$$

where $P(0^{\circ})$ is the pressure at which the weighting function peaks at nadir, and theta is the scan angle. Surface emissivity effects are also shown for the lower channels, varying from near 1.0 for dry land and 0.5 for ocean surfaces.

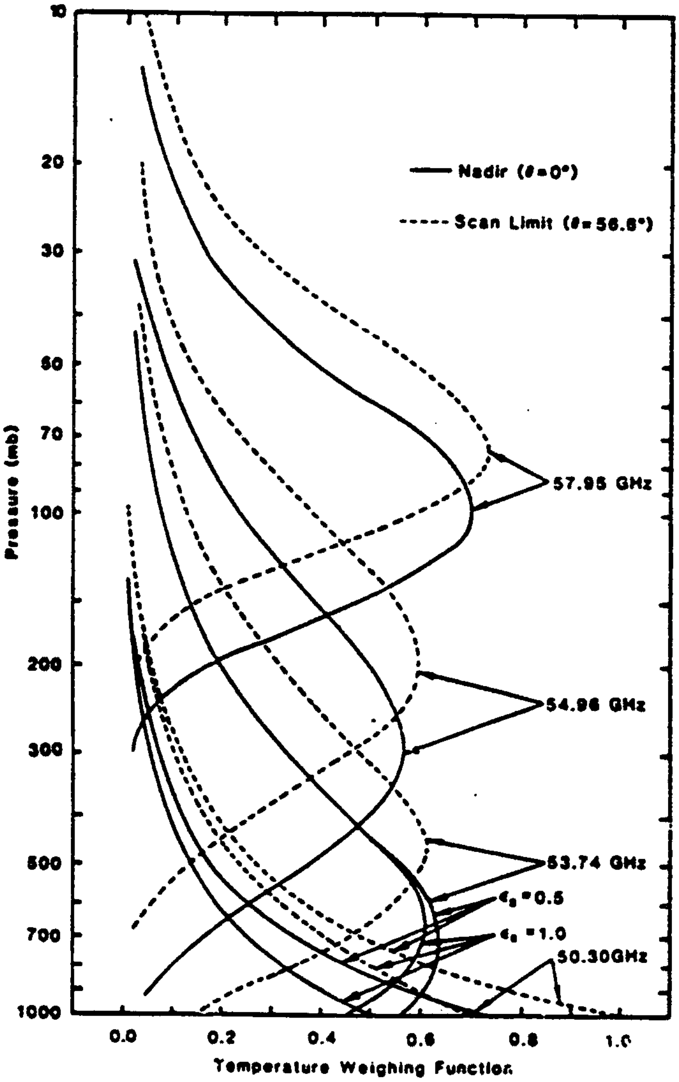

Figure 2.4: MSU Weighting Function at nadir and scan limit positions (From Grody, 1983).

2.3 MSU'S SATELLITE PLATFORM

The Microwave Sounding Unit (MSU) was first flown aboard TIROS-N, launched on October 13, 1978. The TIROS-N spacecraft system with the MSU attached is illustrated in Figure 2.5. Its communications and instrumentation systems are labeled. Since 1978, the microwave sounding unit has flown on all the current generation NOAA polar orbiting satellites (NOAA A/6 - G/10). The TIROS-N/NOAA A-G satellite series was designed and built by RCA Corporation, procured and operated by NOAA. MSU data used in this study was taken from NOAA-G/10. NOAA-G/10 was launched on September 17, 1986 and became operational November 17, 1986.

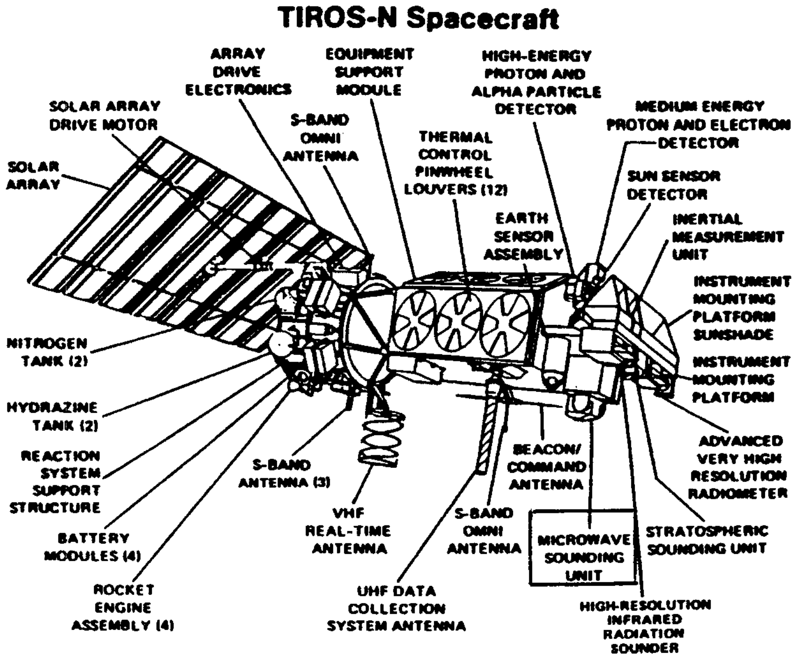

Figure 2.5: The TIROS-N Series Spacecraft (After Schwalb, 1978)

This satellite series operates in a near-polar, sun-synchronous orbit. Figure 2.6 shows the ground track of TIROS-N series for 2.5 orbits on December 31, 1979 progressing east to west. The ground track does not overlap on a daily basis to allow same daily time coverage of a region. However, it does cross similiar latitude lines at the same Local Solar Time (LST) allowing a diurnal division of data. NOAA G/10 crosses the equator at 1930 LST at its ascending node(northbound Equator crossing) and 0730 LST at its decending node (southbound Equator crossing).

The orbital period of TIROS-N/NOAA A-G satellites is approximately 102 minutes, resulting in 14.1 orbits per day. Orbit altitude is 833 km (450 n. mi.). A sub-orbital track and path swath locator can be constructed for this satellite series using directions in the NOAA Polar Oribiter Users Guide, (Kidwell, 1986).

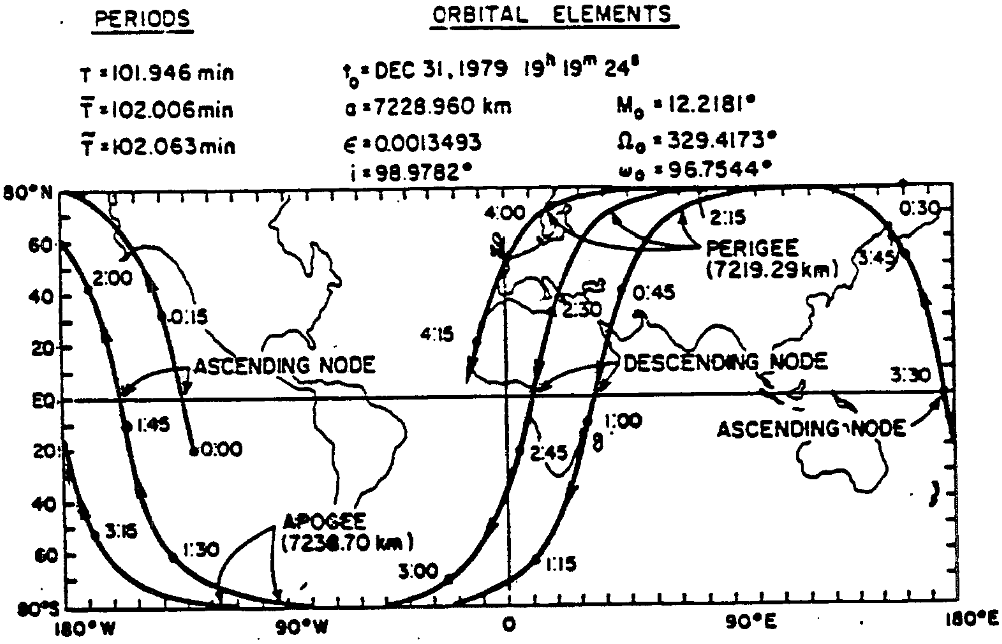

TIROS-N:2.5 ORBITS-DEC 31,1979
(• TIMES GIVEN IN GMT)

Figure 2.6: The Ground Track of a Sun-synchronous Satellite

2.4 MSU INSTRUMENT DESCRIPTION AND OPERATION

The Microwave Sounding Unit is a 4-channel Dicke radiometer making passive measurements in the 50 - 60 GHz oxygen band. The instrument was built by the Jet Propulsion Laboratory (JPL) of the California Institute of Technology, and is an adaption of the Scanning Microwave Spectrometer which flew on Nimbus 6. The MSU is one of three instruments which makeup the TIROS Operational Vertical Sounder (TOVS) system. Its primary design purpose is to provide a means of temperature sounding in the presence of clouds. A photograph of the MSU is shown in Figure 2.7 and its system parameters are summarized in Table 2.1.

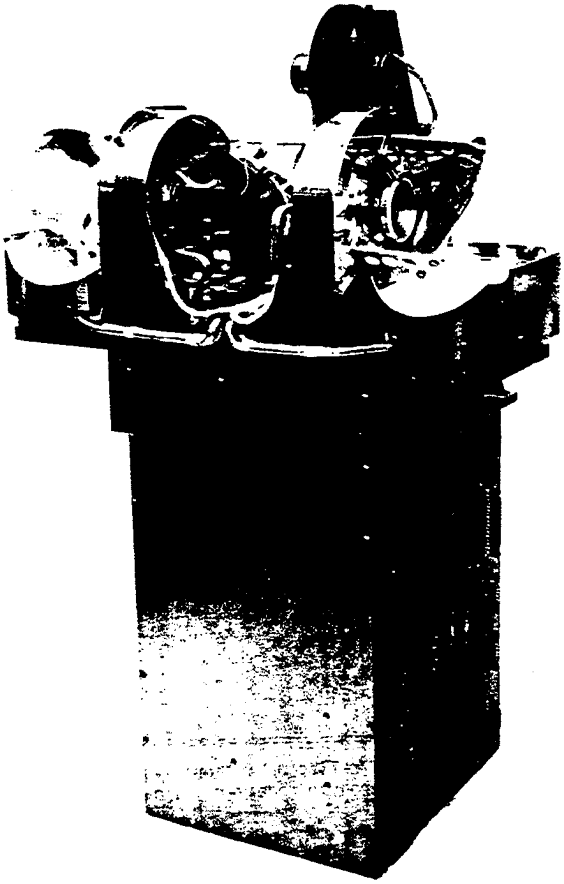

Figure 2.7: The Microwave Sounding Unit (from Schwalb, 1978)

2.4.1 The Antenna and Scan Systems

The Microwave Sounding Unit has two scanning antenna systems. Each antenna system consists of two cross-track rotating reflectors which direct

TABLE 2.1

Table 2.1 : Microwave Sounding Unit Instrument Parameters

Parameter	Value
Instrument Type:	Dicke Radiometer
Channel Frequencies:	
Channel 1	50.30 GHz
Channel 2	53.74 GHz
Channel 3	54.96 GHz
Channel 4	57.05 GHz
RF Bandwidth:	220 MHz
Noise Equivalent ΔT_B:	0.3 °K
Angular Resolution:	7.5° (3 dB)
Ground Field of View:	109.3 km at Nadir
Scan Line:	
Cross-Track Scan Angle	±47.35°
Cross-Track Distance	±1015 km
Time Per Scan	25.6 sec
Number of steps	11
Scan Step:	
Angle	9.47°
Time	1.84 sec
Gap Between Consecutive Passes at Equator:	433 km
Calibration:	Hot reference body and space background each scan cycle
Data Rate:	320 bits s-1
Instrument Mass:	20.9 kg
Instrument Size:	58.4 x 20.3 x 38.1 cm
Average Power Consumption:	30 W

incoming radiation into fixed corrugated horns. The antenna beamwidths are both 7.5° (half power point) from four-inch reflectors, resulting in a ground resolution at the subpoint of 109 km. The reflectors are rotated by highly accurate pulley drives through ten 9.45° steps resulting in 11 Earth views per scan line as shown in Figure 2.8. Figures 2.9 and 2.10 show two examples of the MSU scan pattern. The total scan line covers ±47.35° from nadir. Ground resolution varies from 109 km at subpoint to 323 km at the fringe field of views. Two additional steps provide calibration views of cold space and a blackbody attached to the instrument housing. A new scan line is started every 25.6 seconds to allow synchronization with the other two TOVS instruments every five scan lines.

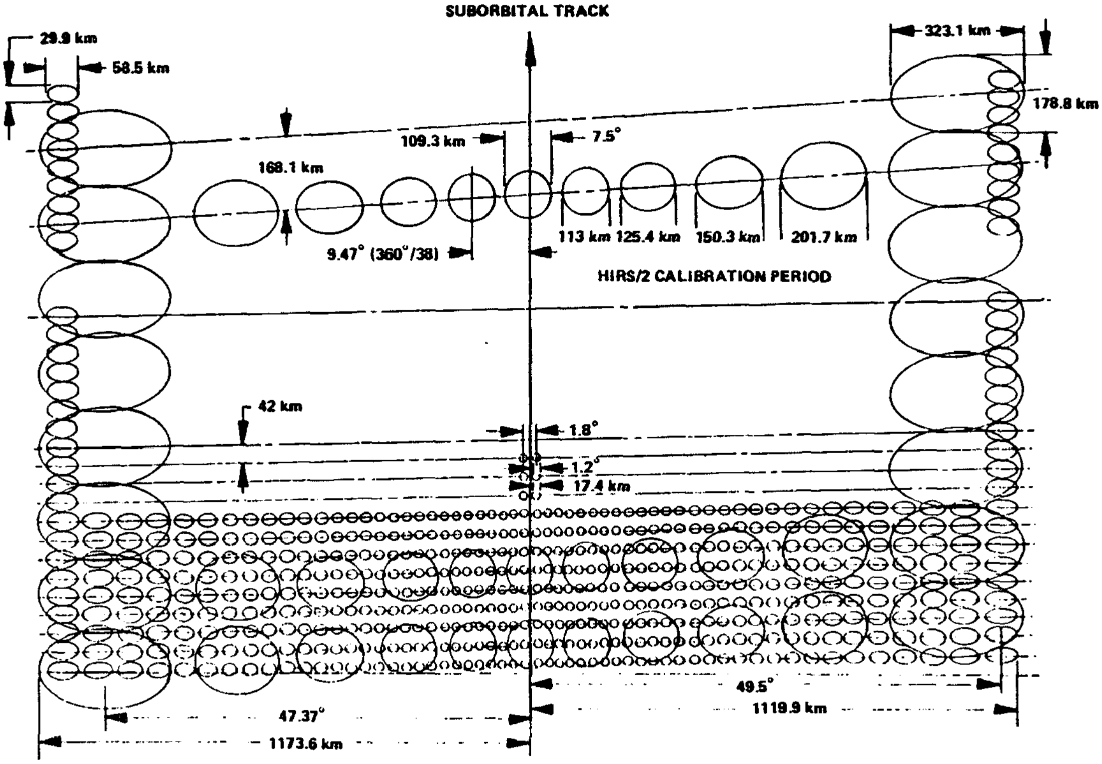

Figure 2.8: MSU Scan Line pattern (large oblate circles) projected on Earth, coverage pattern is shown in relation to the High Resolution Infrared Radiation Sounder (HIRS/2) instrument (smaller circles). (Schwalb, 1978)

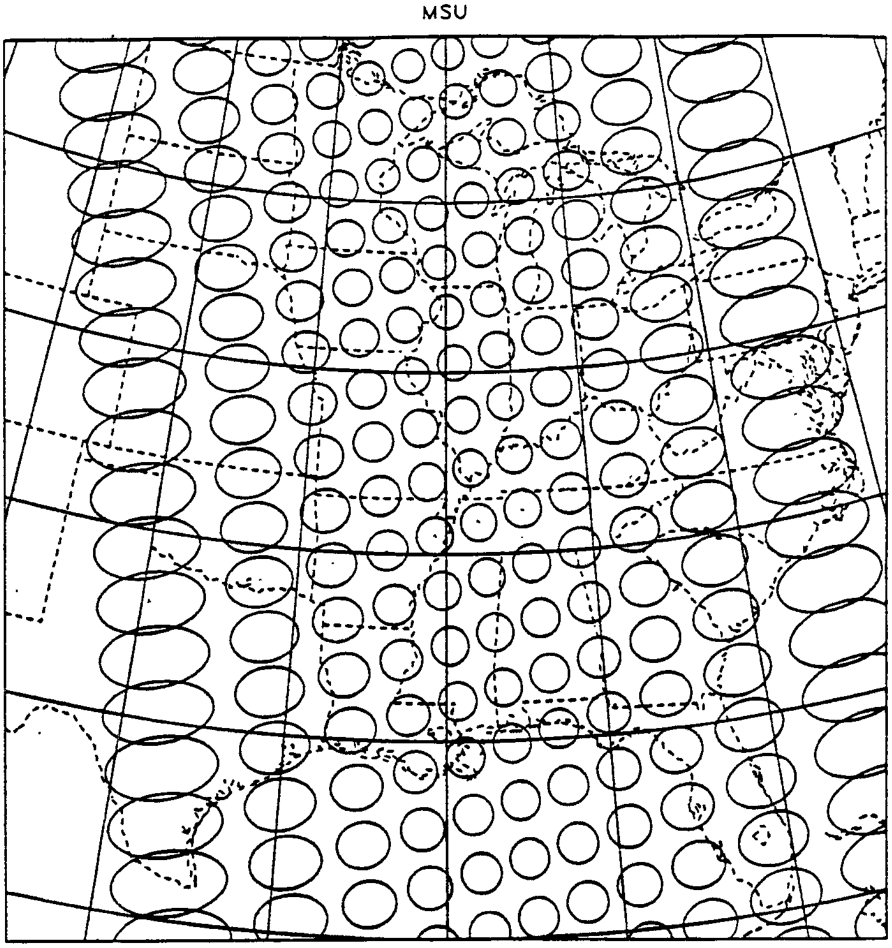

Figure 2.9: Successive MSU Scan Lines.

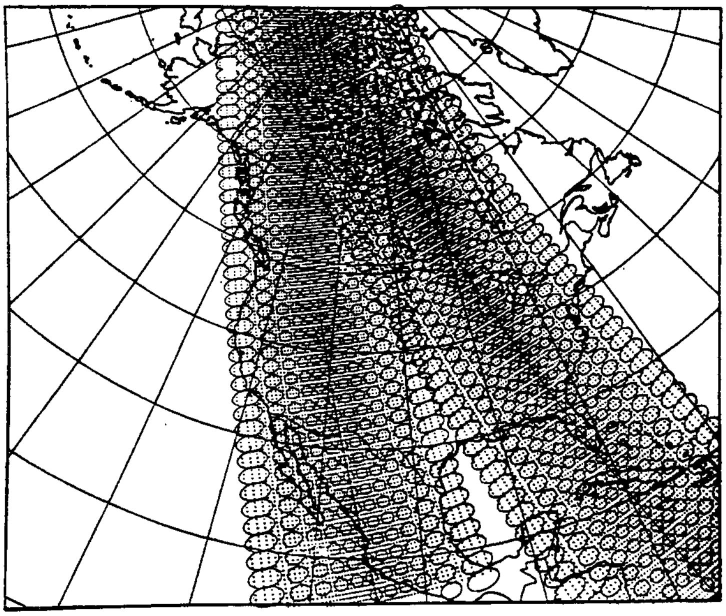

Figure 2.10: MSU Scan PatternTwo Consecutive Orbits. (Smith et. al., 1979) shown along with HIRS scan pattern (small dots).

2.4.2 Radiometer System and Calibration

The Microwave Sounding Unit contains an orthomode transducer, four Dicke superheterodyne receivers, a data programmer, and power supplies. Microwave radiation entering the feedhorn is seperated into vertical and horizontal polarization components. The four resulting beams travel via a waveguide to a Dicke switch which alternates between viewing radiation from the feedhorn and radiation from an internal ambient temperature reference load. This switching occurs at a rate of 1 kHz which modulates the incoming noise temperature. A two-point calibration is performed by viewing cold space and the reference body every scan line. The incoming signal is then mixed with radiation, of the same frequency, produced by a local oscillator to produce an intermediate-frequency (IF). The lower IF is amplified and detected by a superheterodyne receiver. After demodulation the signal is integrated and outputed to the data collection system. The output voltage of the receiver is proportional to the difference in brightness temperature between the scene and internal source. A schematic of this system is presented as Figure 2.11. The radiometer is sensitive to input originating from temperatures ranging from 0 to 350^{o} K. Output from the Microwave Sounding Unit is transmitted to Command and Data Acquisition stations in the TIROS information processor (TIP) format. Radiometric output data and telemetry are formatted into 16-bit words. One scan line of MSU data comprises 112 data words in the format shown in Table 2.2. The Satellite Data Services Division of the National Climatic Data Center archives and offers MSU data on 6250 BPI tapes. Radiometric calibration of the MSU is accomplished by viewing the two calibration targets and determining the relationship between the output of the radiometer and the intensity

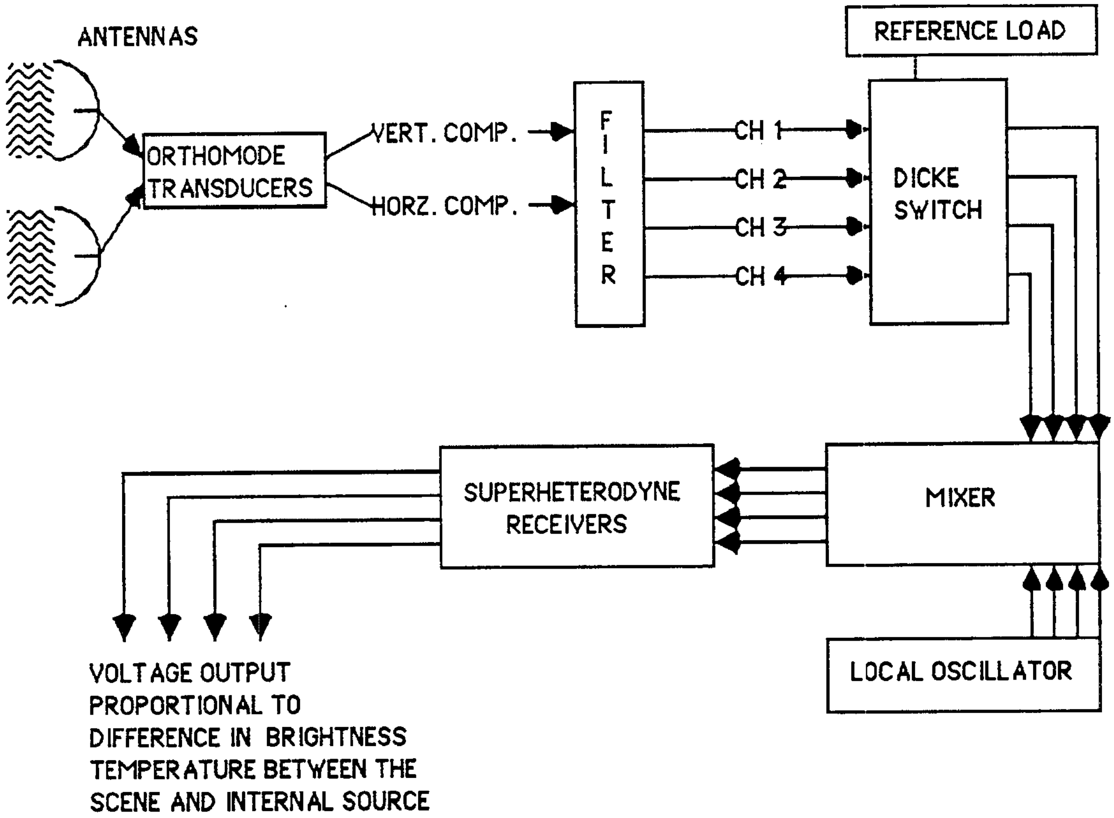

Figure 2.11: The MSU Radiometer Subsystem (Adapted from Njoku, 1982).

of the incident radiation. The temperature of the MSU's calibration targets are measured by two platinum resistance thermistors. The calibration algorithim with coefficients is published in NOAA Technical Memorandum NESS 107 - Rev. 1 (Planet, 1988).

The relationship between input radiance and instrument output counts (0 - 1024) is non-linear. A correction algorithm which allows the converting of raw data (in counts) to radiance in a linear fashion is applied to each channel. This is accomplished using calibration coefficients and normalization coefficients as detailed in the TOVS Level 1b Data section of the NOAA Polar Orbiter Data User's Guide (Kidwell, 1986). Equation 2.11 shows the relationship between count value and radiance

$$E_i = A_{i,1}\, C_i + A_{i,0} \tag{2.11}$$

where E = radiance value in mW/m^2 x steradian x cm^{-1}
C = normalized count value
A = calibration coefficients
(The first subscript represents the ith channel and the second denotes the order of the term).

Converting radiance into an equivalent brightness temperature is a simple one-step process using the inverse of Planck's equation below,

$$T(E_i) = \frac{c_2 v}{\ln\left(1 + \frac{c_1 v^3}{E_i}\right)} \tag{2.12}$$

where E_i = radiance computed from equation 2.11 (mW/m^2*ster*cm^{-1})
$T_B(E_i)$ = Brightness temperature as a function of E_i (^oK)
v = central wave number of the MSU channel filters:

MSU Channel 1 v = 1.6779 cm^{-1}
MSU Channel 2 v = 1.7927 cm^{-1}
MSU Channel 3 v = 1.8334 cm^{-1}
MSU Channel 4 v = 1.9331 cm^{-1}

c_1 = 1.1910659 x 10^{-5} mW/m^2*ster*cm^{-4}

c_2 = 1.438833 cm*^{o}K.

Note: The subscript i refers the the ith- channel.

The Microwave Sounding Unit data used in this study was extracted from 6250 bpi tapes. Thermal data counts, and calibration coefficients were stored in the TOVS data format shown in Table 2.2. These thermal counts were first calibrated and converted to a radiance value, and then to equivalent brightness temperature using the method described above. Section 2.5 discusses the techniques used to process MSU data from tape format to produce MSU brightness temperature fields. It also contains a collection of global and hemispheric MSU brightness temperature map projections.

TABLE 2.2

Table 2.2: MSU Scan Line Format on Data Tapes

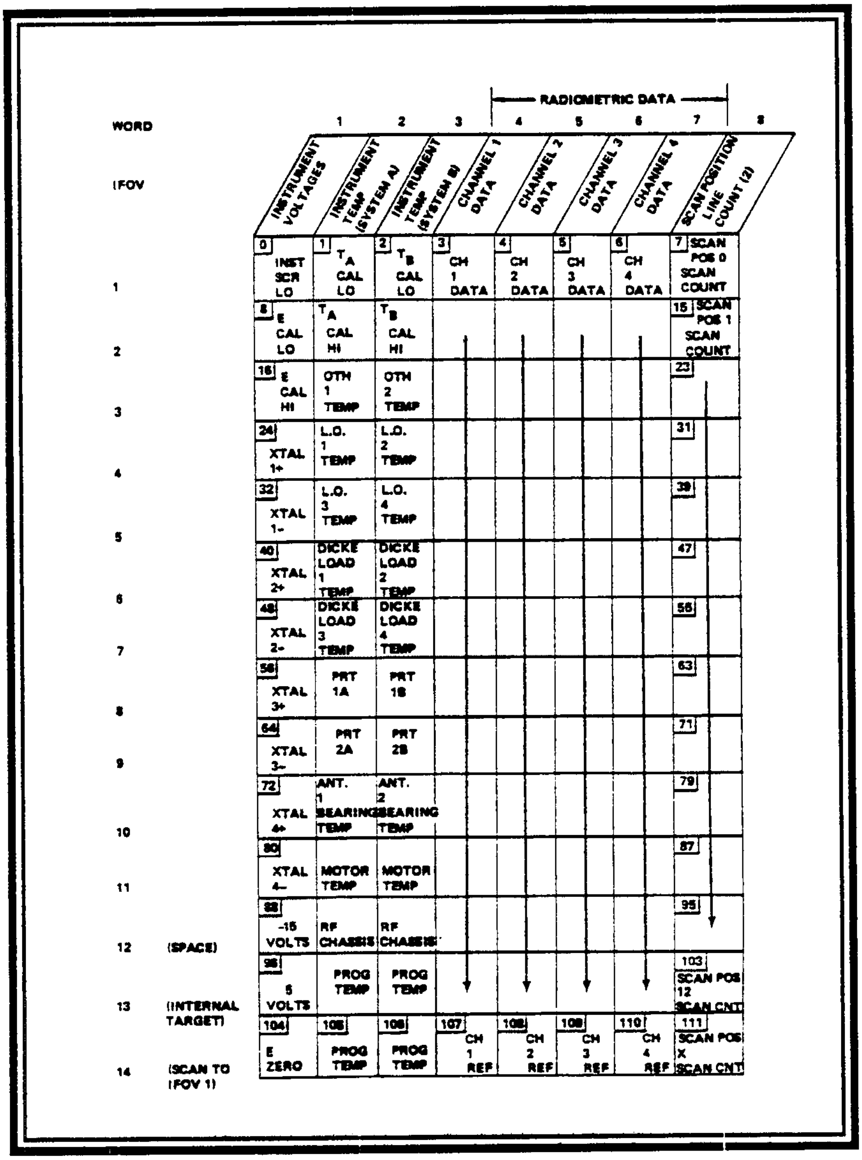

WORD		1	2	3	4	5	6	7	8
					RADIOMETRIC DATA				
IFOV		INSTRUMENT VOLTAGES	INSTRUMENT TEMP (SYSTEM A)	INSTRUMENT TEMP (SYSTEM B)	CHANNEL 1 DATA	CHANNEL 2 DATA	CHANNEL 3 DATA	CHANNEL 4 DATA	SCAN POSITION LINE COUNT (2)
1		0 INST SCR LO	1 T_A CAL LO	2 T_B CAL LO	3 CH 1 DATA	4 CH 2 DATA	5 CH 3 DATA	6 CH 4 DATA	7 SCAN POS 0 SCAN COUNT
2		8 E CAL LO	T_A CAL HI	T_B CAL HI					15 SCAN POS 1 SCAN COUNT
3		16 E CAL HI	OTH 1 TEMP	OTH 2 TEMP					23
4		24 XTAL 1+	L.O. 1 TEMP	L.O. 2 TEMP					31
5		32 XTAL 1-	L.O. 3 TEMP	L.O. 4 TEMP					39
6		40 XTAL 2+	DICKE LOAD 1 TEMP	DICKE LOAD 2 TEMP					47
7		48 XTAL 2-	DICKE LOAD 3 TEMP	DICKE LOAD 4 TEMP					55
8		56 XTAL 3+	PRT 1A	PRT 1B					63
9		64 XTAL 3-	PRT 2A	PRT 2B					71
10		72 XTAL 4+	ANT. 1 BEARING TEMP	ANT. 2 BEARING TEMP					79
11		80 XTAL 4-	MOTOR TEMP	MOTOR TEMP					87
12	(SPACE)	88 -15 VOLTS	RF CHASSIS	RF CHASSIS					95
13	(INTERNAL TARGET)	96 5 VOLTS	PROG TEMP	PROG TEMP					103 SCAN POS 12 SCAN CNT
14	(SCAN TO IFOV 1)	104 E ZERO	105 PROG TEMP	106 PROG TEMP	107 CH 1 REF	108 CH 2 REF	109 CH 3 REF	110 CH 4 REF	111 SCAN POS X SCAN CNT

2.5 MSU BRIGHTNESS TEMPERATURE FIELDS

The Microwave Sounding Unit data used in this study was obtained by researchers at the Cooperative Institute for Research in the Atmosphere at Colorado State University from NOAA-NESDIS. The data set is stored in TOVS format on 6250 bpi magnetic tapes. It covers the time period from January 8, 1987 to February 18, 1987. This section explains the methods used to process MSU data from tape format to produce global and hemispheric projections of equivalent brightness temperature. Section 2.5.1 discusses data preparation and the graphics routines used to map the MSU fields. Section 2.5.2 is a collection of global and hemispheric brightness temperature fields for 8 Jan - 18 Feb 87 divided into 8-31 January, and 1-18 February time periods.

2.5.1 Data Preparation

Preparation of MSU data for mapping is accomplished in four steps. Step one involves reading off raw voltage data converting these voltages to brightness temperature. In step two, the brightness temperature data files are limb-corrected. The third step involves application of an averaging scheme to produce a global 2.5-degree latitude/longitude gridded data set. The final step makes use of graphics routines developed by the Scientific Computing Division of the National Center for Atmospheric Research (NCAR). Subroutine CONRAN is used to contour the brightness temperature fields and the graphics utility EZMAP produces the mapped image (Clare *et al.*, 1986).

2.5.1.1 Data Extraction

FORTRAN-77 program MSUTAPE (Appendix A) reads raw MSU data from the magnetic tapes and produces a formatted brightness temperature file.

MSUTAPE extracts MSU radiometric data, satellite telemetry, and calibration data stored in TOVS format (Table 2.2) from the data tapes. MSUTAPE then performs a calibration on each MSU channel and converts raw thermal count values to equivalent brightness temperature. This procedure is outlined in Section 2.4.2 and discussed in detail by Kidwell, 1986. Subroutines SCAN QUALITY and BADSCAN search for and delete scan lines containing data or transmission errors. Finally, MSUTAPE outputs a formatted brightness temperature file. Figure 2.12a is a sample of MSUTAPE's output. The first line, the file header, contains the satellite name (NOAA-10), the data set name (MSUX), along with file start and end times (ie. 8701080944 = Jan. 8 1987 at 0944 GMT). Then each field-of-view (FOV) is represented by one row of information in the data file. The column 1 contains the FOV number in each scan line and column 2 contains the scan line number. There are 11 FOV's per scan line as shown in Figure 2.8. Columns 3 and 4 show each FOV's latitude and longitude to the hundredth of a degree (northern and eastern hemispheres are positive). Columns 4, 5, 6, and 7 contain the brightness temperature, in degrees Kelvin, for MSU channels 1, 2, 3, and 4 for each FOV. MSUTAPE processes one data file at a time. A data file contains approximately 250 scan lines or 2750 FOVs, the entire 6-week data period (8 Jan - 18 Feb 87) is contained in 577 files.

2.5.1.2 Limb Correction

The geometry of the MSU scan system requires a correction of brightness temperature proportional to the FOV scan angle. As the MSU scans off-nadir through a longer atmospheric path length, each channels' weighting function peaks higher in the atmosphere as shown in Figure 2.4.

```
NOAA10 MSUX      8701080944      8701081136
  1    1 68.95   90.66         225.8 223.4 212.1 209.0
  2    1 71.30   95.23         224.2 225.4 210.8 206.2
  3    1 72.88   99.01         222.1 227.4 211.1 205.1
  4    1 74.08 102.42          223.5 228.5 210.8 204.9
  5    1 75.09 105.77          223.6 229.5 211.4 203.9
  6    1 75.98 109.29          225.0 230.0 211.2 204.0
  7    1 76.81 113.27          240.1 230.8 210.9 203.4
  8    1 77.63 118.11          238.3 230.3 210.0 203.4
  9    1 78.42 124.52          231.3 228.5 208.8 203.6
 10    1 79.17 133.84          226.7 226.0 207.6 205.2
 11    1 79.63 149.09          226.6 221.7 207.4 208.2
  1    2 69.73   86.95         225.6 223.1 210.3 206.5
```

Figure 2.12a: MSUTAPE Output

```
NOAA10 MSUX      8701080944      8701081136
  1    1 68.95   90.66         349.2 232.3 215.6 210.8
  2    1 71.30   95.23         359.9 230.7 213.5 207.4
  3    1 72.88   99.01         354.8 230.6 212.9 205.8
  4    1 74.08 102.42          349.4 230.4 211.7 205.2
  5    1 75.09 105.77          345.9 230.8 211.8 204.1
  6    1 75.98 109.29          345.1 231.0 211.4 204.1
  7    1 76.81 113.27          347.5 231.7 211.4 203.5
  8    1 77.63 118.11          352.2 232.0 211.1 203.6
  9    1 78.42 124.52          357.4 231.9 211.0 204.0
 10    1 79.17 133.84          362.5 232.0 211.1 205.6
 11    1 79.63 149.09          349.6 232.0 211.9 208.4
  1    2 69.73   86.95         349.6 232.4 214.5 208.3
```

Figure 2.12b: MSULIMB Output

```
LAT       LON       NUM OBS          Tb

7.5      -17.5       172.           258.1
7.5      -15.0       163.           258.2
7.5      -12.5       168.           258.3
7.5      -10.0       172.           258.2
7.5       -7.5       178.           258.4
7.5       -5.0       170.           258.6
7.5       -2.5       179.           258.7
7.5        0.0       180.           258.9
7.5        2.5       172.           259.1
7.5        5.0       170.           259.0
7.5        7.5       170.           259.2
7.5       10.0       169.           259.1
```

Figure 2.12c: Averaging Output (MSUChannel 2)

This results in anomalously cold brightness temperatures for FOV's with large scan angles. In order to use brightness temperature measurements from all FOV's without the effects of a cold bias, temperatures are normalized to the value they would have if the satellite observed the FOV at nadir (scan angle 0^o). The Earth-located zenith angles for the 11 MSU scan positions are 0^o, $\pm 10.7^o$, $\pm 21.6^o$, $\pm 32.7^o$, $\pm 44.2^o$, and $\pm 56.6^o$. Smith *et al.*, 1974 has developed a method of computing nadir brightness temperature using regression equations. This method is used by FORTRAN-77 program MSULIMB (Appendix B) to limb- correct the brightness temperature files produced by MSUTAPE. Figure 2.12b is a sample of MSULIMB's output, which corresponds to the MSUTAPE example in Figure 2.12b. The limb-corrected brightness temperatures from the scan fringes have increased, correcting the cold bias. MSU Channel 1 contains limb-correction temperature errors on the order of 120^o K due to surface influences. No data from channel 1 is used in this study.

2.5.1.3 Data Averaging Scheme

The MSU data set available for this study (January 8 - February 18 1987) is divided into 577 files of approximately 250 scan lines each. This amounts to over 1.5 million data points per channel over the six-week period. To simplify the mapping process a simple averaging scheme is used produce a global grid-formatted data set. Each brightness temperature data point location is rounded-off to the nearest 2.5 degree latitude/longitude intersection. The final grid point temperature value is obtained by averaging all data points that round-off to the same grid intersection. Figure 2.13 shows a schematic of this process. For example, all the data points that fall inside the 1.25^o - 3.75^o N.

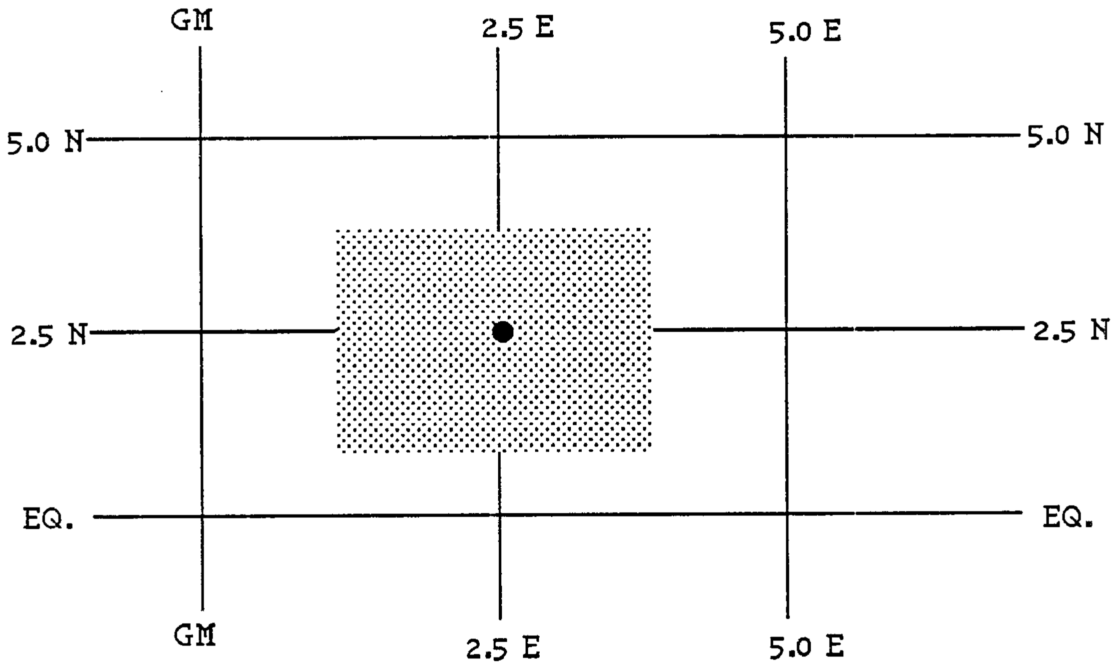

Figure 2.13: Sample Averaging Scheme Grid Area and Point

latitude and 1.25$^{\text{o}}$ - 3.75$^{\text{o}}$ E. longitude box are averaged and recorded as a single data point at 2.5$^{\text{o}}$ N. latitude and 2.5$^{\text{o}}$ E. longitude. This method reduces the global data set from 1.5 million to 10,439 data points per channel. No special weighting was used in the averaging process to account for varying distance from the 2.5$^{\text{o}}$ grid point. Figure 2.12c is a sample of the 2.5$^{\text{o}}$-grid data file resultant from the averaging process. These files are then used by NCAR graphics routines to produce global brightness temperature maps.

2.5.1.4 Graphics Routines used to Produce MSU Fields

The NCAR GKS-Compatible Graphics Package provides all the analysis and mapping routines used to produce the MSU fields presented in Section 2.5.2 (Clare *et al.*, 1986). This package is designed to conform to the international Graphical Kernal System (GKS) standard adopted by the American National Standards Institute (ANSI). This allows computer code to be written in FORTRAN-77 and linked through GKS to produce an executable contouring and mapping program. The Scientific Computing Division at NCAR developed the contouring utility CONRAN and the earth mapping utility EZMAP, both used in this study to produce global brightness maps. CONRAN is also used to contour the MSU temperature anomaly fields presented in Section 4.4.2 Program MSUMAP (Appendix C) was used to call the CONRAN and EZMAP utilities, and along with various graphics options to produce the global MSU brightness temperature fields shown in Section 2.5.2. The next section presents the MSUMAP graphics output, global and hemispheric brightness temperature fields for MSU channels 2, 3, and 4.

2.5.2 Collection of MSU Fields

Microwave Sounding Unit Channel 2, 3, and 4 brightness temperature fields are shown in Figures 2.14 - 2.21 on the following seven pages. Figure 2.14a is a cylindrical equidistant projection of MSU Channel 2's brightness temperature averaged over 8-31 Jan 87, Figure 2.14b is the same data set projected on a northern hemisphere polar stereographic projection. Figures 2.15a and b display MSU Channel 2 brightness temperature averaged over 1-18 Feb 87. Figures 2.16 and 2.17 are arranged in the same sequence as 2.14 and 2.15, but display MSU Channel 3 average brightness temperatures. Likewise, Figures 2.18 and 2.19 shows brightness temperature fields for MSU Channel 4. Figures 2.20 and 2.21 are southern hemisphere polar stereographic projection for 8-31 Jan 87 of Channels 2 and 4, respectively. A detailed discussion of these fields is contained in Chapter 4 where they are

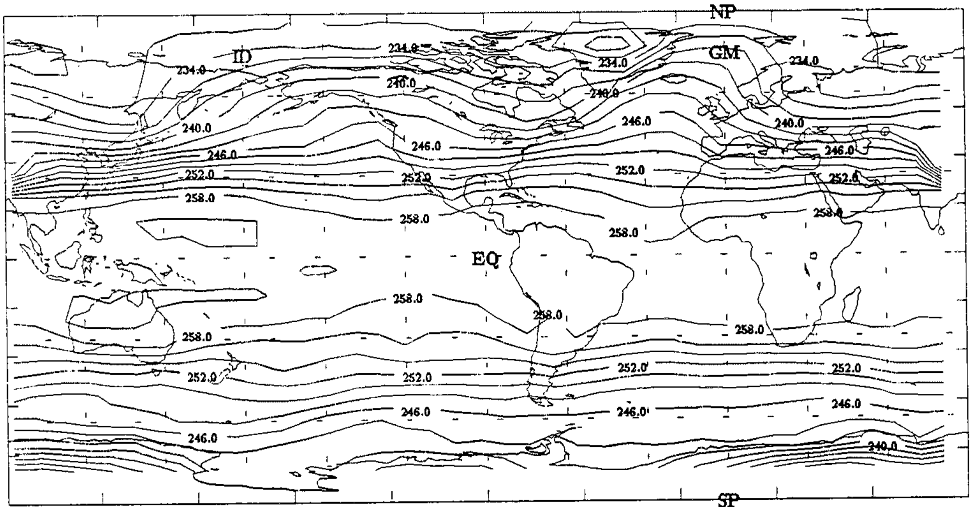

CONTOUR FROM 226.00 TO 262.00 CONTOUR INTERVAL OF 2.0000

Figure 2.14a: MSU Channel 2 Brightness Temperature (K) (8-31 Jan 87)

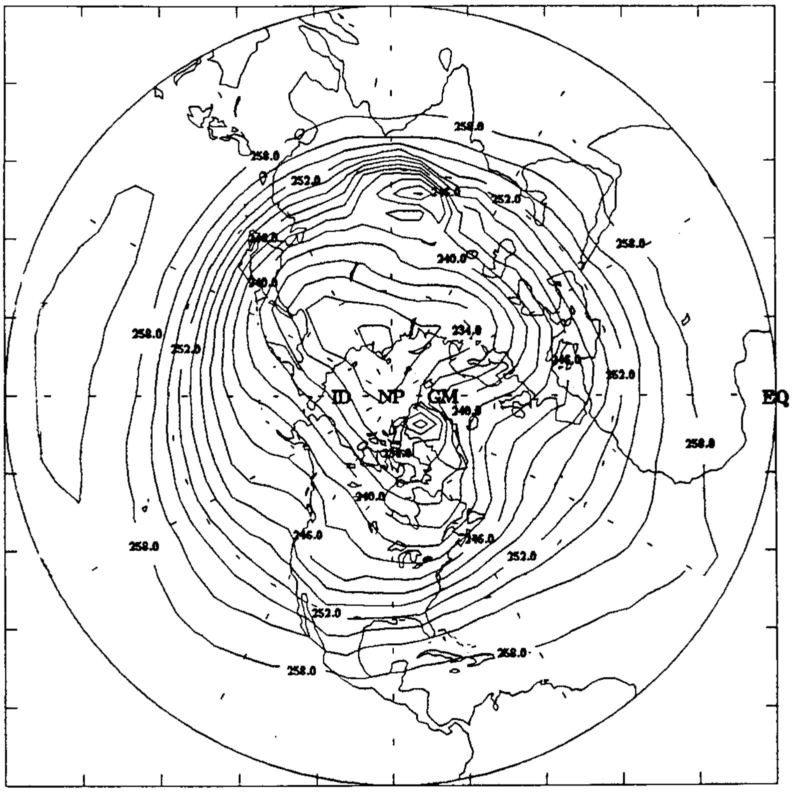

CONTOUR FROM 226.00 TO 262.00 CONTOUR INTERVAL OF 2.0000

Figure 2.14b: MSU Channel 2 Brightness Temperature (K) Northern Hemisphere (8-31 Jan 87)

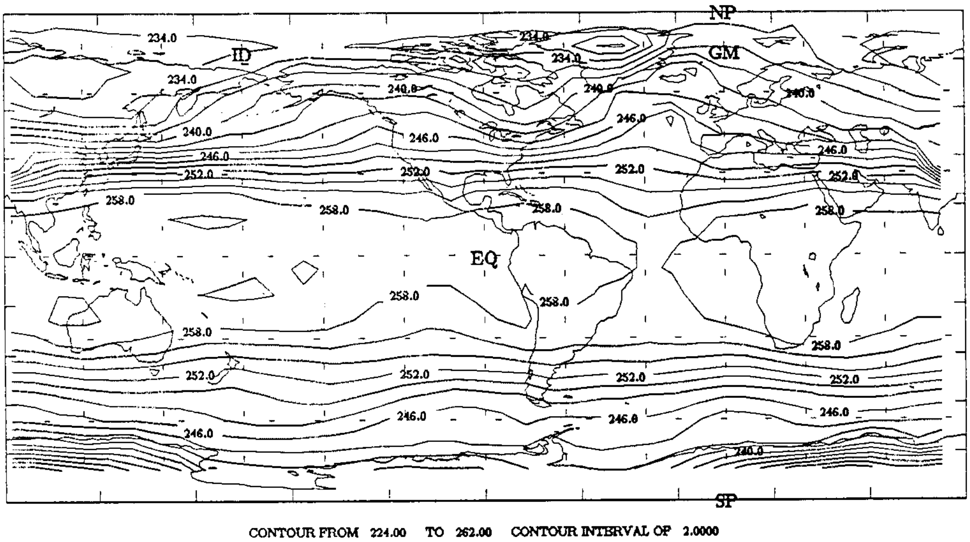

Figure 2.15a: MSU Channel 2 Brightness Temperature (K) (1-18 Feb 87)

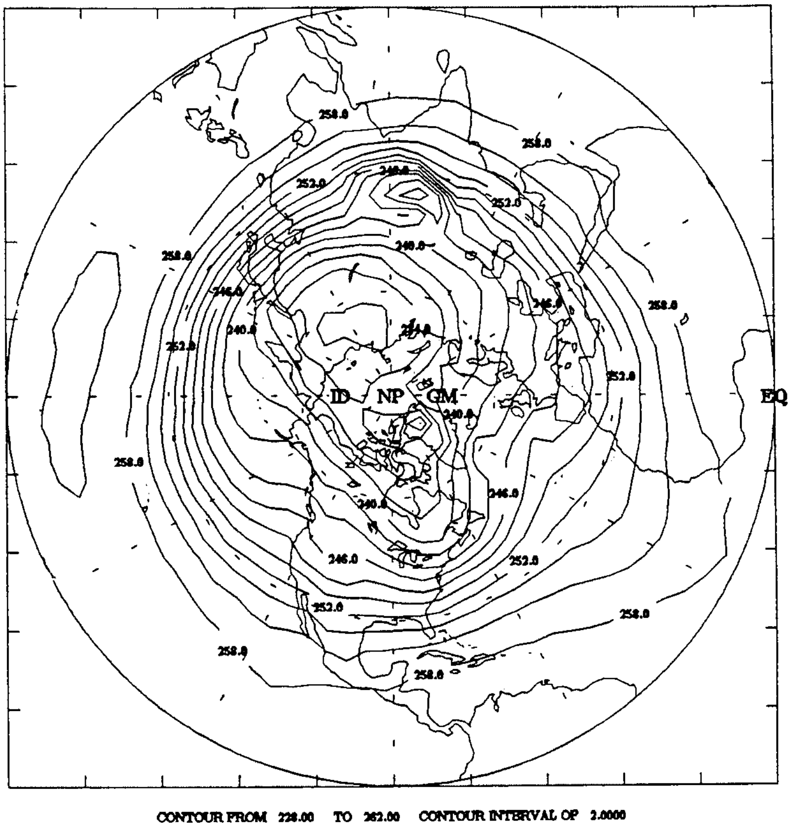

Figure 2.15b: MSU Channel 2 Brightness Temperature (K) Northern Hemisphere (1-18 Feb 87)

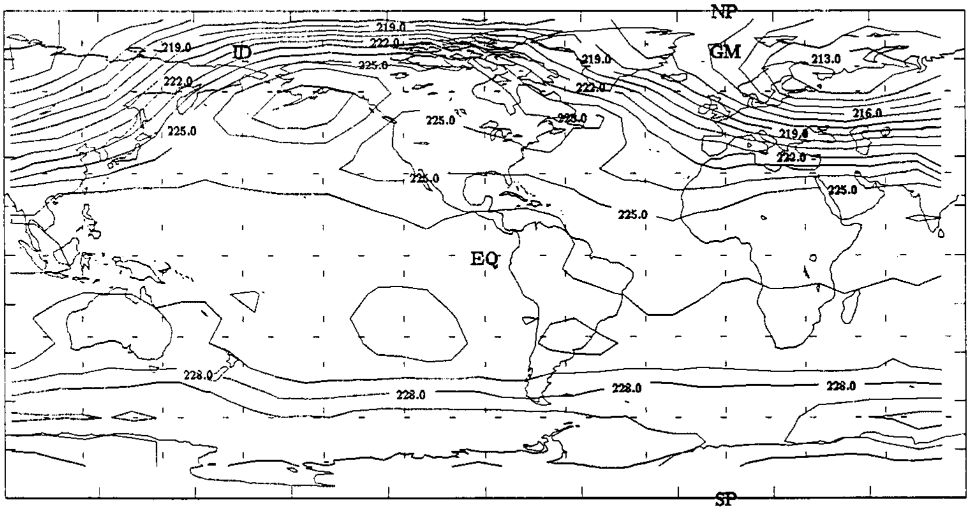

CONTOUR FROM 211.00 TO 231.00 CONTOUR INTERVAL OF 1.0000

Figure 2.16a: MSU Channel 3 Brightness Temperature (K)
(8-31 Jan 87)

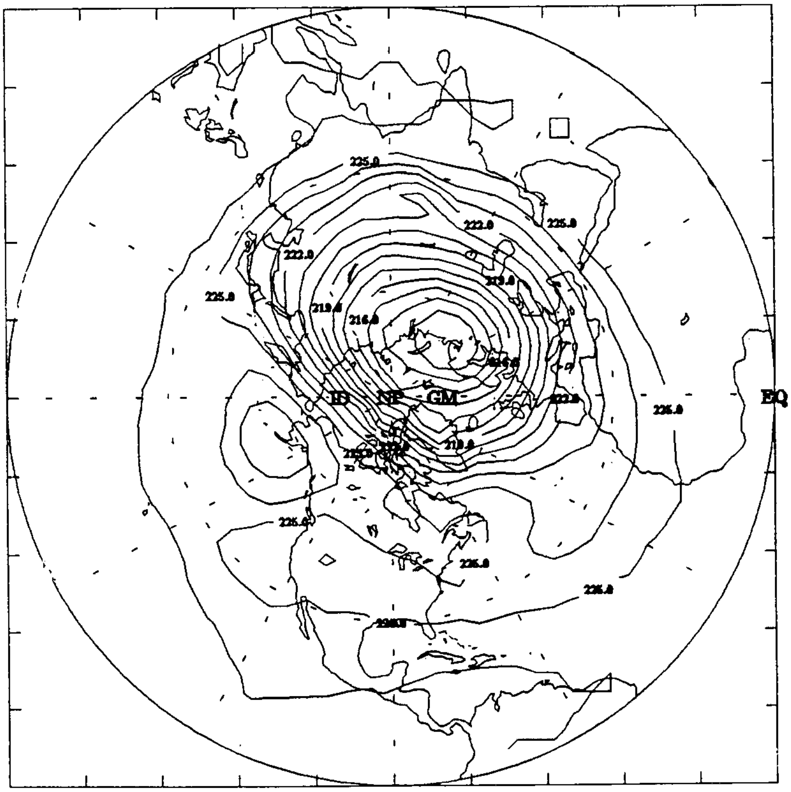

CONTOUR FROM 211.00 TO 228.00 CONTOUR INTERVAL OF 1.0000

Figure 2.16b: MSU Channel 3 Brightness Temperature (K)
Northern Hemisphere (8-31 Jan 87)

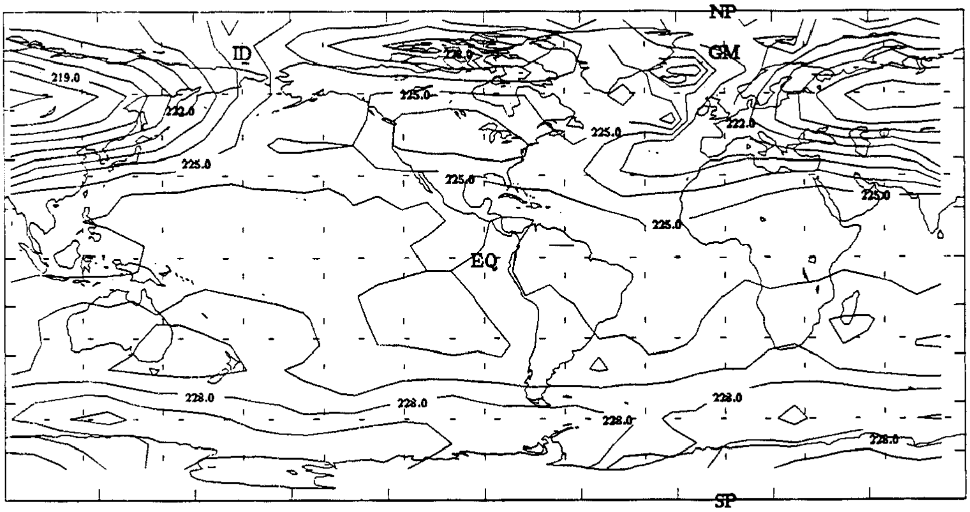

CONTOUR FROM 216.00 TO 236.00 CONTOUR INTERVAL OF 1.0000

Figure 2.17a: MSU Channel 3 Brightness Temperature (K)
(1-18 Feb 87)

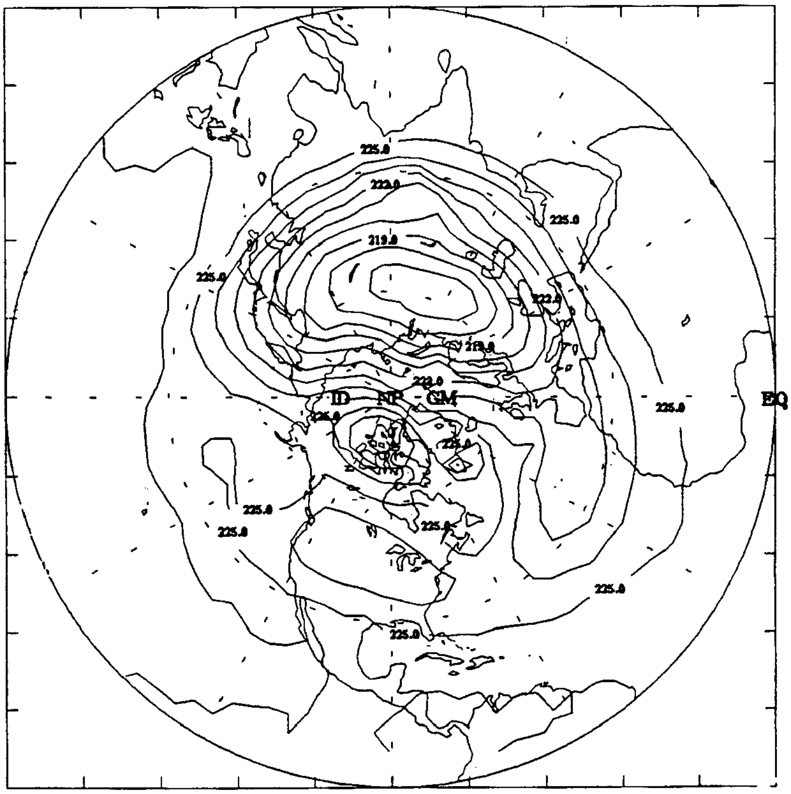

CONTOUR FROM 216.00 TO 236.00 CONTOUR INTERVAL OF 1.0000

Figure 2.17b: MSU Channel 3 Brightness Temperature (K)
Northern Hemisphere (1-18 Feb 87)

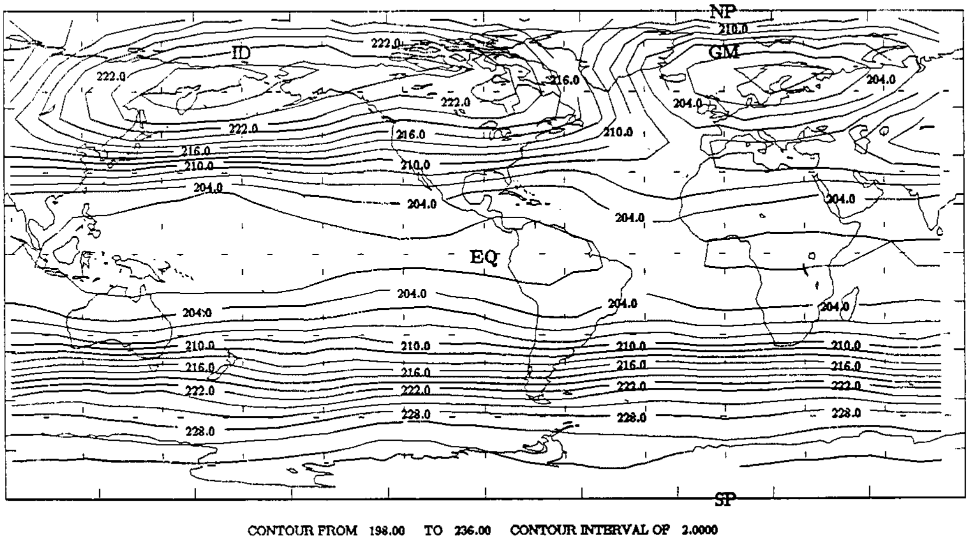

Figure 2.18a: MSU Channel 4 Brightness Temperature (K)
(8-31 Jan 87)

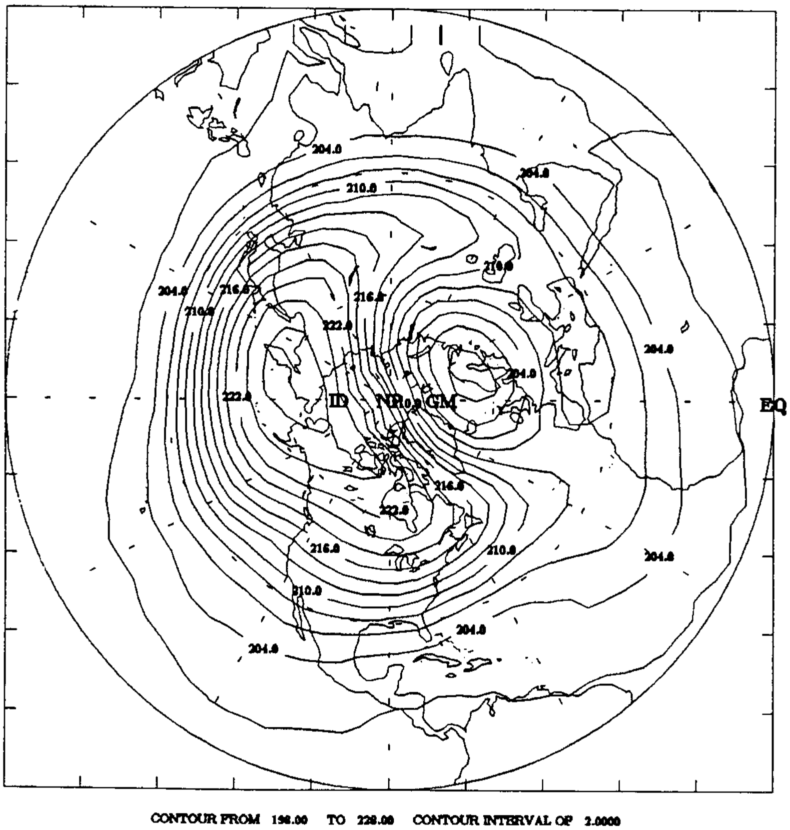

Figure 2.18b: MSU Channel 4 Brightness Temperature (K)
Northern Hemisphere (8-31 Jan 87)

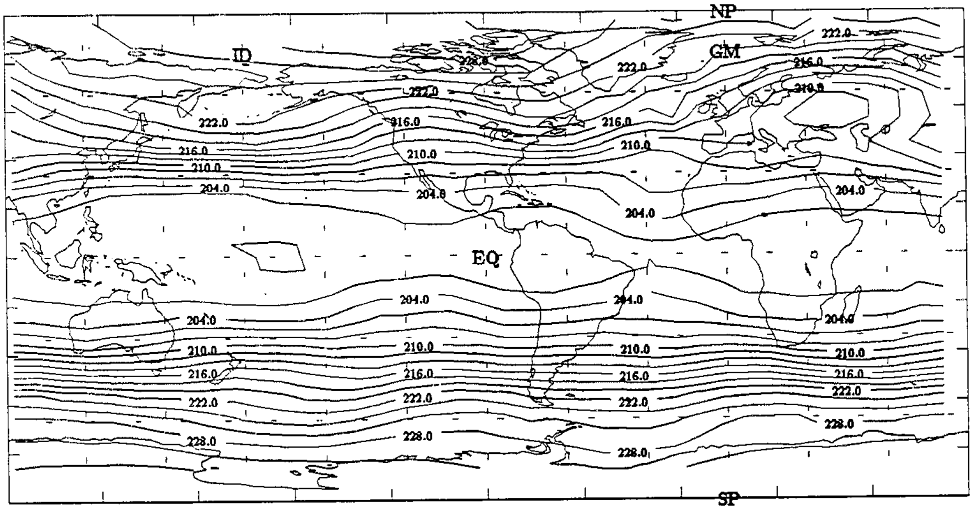

CONTOUR FROM 198.00 TO 236.00 CONTOUR INTERVAL OF 2.0000

Figure 2.19a: MSU Channel 4 Brightness Temperature (K) (1-18 Feb 87)

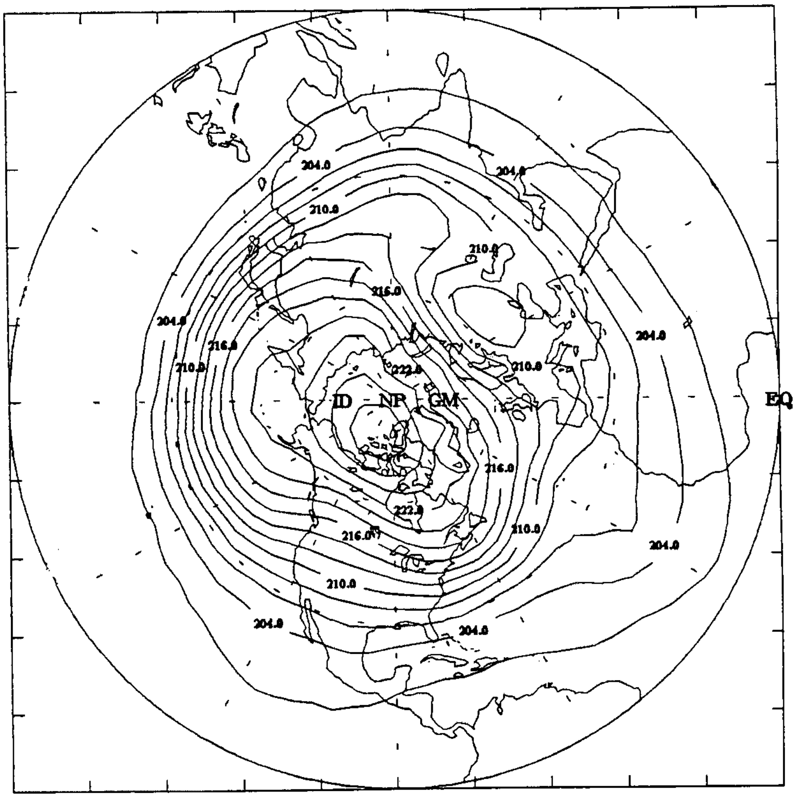

CONTOUR FROM 198.00 TO 236.00 CONTOUR INTERVAL OF 2.0000

Figure 2.19b: MSU Channel 4 Brightness Temperature (K) Northern Hemisphere (1-18 Feb 87)

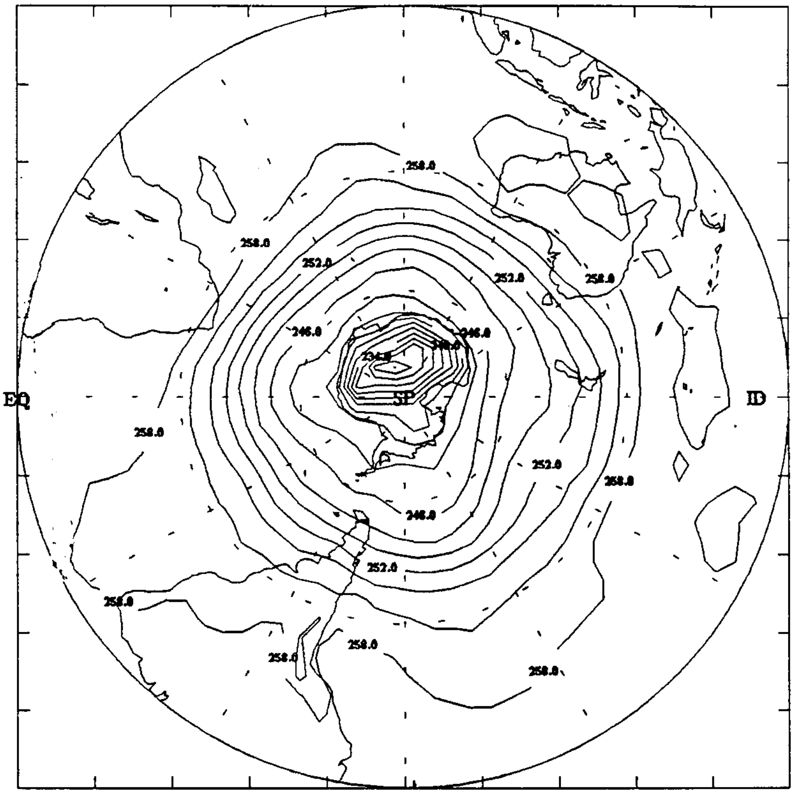

CONTOUR FROM 224.00 TO 262.00 CONTOUR INTERVAL OF 2.0000

Figure 2.20: MSU Channel 2 Brightness Temperature (K), SH, (8-31 Jan 87)

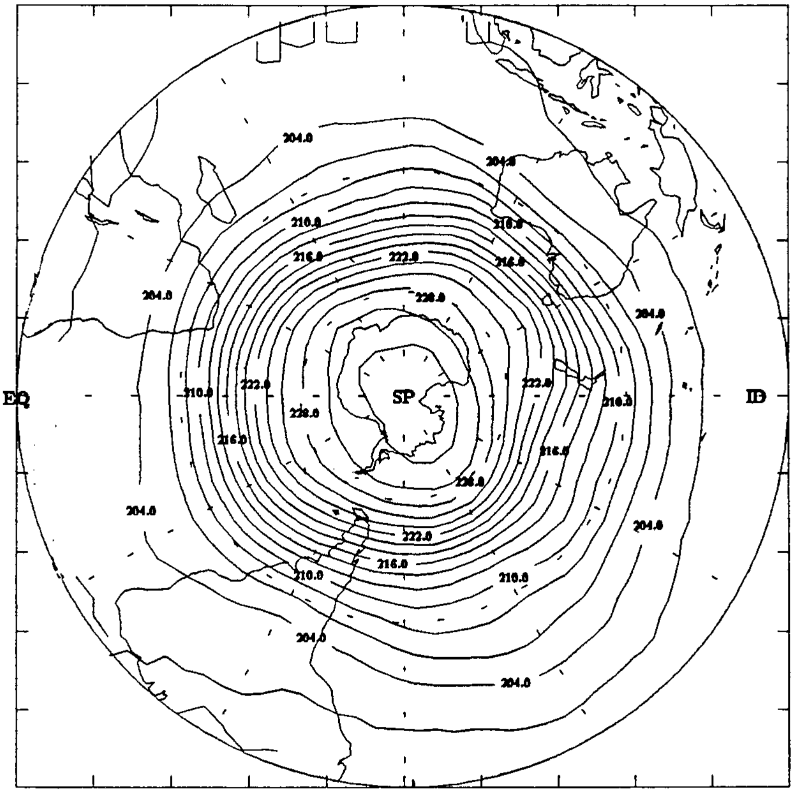

CONTOUR FROM 200.00 TO 236.00 CONTOUR INTERVAL OF 2.0000

Figure 2.21: MSU Channel 4 Brightness Temperature (K), SH, (8-31 Jan 87)

compared and contrasted with corresponding ECMWF analyses presented in Chapter 3. However, several interesting features require comment at this point.

One noticable feature of interest appears in the Channel 2 brightness temperature field due to elevated terrain. Channel 2's weighting function peaks near 700 mb (10,000 ft.) with levels below also contributing to the brightness temperature value, as shown in Figure 2.4. Regions of extensive high elevation such as the Tibetan Plateau, central Greenland, and the Antartic Ice Cap (labelled A, B, and C respectively) protrude into the weighting function of Channel 2. Therefore, since Channel 2 is detecting the surface in these areas they show up as cold anomalies, as shown in Figures 2.14a, 2.14b, and 2.20. The 2.5^{o}-grid resolution appears too small to detect the narrow Rocky Mountain range of North America, however there is a small trough observable in that region. Another interesting feature observable in Channel 2 fields is the contrast of northern and southern hemisphere thermal patterns. The near zonal pattern appearing over the ocean-covered southern hemisphere contrasts well with the trough/ridge pattern over the land-covered northern hemisphere.

The weighting function for Channel 3 peaks near the 300 mb (30,000 ft.) level where horizontal temperature gradients are weaker. The MSU fields of Channel 3 are contoured every 1^{o}K instead of every 2^{o}K as was used for Channels 2 and 4. Figures 2.16 - 2.17 show a cold region centered over the Barents Sea in January migrating southeastward over the north-central Soviet Union during February. Along with this migration, the thermal gradient associated with the cold region is observed to weaken significantly during February.

MSU Channel 4's weighting function peaks in the lower stratosphere near 100 mb. The most distinguishing feature observed from the temperatures obtained from this channel is the positive equator to pole temperature gradient. This is a result of the variation of the tropopause (level where temperature begins to increase with height) with latitude. Figure 2.22 shows the tropopause (thick line) higher and colder over the equator than over the pole during January. Less dense equatorial air forces a higher troposphere at lower latitudes, thus MSU Channel 4 peaks in the cold troposphere over the equator and in the warmer stratosphere over the poles.

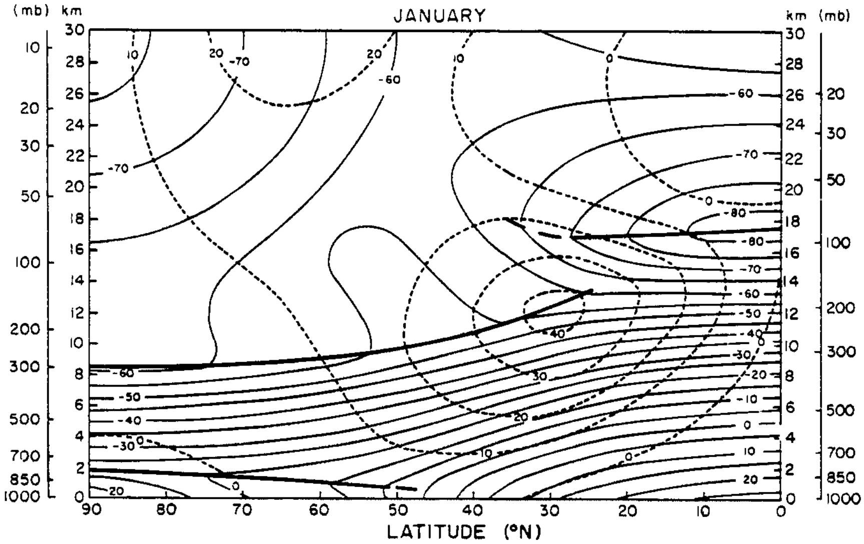

Figure 2.23: Average January Tropopause (Wallace and Hobbs, 1977)
Solid - Isotherms, Dotted - zonal wind, Thick Solid - Tropopause

Channel 4 also show a significant warming in February above 50^{O}N latitude, most noticably in the Barents Sea region.

These global MSU fields will be discussed in more detail in Chapter 4 as they are related to climatology and thermal wind theory. Further analysis of MSU brightness temperature data sets are presented in Section 4.4.1 in an attempt to locate jet stream core regions.

CHAPTER 3

ECMWF ANALYSIS FIELDS

3.1 INTRODUCTION

In order to evaluate the usefulness of the Microwave Sounding Unit fields described in the Chapter 2, a complementary data set was constructed to allow a comparative study. This was accomplished by producing global analyses of data from the European Centre for Medium Range Weather Forcasts (ECMWF) for the time periods corresponding to the MSU fields. ECMWF data is also used to present a brief global climatology for this time period, January and February. Trenberth and Olson, of the Climate and Global Dynamics Division at the National Center for Atmospheric Research (NCAR), have compiled ECMWF global analysis and circulation statistics onto mass storage tapes. The data set begins with January 1978 and currently extends through December 1987. Section 3.2 describes the method used to produce global, zonal, and meridional fields of various meteorological parameters such as temperature, zonal wind, and geopotential height. In Section 3.3, ECMWF climatology is presented along with averaged data sets for time periods coinciding with the MSU fields (8-31 Jan and 1-18 Feb 87). Lastly, Section 3.4 summarizes the climatology and circulation features found in the fields shown in Section 3.3.

3.2 DEVELOPMENT OF ECMWF FIELDS

The ECMWF data archive used in this section to produce global analysis fields is described in detail in NCAR/TN-300+STR (Trenberth and Olson, 1988). The source of the ECMWF data set is the World Meteorological Organization (WMO) Archive. Data is available on a 2.5 - degree global grid at seven pressure levels (1000, 850, 700, 500, 300, 200, and 100 mb), twice daily. This is the same horizontal grid-resolution used to produce the MSU fields in Chapter 2. Trenberth and Olson 1988, completed a comprehensive evaluation of ECMWF data sets, checking for internal and temporal consistency. All data sets containing errors were omitted from analysis. No errors were detected in the 8 Jan - 18 Feb 87 data set. ECMWF data sets are stored on history tapes (mass storage volumes). Each tape contains 15-days of record in 30 files, two data sets per day. The analysis of data on history tapes is performed by the NCAR Community Climate Model (CCM) processor, a post-processing software package developed by Wolski at NCAR. A tutorial supplement to the CCM Modular Processor Users' Guide (Wolski, 1987) was written by Dias of the Climate and Global Dynamics Division at NCAR (Dias, 1987).

Data on the history tapes is inputted to the CCM processor, manipulated, and outputted as metacode graphics in various user-specified forms. A complete list of the processor's functional capabilites is contained in the tutorial. Several of the basic functions of the processor used in this chapter include time averaging, zonal averaging, meridional averaging, and meridional cross-section ploting. Details of the access to the ECMWF data set and use of the CCM processor are provided in Appendix D.

Figures 3.1a-b are two examples of graphics output produced by the CCM processor operating on ECMWF data sets stored on the NCAR Mass Store tape system. Figure 3.1a shows the time-averaged geopotential height field at 300 mb for 8 Jan 87 thru 31 Jan 87. The 48 ECMWF data sets covering 8-31

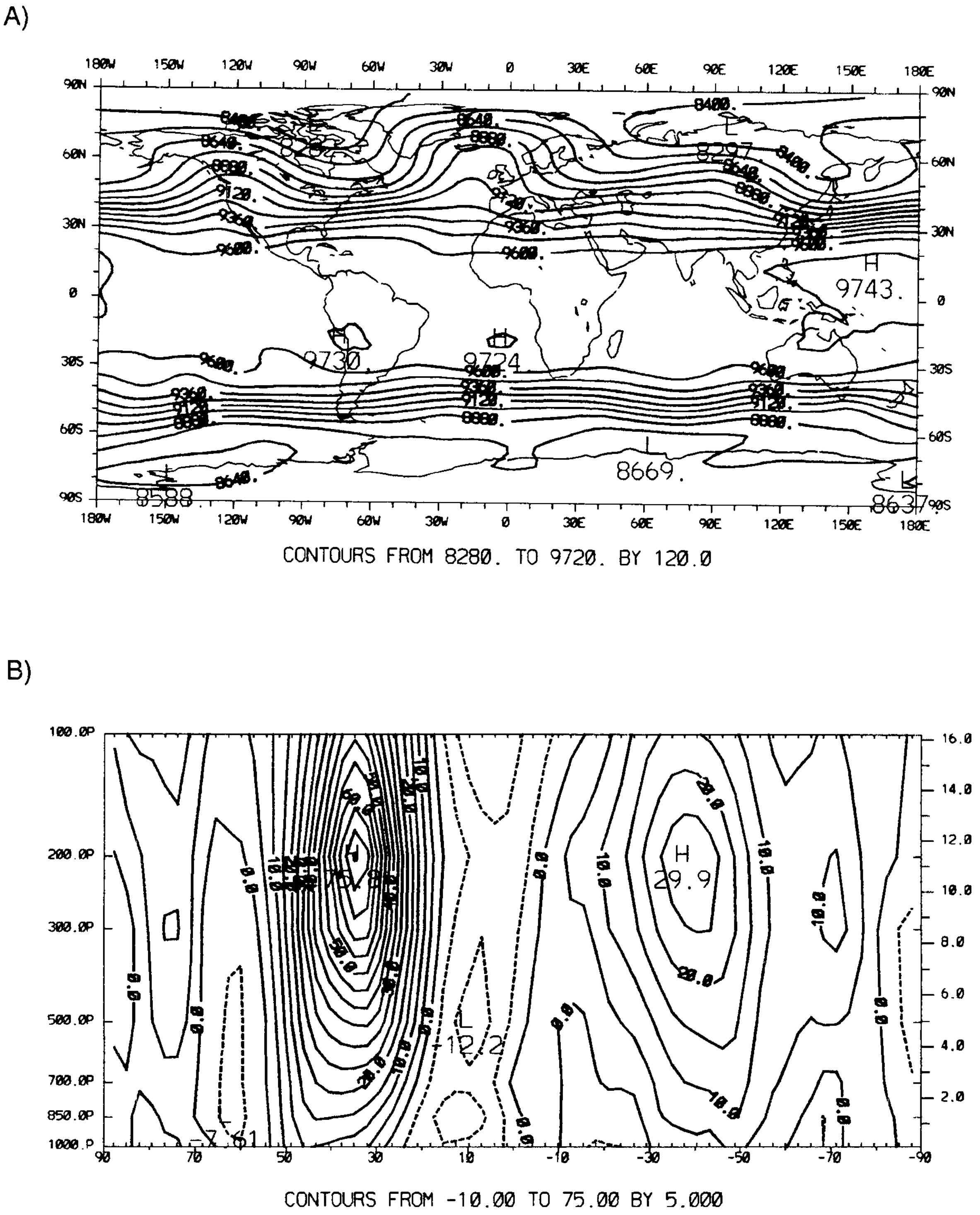

CONTOURS FROM 8280. TO 9720. BY 120.0

CONTOURS FROM -10.00 TO 75.00 BY 5.000

Figure 3.1: ECMWF Fields Produced Using The CCM Processor
A) 300 MB Geopotential Height, 8-31 Jan Average
B) Meridional Cross-Section of Zonal Wind at 165E, 8-31 Jan 87.

Jan were time-averaged to produce this field. The processor then contoured the 300 mb geopotential height field, at a 120 decameter interval, onto a equatorial cylindrical projection. Many of the comparisons discussed in Chapter 4 are presented on polar sterographic projections. Another example of CCM processor capabilities is shown in Figure 3.1b. It shows the time-averaged meridional cross-section of zonal wind (U) at 165^{0} East longitude for the same time period in Figure 3.1a. This is produced by first time-averaging the ECMWF data sets and then performing a zonal average, in this case the zonal average consisted of only one meridonal grid point at 165.9^{0} East (the ECMWF grid does not exactly coincide with latitude/longitude lines). The time-averaged zonal wind is contoured at 5 ms^{-1} intervals. Tight geopotential packing over Japan (and regions east of the major northern hemispheric land masses), south of Australia, and west of South America are evident in Figure 3.1a. This is reflected in Figure 3.1b as zonal wind maximums.

The CCM processor can also manipulate ECMWF data sets to produce fields not specificly stored on history tapes. Figures 3.2a-b are two examples of user-specified derived fields that are used in Chapter 4 to compare with MSU fields; geopotential and streamfunction difference. These fields are produced by taking the difference between two previously time-averaged geopotential height or streamfunction fields. Figure 3.2a shows 850-500 mb geopotential thickness averaged over 8-31 Jan on a northern hemisphere polar stereographic projection. Several similar features are evident in Figure 3.1a, such as ridging over the North Atlantic and a trough off the east coast of Asia. Figure 3.2b shows 1000-300 mb streamfunction difference on a similar projection. Streamfunction difference fields are compared with MSU thermal fields in Chapter 4.

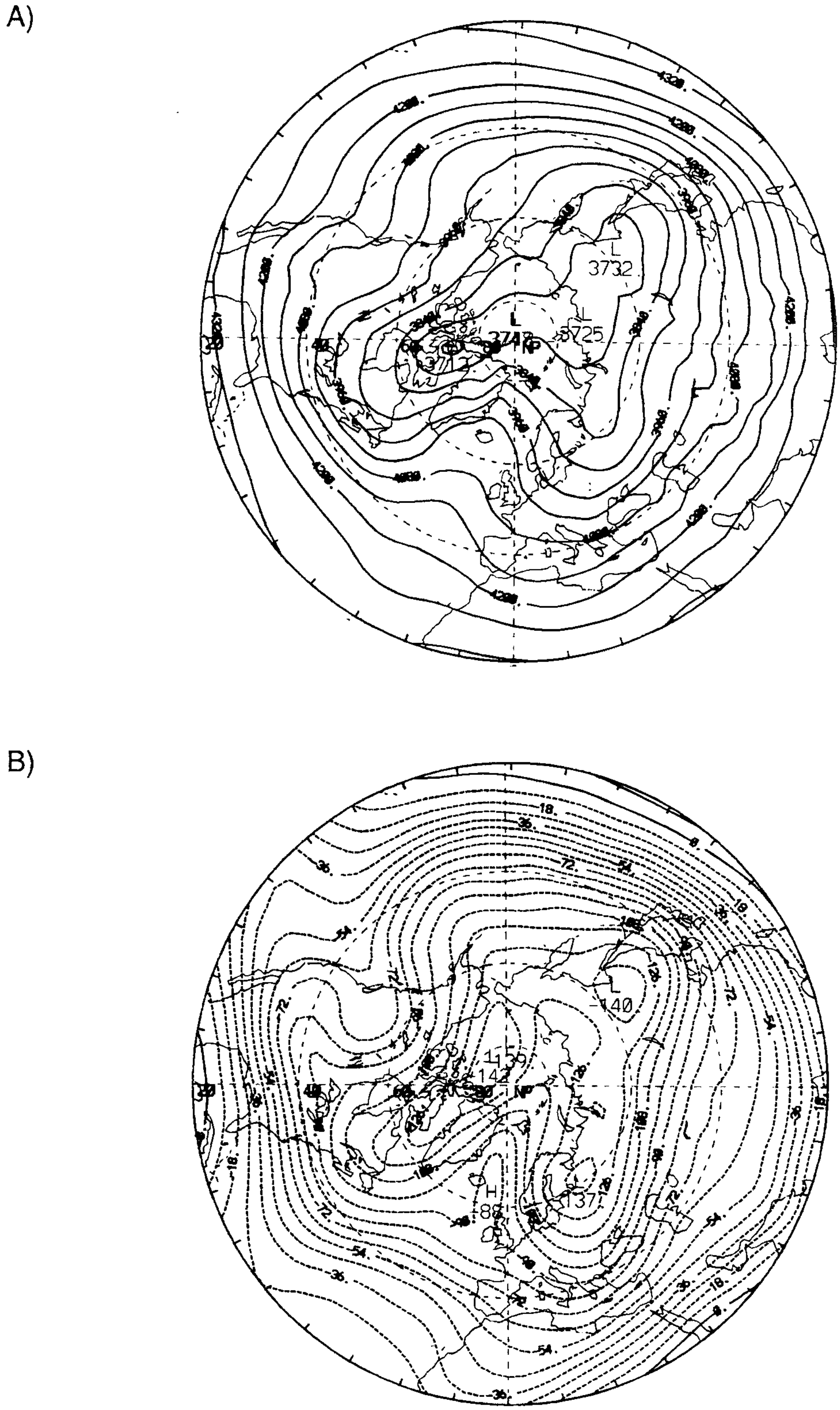

Figure 3.2: ECMWF Derived Fields Produced Using The CCM Processor
A) 850-500 MB Geopotential Thickness, 8-31 Jan
B) 1000-300 mb Streamfunction Difference, 8-10 Jan

The next section in this chapter presents ECMWF fields of temperature, geopotential height, and zonal wind as a climatological overview, and an overview of the time period coinciding with the MSU fields developed in Chapter 2.

3.3 COLLECTION OF ECMWF ANALYSIS FIELDS

The fields presented in this section are arranged in two time-averaged formats. Figures 3.3 - 3.10 show ECMWF fields of temperature, geopotential height, and zonal wind averaged from 1979-1986 along with similar fields averaged over the specific time-periods corresponding to the MSU data set analyzed in Chapter 2. Each figure shows a January or February 79-86 climatology field and a corresponding 8-31 Jan 87 or 1-18 Feb 87 time-averaged field. Figure 3.3a shows the global 100 mb January temperature field averaged from 1979-1986 while Figure 3.3b shows the time-average for 8-31 Jan 87. Figure 3.4a-b shows 100 mb temperature fields for February 79-86 and 1-18 Feb 87. Figures 3.5a-b and 3.6a-b show the 300 mb temperature fields in the same format and Figure 3.7a-b shows 700 mb January temperature fields. Figures 3.8a-b and 3.9a-b show January and February time-average 300 mb geopotential height fields, and Figure 3.10a-b shows January 300 mb time-averaged zonal wind fields. The next section contains a brief discussion of several climatology and general circulation features present in these ECMWF fields. A comparison between ECMWF fields and MSU fields is contained in Chapter 4.

3.4 Discussion of ECMWF January and February Climatology

January and February climatology derived from ECMWF data sets is shown in Figures 3.3 thru 3.10 for the purpose of presenting an overview of circulation features during this time period. This climatology is also used as a reference to compare with 8-31 Jan 87, and 1-18 Feb 87 ECMWF analyses to detect any anomalies present during that period.

The 100 mb temperature fields show several interesting feaures. As expected the southern hemisphere thermal pattern is more zonal than the northern hemisphere as a result of larger ocean regions. Also expected at 100 mb the temperature is observed to increase with latitude, a result of a the variation of tropopause with latitude. Near the equator the 100 mb level is in the cold upper- troposphere while near the poles the 100 mb level is in the warmer lower-stratosphere. In the northern hemisphere a 226 K maximum is observed over the North Pacific extending along the 60°N latitude belt with a relative minimum over the North Atlantic. Both January and February climatology show a 204 K minimum centered just north of Norway. The 8-31 Jan 87 data set average shows a similar 100 mb temperature pattern with January climatology, a 203 K minimum centered over Norway and a 229 K maximum along 60°N. Temperatures are 5-10 K higher over Canada and Alaska though. A much stronger anomaly is seen in the 1-18 Feb 87 data, the cold pool near the North Pole is 15-20 K warmer than what both the February climatology and the 8-31 Jan data sets show. A 232 K maximum is shown along 110°W near the pole. The warming appears to be northward of 50°N, with no corresponding warming observed in the southern hemisphere.

Figures 3.5a-b and 3.6a-b show the 300 mb temperature fields for Jan and Feb 87, respectively. Since the 300 mb level is in the troposphere at all latitudes, temperature is observed to decrease moving from equator to pole. The strongest baroclinicity, temperature gradients on a constant pressure surface, at 300 mb is associated with the intense jet located at about 35°N as

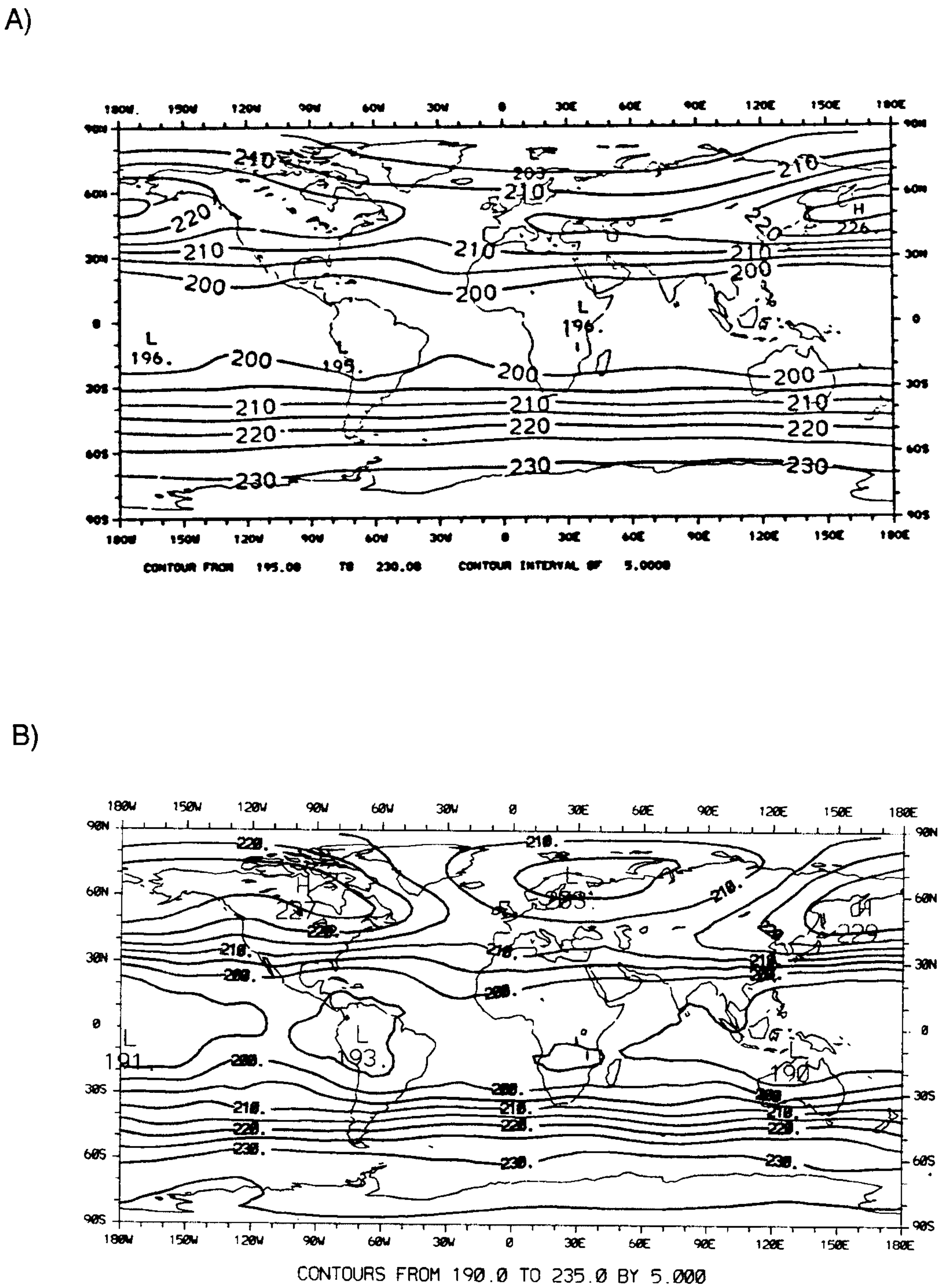

Figure 3.3: ECMWF 100 mb Temperature Field ($^{\circ}$K) for
A) 1979-1986 January Average
B) 8-31 January 1987 Average

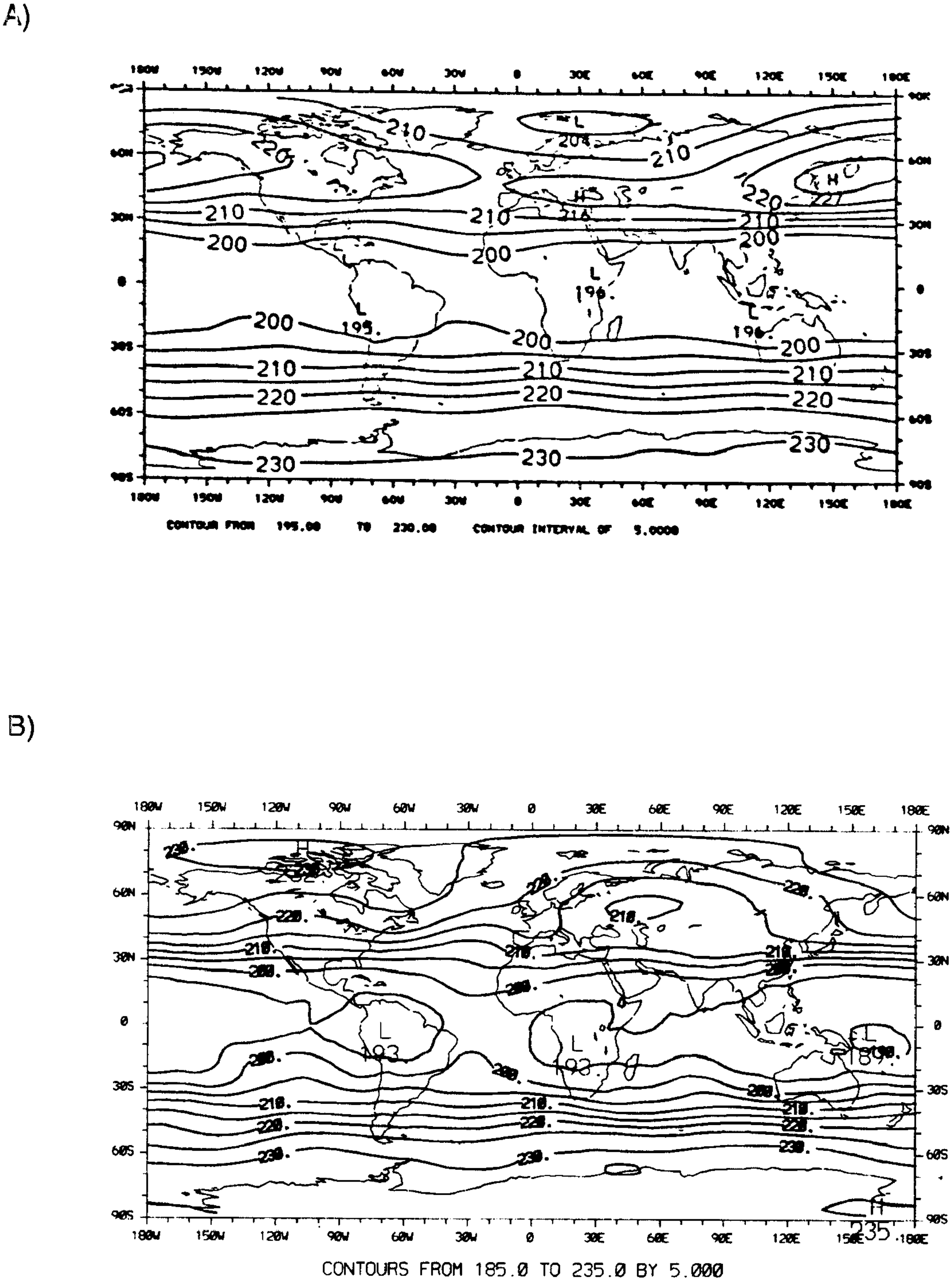

Figure 3.4: ECMWF 100 mb Temperature Field (^{o}K) for
A) 1979-1986 February Average
B) 1-18 February 1987 Average

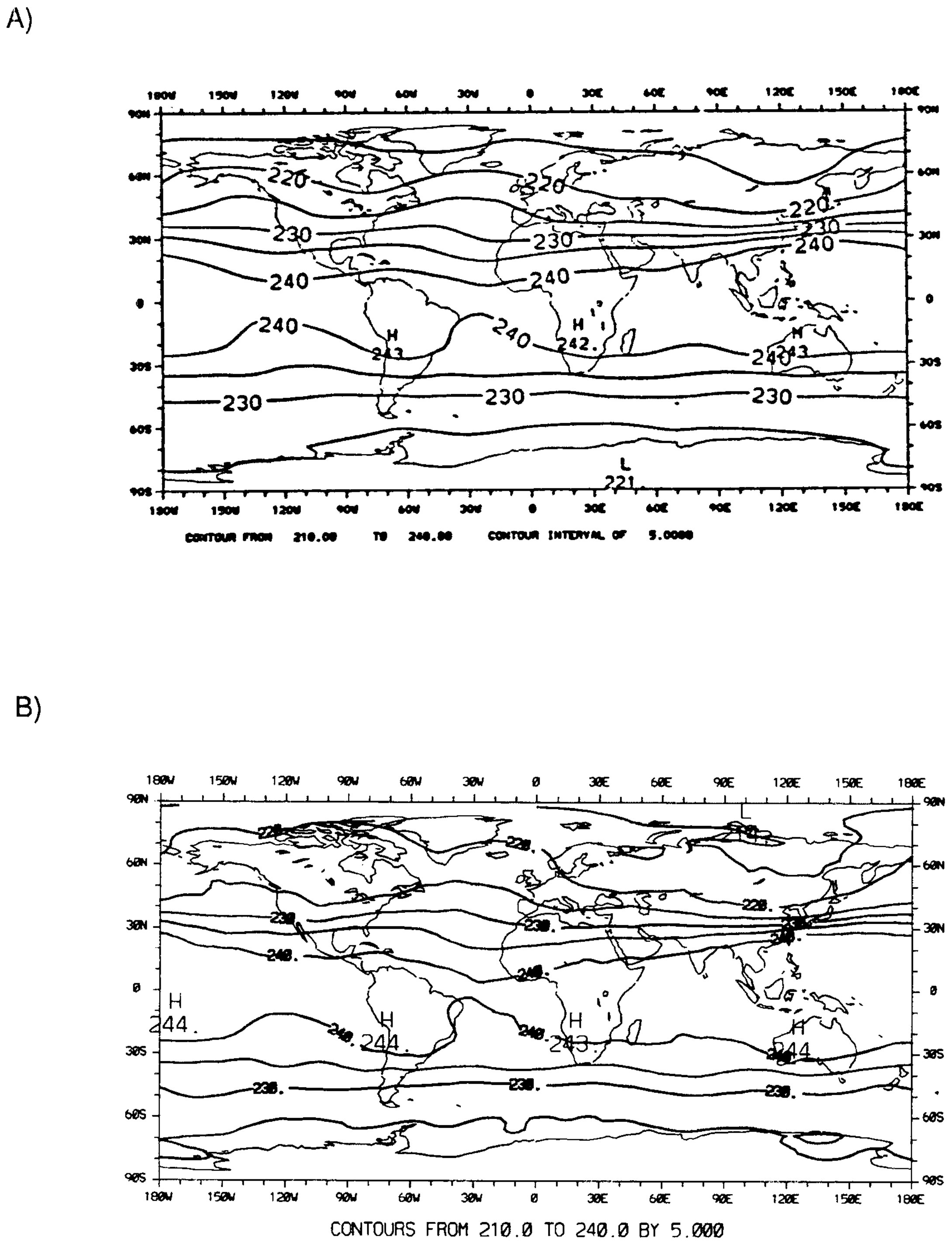

Figure 3.5: ECMWF 300 mb Temperature Field (^{O}K) for
A) 1979-1986 January Average
B) 8-31 January 1987 Average

A)

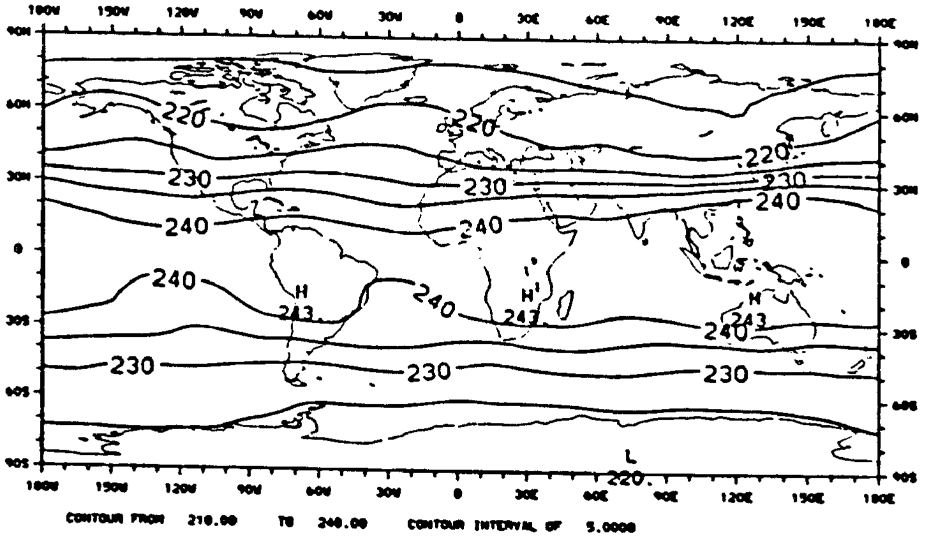

B)

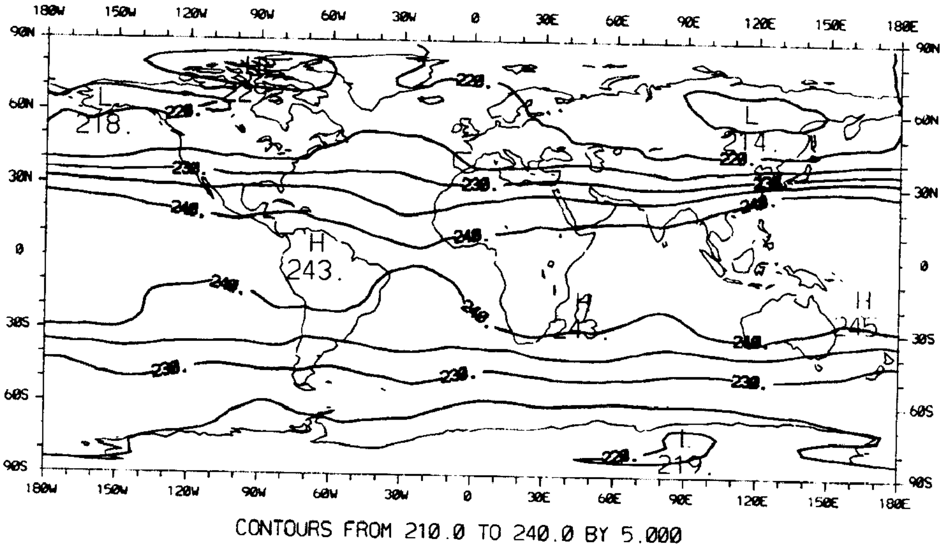

Figure 3.6: ECMWF 300 mb Temperature Field (^{O}K) for
A) 1979-1986 February Average
B) 1-18 February 1987 Average

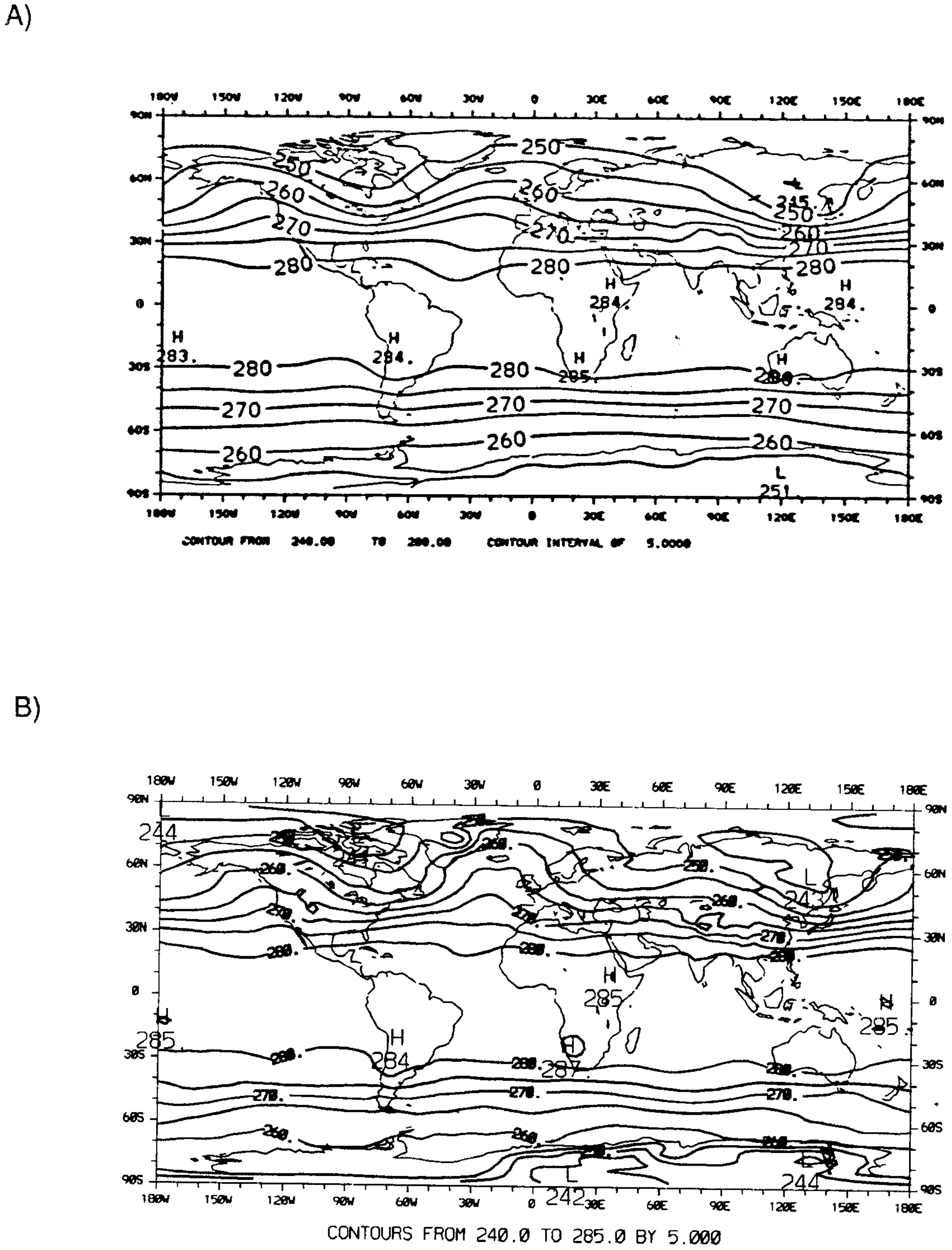

Figure 3.7: ECMWF 700 mb Temperature Field (^{0}K) for
A) 1979-1986 January Average
B) 8-31 January 1987 Average

also seen in Figure 3.1a. The 8-31 Jan temperature pattern is remarkably similar to January climatology, ridging is observed over the North Atlantic due to the warmer ocean temperatures compared to nearby land temperatures. The strongest meridional temperature gradients are associated with the jet stream just south of Korea. In addition to both these features, the 1-18 Feb 300 mb ECMWF data shows a regional warming over northern Canada with respect to climatology. A 229 K maximum is shown over northern Canada in Figure 3.6b. February climatology shows a temperature of 215 K, and 1-31 Jan shows a temperature of 220 K in this region. From these figures it is evident the warming observed at 100 mb is also observed to a smaller degree at 300 mb.

Figures 3.7a-b show 700 mb temperature fields for January and 8-31 Jan. The effects of cold land surface are seen to influence 700 mb temperature in the winter northern hemisphere. Cold minimums are shown on both figures over Canada and Siberia with relative maximums over the warmer ocean regions, especially where the Gulf Stream crosses the North Atlantic. The cold core continential low temperatures over Siberia and N. Canada at 700 mb are shallow phenomen, as we expect, gradually being replaced aloft, as seen in Figure 3.4a and b, by comparatively warmer air. The 8-31 Jan data set shows three regions of relative minimums due to extensive elevated terrain (where the surface is above 700 mb). These are seen over Greenland, the Tibetian Plateau, and Antartica. Comparing Figures 3.7a and b, 8-31 Jan 87 is shown to have a normal January 700 mb thermal pattern.

January and February 300 mb geopotential height fields are shown in Figures 3.8a-b and 3.9a-b. Climatology shows a wave number 2 pattern in the northern hemisphere with troughs located off the east coast of North America and Asia and ridges over the west coasts of North America and Europe. Regions of strongest meridional gradient and hence geostrophic wind are seen off the east coast of the US and over Japan. The 8-31 Jan and 1-18 Feb data sets appear to show a slightly tighter meridional gradient than climatology in these regions. In the southern hemisphere a zonal pattern dominates similar to temperature. The largest geopotential anomaly in the 8-31 Jan 87 field is the strength of the North Atlantic ridge. The 300 mb geopotential height in this region is 300-400 meters higher than January climatology. The 1-18 Feb data sets show this ridge weakening, returning to its climatological value.

The last ECMWF figures used in this study are of 300 mb zonal wind for January climatology and 8-31 Jan 87. As expected Figures 3.10a-b show zonal wind maximums to exist in regions of strong meridional temperature and geopotential height gradients. Climatology shows a 60 ms^{-1} maximum along 30^{o}N off the east coast of Asia and a 40 ms^{-1} maximum off the east coast of the US which are regions already noted for the packing of the temperature gradient. In the southern hemisphere the 30 -40 ms^{-1} zonal wind maximum lies in a zonal band along 45^{o}S. Equatorial easterlies are observed near the equator. The 8-31 Jan data set shows all the major features of climatology. The jet off the east coast of the United States is slightly (7-8 ms^{-1}) stronger than climatology and a small wind maximum is seen north of Iceland that does not appear on climatology. These small anomalies are associated with the geopotential ridge anomaly seen in Figure 3.8b.

The ECMWF data set on mass store at NCAR combined with the capabilites of the CCM processor create a valuable and easy to access meteorological data system for researchers. Its capability to quickly create user-specified and derived fields make this system a valuable tool that can be applied to research

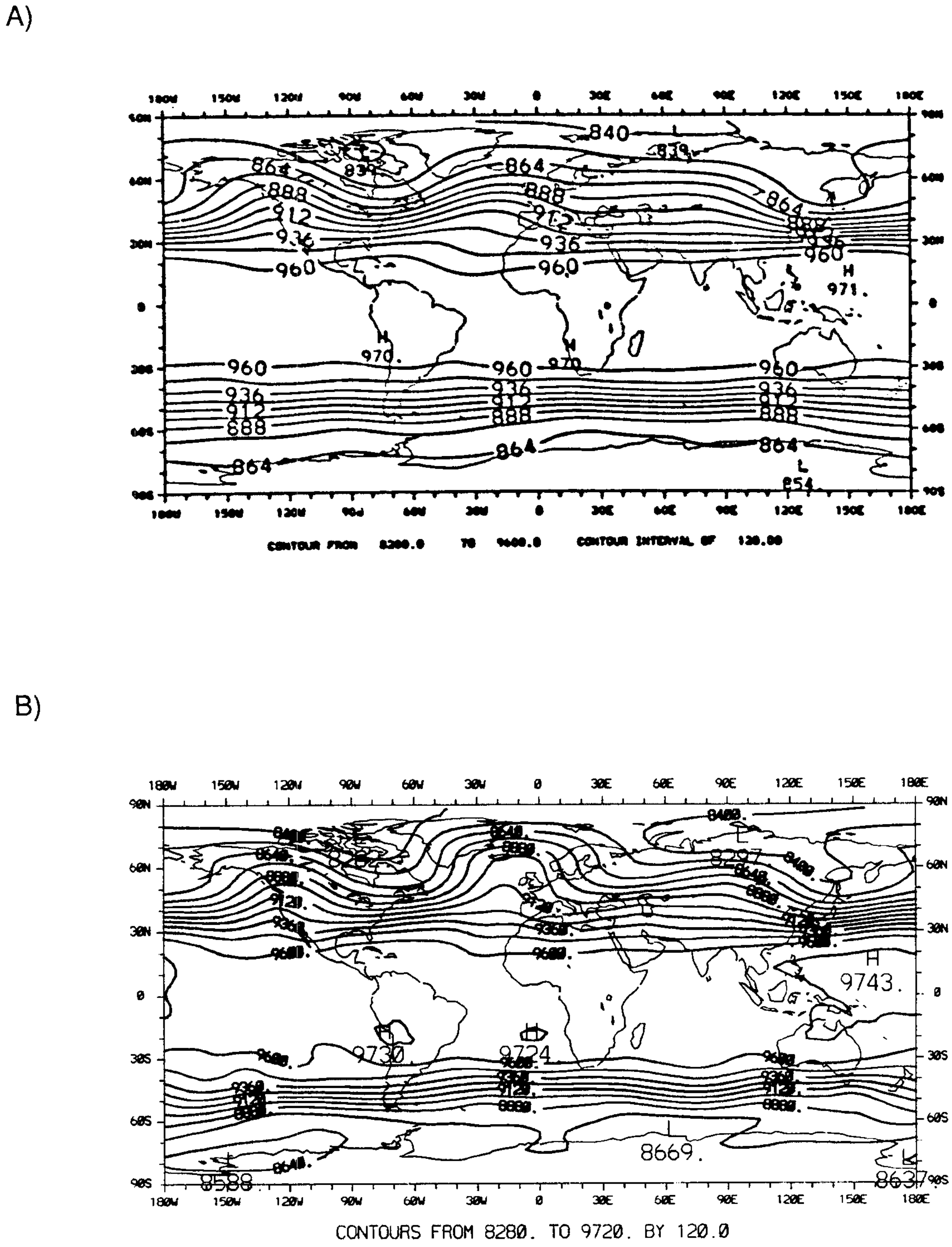

Figure 3.8: ECMWF 300 mb Geopotential Height Field for
A) 1979-1986 January Average (dm)
B) 8-31 January 1987 Average m)

A)

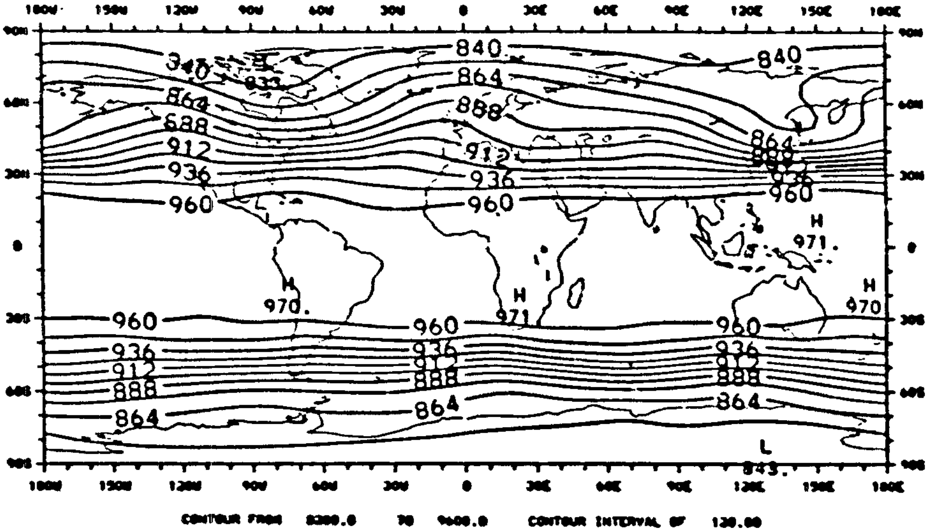

B)

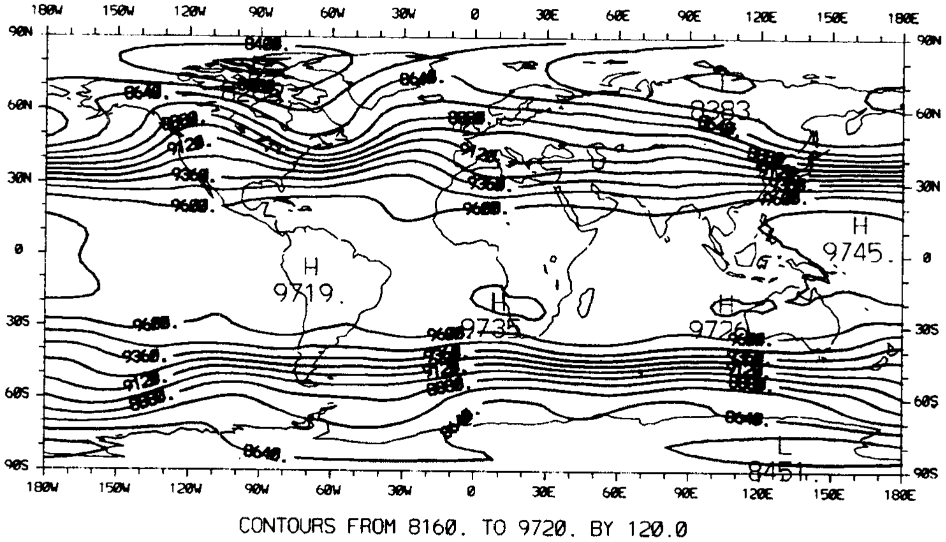

Figure 3.9: ECMWF 300 mb Geopotential Height Field for
A) 1979-1986 February Average (dm)
B) 1-18 February 1987 Average m)

A)

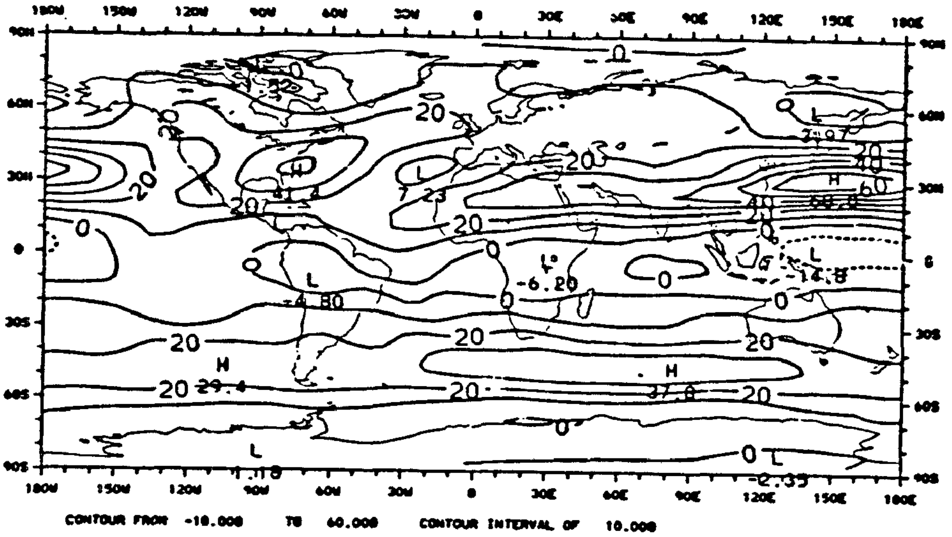

B)

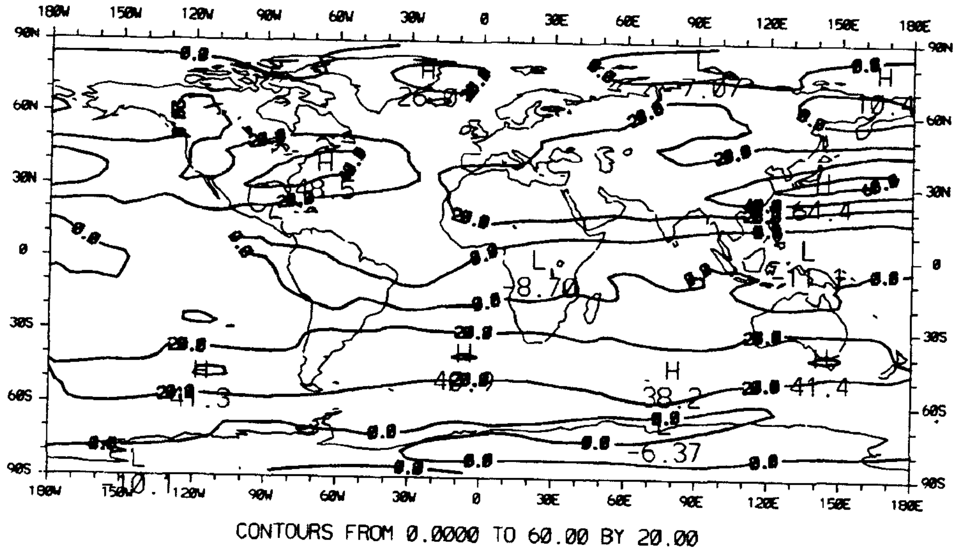

Figure 3.10: ECMWF 300 mb Zonal Wind Field (ms^{-1}) for
A) 1979-1986 January Average
B) 8-31 January 1987 Average

questions across the spectrum of the atmospheric sciences. Chapter 4 presents a comparison between the MSU fields produced in Chapter 2 and various ECMWF fields created using the methods discussed in this chapter. Thermal wind concepts are used as the basis behind many of the comparisons.

CHAPTER 4

COMPARISON OF MSU FIELDS WITH OBSERVED CIRCULATIONS

4.1 INTRODUCTION

This chapter is devoted to the comparison of Microwave Sounding Unit (MSU) observations analyzed in Chapter 2 with European Centre for Medium Range Weather Forecasts (ECMWF) analyses products reviewed in Chapter 3. The overall goal of this comparative study is to explore various applications of MSU radiometric data from an observational viewpoint. Section 4.2 examines the relationship between MSU brightness temperature fields and ECMWF temperature analyses corresponding to MSU Channel 2, 3, and 4 weighting functions. Section 4.3 discusses the relation between thermal wind and meridional temperature gradients with the goal of correlating zonal wind fields to MSU meridional brightness temperature gradients. A similar thermal wind relation is used in Section 4.4 to explore the relation between the MSU brightness temperature anomaly fields and the location of jet stream cores as observed in ECMWF analyses. Section 4.5 takes the thermal wind concept another direction and compares mean-layer temperature as represented by MSU brightness temperature fields to ECMWF geopotential thickness fields. It also examines the relationship between MSU meridional brightness temperature gradients and ECMWF meridional geopotential thickness gradients. Section 4.6 links the thermal structure of the atmosphere as shown by the MSU to its dynamical nature through a comparison of MSU brightness temperature and ECMWF stream function fields. The final section, Section 4.7, discusses the upper-level warming observed north of 50^{o}N latitude by both the MSU and ECMWF data sets between Jan 87 and Feb 87.

4.2 MSU BRIGHTNESS TEMPERATURE AND ECMWF TEMPERATURE FIELDS

This section compares MSU Channels 2, 3, and 4 brightness temperature fields to ECMWF temperature analyses fields. The best correlation between Channel 2 and ECMWF temperature analyses was found to occur in comparison of the 500 mb fields. Figures 4.1a and b show this thermal pattern comparison. Both show a wave number three pattern with absolute temperatures ranging from 225 K to 265 K. Since MSU Channel 2's weighting function peaks at 700mb, one might first assume Figure 4.1a (MSU Channel 2) would more closely correlate with the 700 mb ECMWF field. However, the 700 mb ECMWF temperature field ranges from 240 K to 280 K, 15 degrees warmer than MSU Channel 2. This finding is most likely a result of Channel 2 detecting the relatively cold surface as shown by its weighting function. This is clearly evident in regions of elevated terrain such as the Tibetian Plateau and Greenland, as seen in Figure 4.1a.

MSU Channel 3 brightness temperature best correlates (based on a visual comparison) with ECMWF 300 mb level temperatures, shown as Figures 4.2a and b. Both figures show a 'dipole' pattern cold region over Siberia and relative warm region west of Greenland. Absolute temperatures range from 210 K to 240 K. MSU Channel 3 is colder than ECMWF 300 mb temperatures south of 30^{o}N, where it is detecting the higher cold tropical troposphere with the upper portions of its weighting function (Channel 3's weighting function

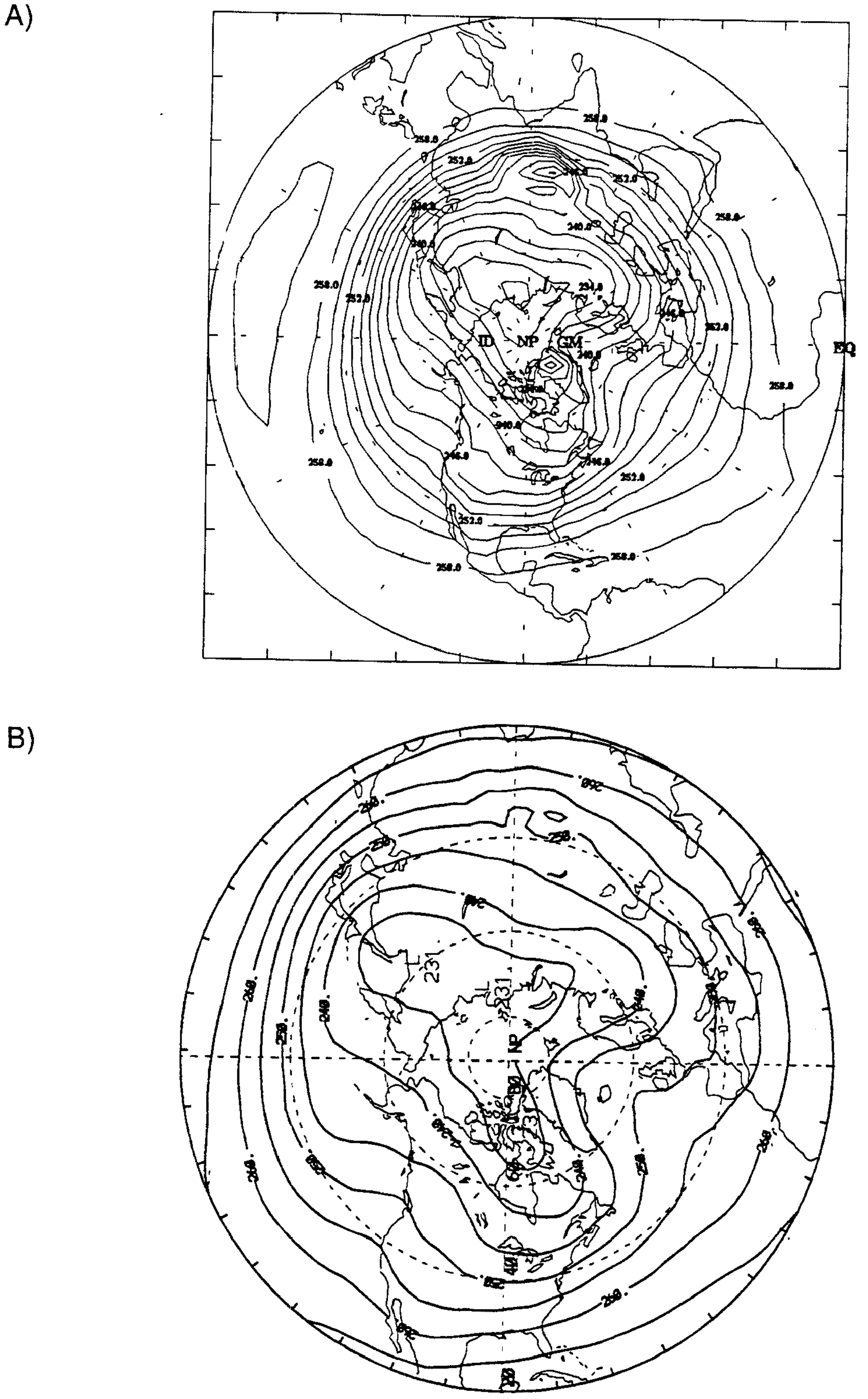

Figure 4.1: Comparison between MSU Channel 2 and ECMWF 500 mb.
A) MSU Channel 2, 8-31 Jan 87, Contour Interval 2 K.
B) ECMWF 500 mb Temperature Field, 8-31 Jan 87, Contour Interval 5K.

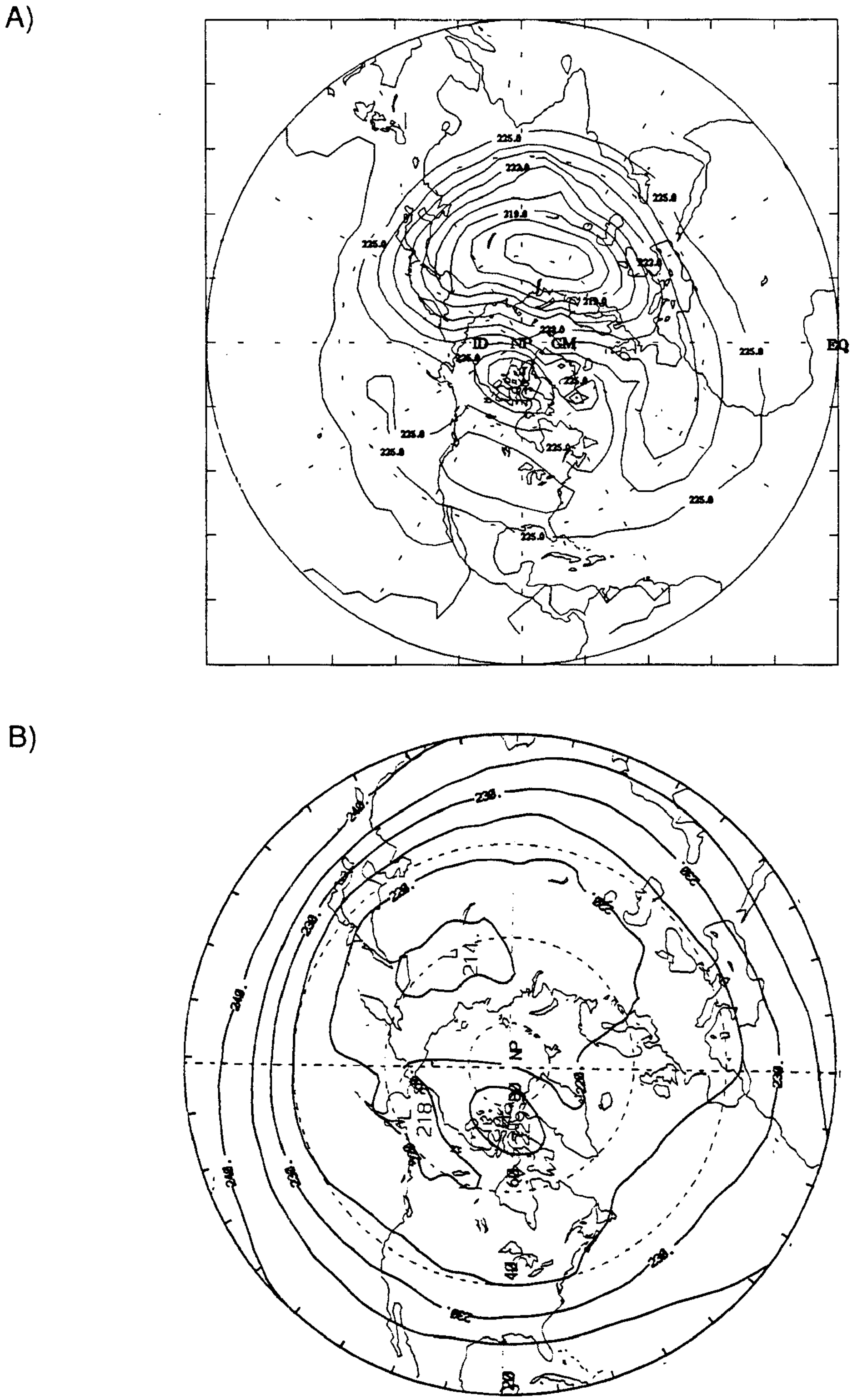

Figure 4.2: Comparison between MSU Channel 3 and ECMWF 300 mb.
A) MSU Channel 3, 1-18 Feb 87, Contour Interval 2 K.
B) ECMWF 300 mb Temperature Field, 1-18 Feb 87, Contour Interval 5K.

A)

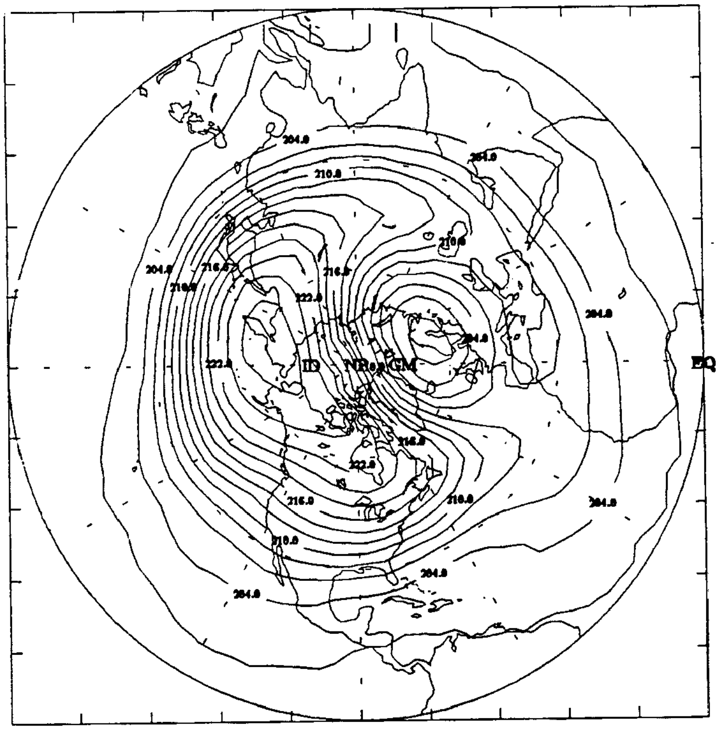

B)

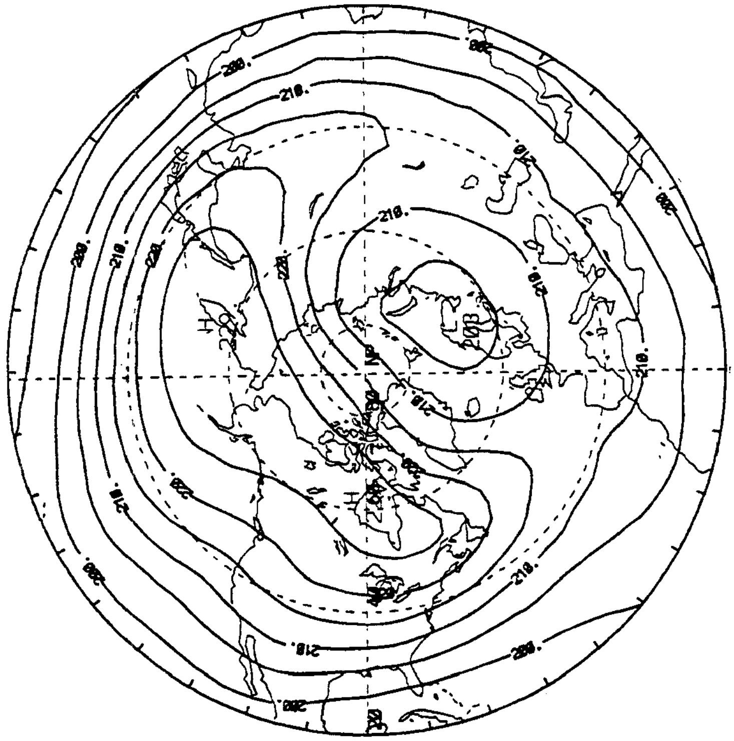

Figure 4.3: Comparison between MSU Channel 4 and ECMWF 100 mb.
A) MSU Channel 4, 8-31 Jan 87, Contour Interval 2 K.
B) ECMWF 100 mb Temperature Field, 8-31 Jan 87, Contour Interval 5K.

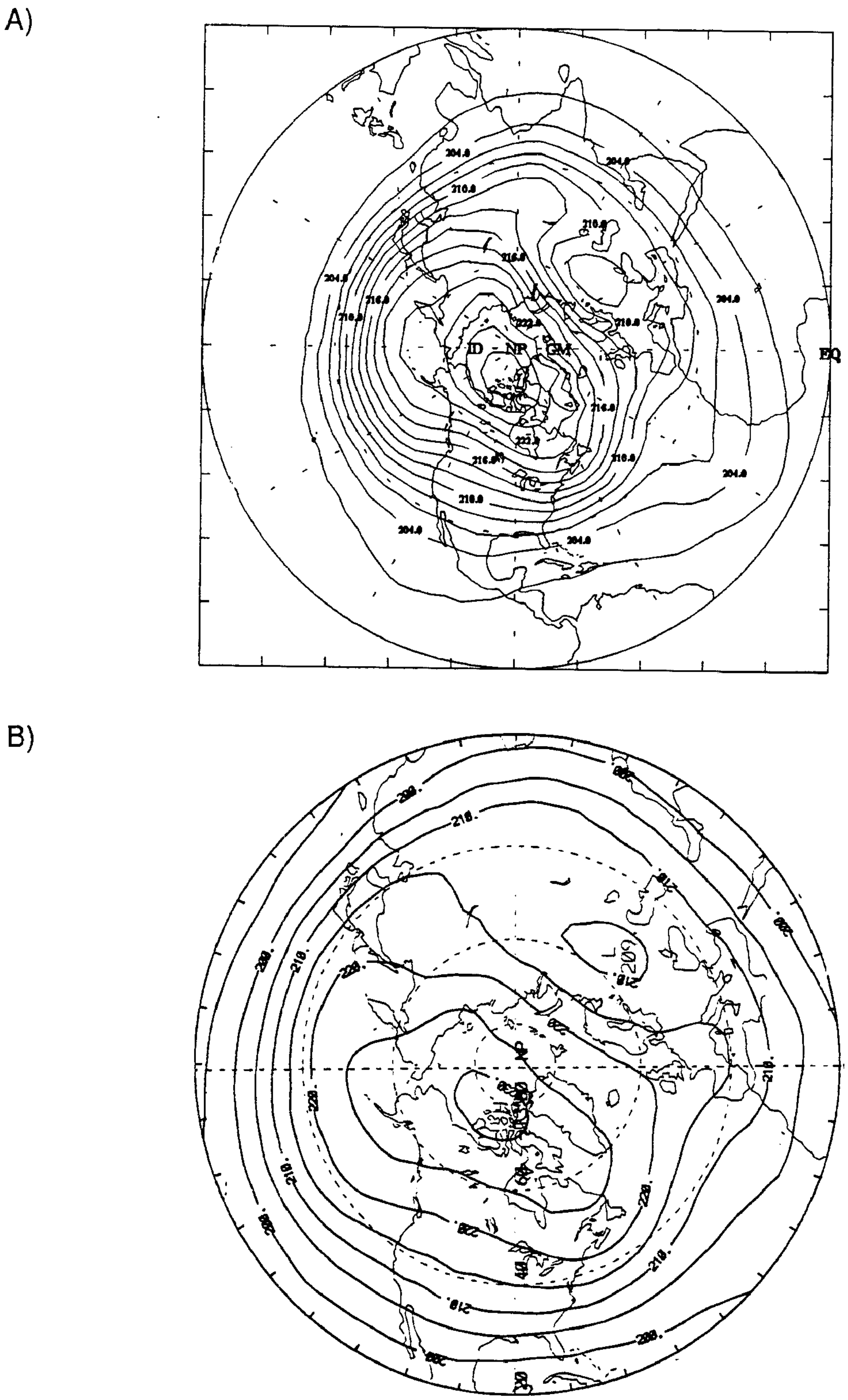

Figure 4.4: Comparison between MSU Channel 4 and ECMWF 100 mb.
A) MSU Channel 4, 1-18 Feb 87, Contour Interval 2 K.
B) ECMWF 100 mb Temperature Field, 1-18 Feb 87, Contour Interval 5K.

peaks near 300 mb). North of 45^{O}N the upper portions of Channel 3's weighting function is instead detecting the lower stratosphere.

The closest temperature correlation occurs between Channel 4 and ECMWF 100 mb level temperatures. This is shown using the 8-31 Jan 87 data set in Figures 4.3a and b, and the 1-18 Feb 87 data set in Figures 4.4a and b. The similarity in thermal patterns is self-evident in both data sets. The cold region centered over Norway during 8-31 Jan is recorded as 200 K by Channel 4, and 203 K by ECMWF 100 mb level. The high over the Kamchatka Peninsula is recorded as 226 K by Channel 4, and 229 K by ECMWF 100 mb. The absolute temperature correlation between Figures 4.4a and b is just as impressive. Channel 4's weighting function peaks near 100 mb and appears to be an excellent indicator of 100 mb temperature.

4.3 THERMAL WIND AND MERIDIONAL TEMPERATURE GRADIENTS

The geostrophic wind model in isobaric coordinates may be written in vectorial form as

$$f\tilde{V}_g = \hat{k} \times \tilde{\nabla}_p \Phi \tag{4.1}$$

with its zonal component written as

$$u_g = -\left.\frac{1}{f}\frac{\partial \Phi}{\partial y}\right)_p \tag{4.2}$$

Differentiating Equation 4.2 with respect to ln p and applying the hydrostatic equation in the form

$$\frac{\partial \Phi}{\partial P} = -\frac{R_d T}{P} \tag{4.3}$$

yields Equation 4.4, a relationship between the rate of change of the zonal component of geostrophic wind with respect to ln p and mean layer temperature

$$\frac{\partial u_g}{\partial(\ln P)} = \frac{R_d}{f}\frac{\partial \bar{T}}{\partial y}\Big) \tag{4.4}$$

Integrating Equation 4.4 from pressure level P_0 to pressure level P_1 ($P_1 < P_0$) the x-component of the thermal wind may be expressed as the difference between zonal geostrophic wind components at P_1 and P_0 , and proportional to the meridional gradient of mean-layer temperature, see Equation 4.5.

$$u_T = u_{g(P_1)} - u_{g(P_0)} = -\frac{R_d}{f}\frac{\partial \bar{T}}{\partial y}\Big)_p \ln\left(\frac{P_0}{P_1}\right) \tag{4.5}$$

If we assume pressure level P_0 to be the surface and $U_{g(P_0)} = 0$, the geostrophic wind at P_1 can be related to meridional mean-layer temperature gradient in the following approximate manner

$$u_{g(P_1)} \approx -\left[\frac{R_d}{f}\ln\frac{P_0}{P_1}\right]\frac{\partial T_{msu}}{dy} \tag{4.6}$$

Since the MSU channels measure radiance emitted from well defined but deep layers of the atmosphere, their brightness temperature fields may be considered a direct measure of mean-layer temperature. The MSU weighting function shown in Figure 2.4 indicates Channel 2's half-power points near 300 mb and below the surface. Therefore, Channel 2's brightness temperature field may be thought of as surface to 300 mb weighted mean-layer temperature. With this assumption, it is expected from Equation 4.6 that MSU meridional brightness temperature gradients from Channel 2 should correlate to the observed zonal wind field at 300 mb. Figures 4.5a and b show the 300 mb ECMWF zonal wind analyses for 8-31 Jan and 1-18 Feb 87. These fields are averaged over the same time period and thus correspond to the MSU Channel 2 brightness temperature fields shown in Figures 2.14a and 2.15a. Neglecting the effects of elevated terrain on Channel 2, the strongest meridional temperature gradients occur southeast of Japan and off the east coast of the US during both months. Figures 4.5a and b both show jet stream maximums at these locations. In the Southern Hemisphere the 300 mb zonal wind maximum is centered along 45^{o}S, which correlates to the the strongest meridional temperature gradients shown in Figures 2.14a and b in the Southern Hemisphere.

Table 4.1 shows a comparison between computed zonal winds from MSU meridional temperature gradients and observed zonal winds from the corresponding ECMWF data sets at 15 random locations. MSU meridional temperature gradients, column 2, are computed from the Channel 2 brightness temperature global data set used to produce Figure 2.14a. Column 3, the 300 mb zonal wind was computed from the 8-31 Jan MSU data set using Equation 4.6 (where $R_d = 287\ m^2 s^{-2}\,{}^oK^{-1}$, and $f=2\Omega\sin\o$). For comparison, the time-averaged ECMWF zonal wind field for 8-31 Jan is shown in Figure 4.5a. However to obtain better accuracy for a comparison with the calculated zonal wind, values in column 4 were instead taken from ECMWF meridional cross-section fields of zonal wind such as the one shown in Figure 3.1b.

Results show that zonal wind calculated from MSU Channel 2 meridional brightness temperature gradients is consistantly under-prediciting the magnitude of the zonal wind as shown in the ECMWF fields. This result is not too suprising considering Channel 2 is a convolution of the surface-to-300 mb mean-layer temperature and the weighting function. To be a true measure the

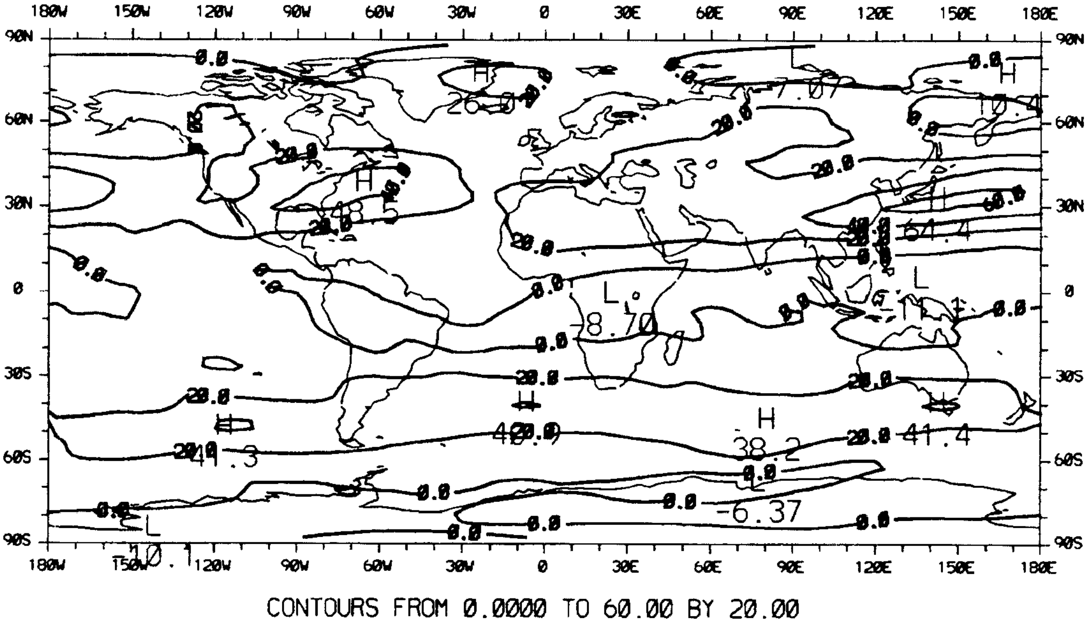

Figure 4.5a: ECMWF 300 mb Zonal Wind Field (8-31 Jan 87)

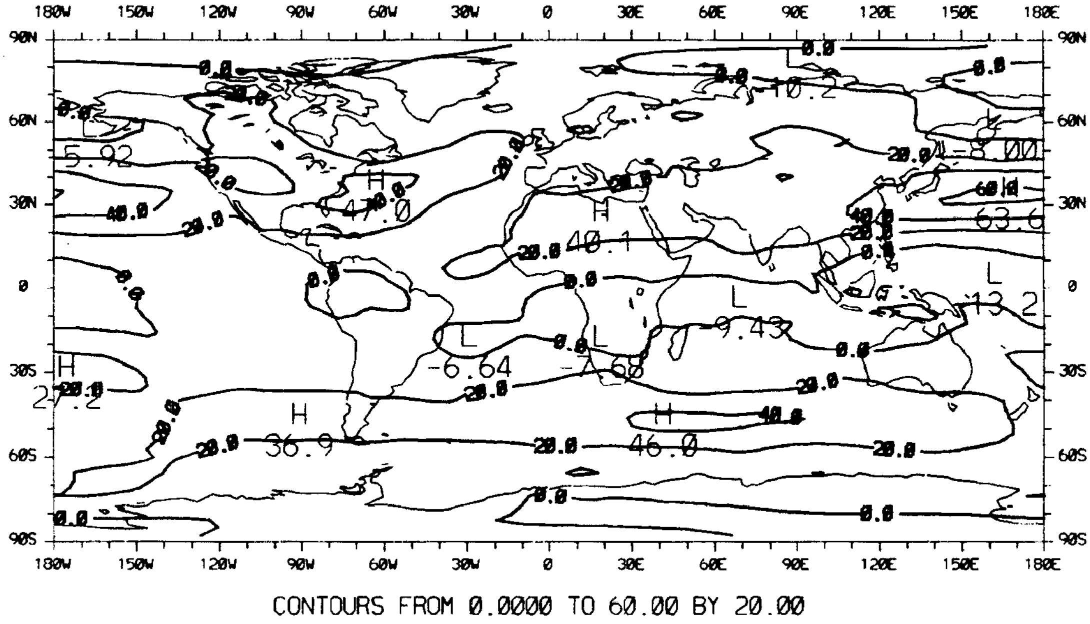

Figure 4.5b: ECMWF 300 mb Zonal Wind Field (1-18 Feb 87)

TABLE 4.1

MSU CALCULATED AND ECMWF GEOSTROPHIC WIND COMPARISON

LATITUDE LONGITUDE	$\frac{\partial T_{msu}}{\partial y}$ (°K m^{-1})	$U_{g(300\ mb)}$ calculated (ms^{-1})	$U_{g(300\ mb)}$ from ECMWF fields (ms^{-1})
60N 160E	7.19×10^{-7}	-1.99	-5
30N 160E	-7.12×10^{-6}	34.39	50
45S 160E	-3.78×10^{-6}	12.78	20
87N 150W	1.80×10^{-6}	-4.3	-7.5
30N 150W	-5.04×10^{-6}	24.09	25
45S 150W	-3.60×10^{-6}	12.17	20
60N 75W	-3.06×10^{-6}	8.48	13
40N 75W	-7.74×10^{-6}	28.79	45
45S 75W	-4.5×10^{-6}	15.21	33
60N 30W	-1.26×10^{-6}	3.49	5
40N 30W	-2.33×10^{-6}	8.67	20
40S 30W	-4.86×10^{-6}	18.08	28
70N 30E	-1.26×10^{-6}	3.2	5
30N 30E	-5.04×10^{-6}	24.09	31
40S 30E	-5.58×10^{-6}	20.75	32

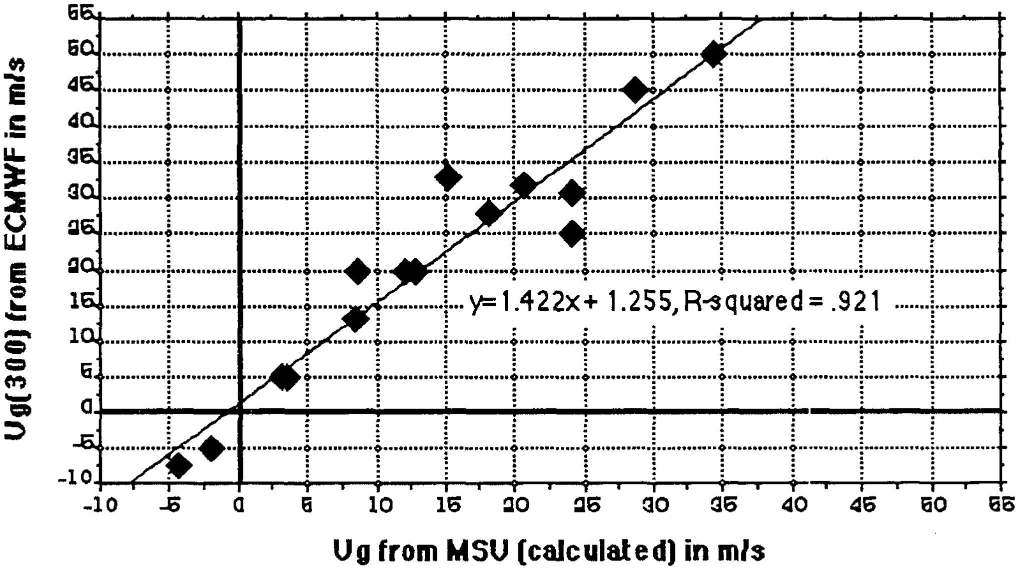

Figure 4.6: Scattergram observations in Table 4.1.

weighting function would need to a vertical line, instead it shows a varying contribution from different pressure levels to the brightness temperature. Another possible reason for this under-predicition lies in the assumptions made deriving Equation 4.6 where the geostrophic wind at the surface was neglected. If the surface winds were subtracted from the ECMWF 300 mb wind, the under-prediction with respect to the calculated would decrease.

As expected though, the strength of the meridional temperature gradient corresponds to strength of the observed (ECMWF) zonal wind, and regions with positive equator to pole brightness temperature gradients show easterly 300 mb flow. A scattergram of the 15 calculated and observed zonal winds in Table 4.1 is shown as Figure 4.6, along with a simple regression curve fit.

4.4 TEMPERATURE ANOMALY AND JET STREAM LOCATION

The Microwave Sounding Unit data sets used in Chapter 2 to produce global brightness temperature fields may be analyzed in a way that provides some potential for locating the core of the jet stream. Section 4.4.1 discusses the methods used to produce MSU brightness temperature anomaly fields shown in this study. Section 4.4.2 contains a review of the thermal wind relation applied to temperature anomaly fields. It also contains a comparison of ECMWF meridional cross-sections of zonal wind with meridional cross-sections of MSU brightness temperature anomaly fields. The goal here is to show a relation between baroclinicity as indicated by the temperature anomaly fields, and the location of the jet core as shown by the ECMWF analyses.

4.4.1 Constructing MSU Brightness Temperature Anomaly Fields

The anomaly fields constructed are defined with respect to the meridional average brightness temperature and derived in the following manner

$$T'_{B,MSU} = \bar{T}_{B,MSU} - T_{B,MSU} \quad (4.7)$$

where $T'_{B,MSU}$ = BrightnessTemperature Anomaly (deviation from meridional average) in ^{O}K,

$T_{B,MSU}$ = Brightness Temperature Value from MSU data set,

$\bar{T}_{B,MSU}$ = Meridional Average MSU Brightness Temperature at a selected longitude (over a specified latitude range).

Figures 4.7a and b are examples of a brightness temperature anomaly fields produced from the 1-18 February 1987 MSU data set for the Northern and Southern Hemisphere. They show meridional cross-sections of brightness temperature anomaly along 165^{O} East longitude, contoured every 1^{O}K. The method used to produce these fields involves interpolation of brightness temperature between MSU channel weighting function peaks.

MSU Channels 2, 3, and 4 provide three temperature data points in the vertical, at 700, 300, and 100 mb, respectively (weighting function peaks). It was shown in Section 4.2 that MSU brightness temperature fields are good approximations of the thermal pattern at pressure levels where the weighting function peaks, with the exception of Channel 2. Brightness temperature values are taken from the grid-averaged MSU data set shown in Figure 2.12c. This provides three temperature data points in the vertical every 2.5^{O} latitude along a meridion from 87.5^{O}S to 87.5^{O}N , one for each MSU channel. The data set is then divided into Northern and Southern Hemisphere files. At this point the brightness temperature values are averaged from equator to pole for

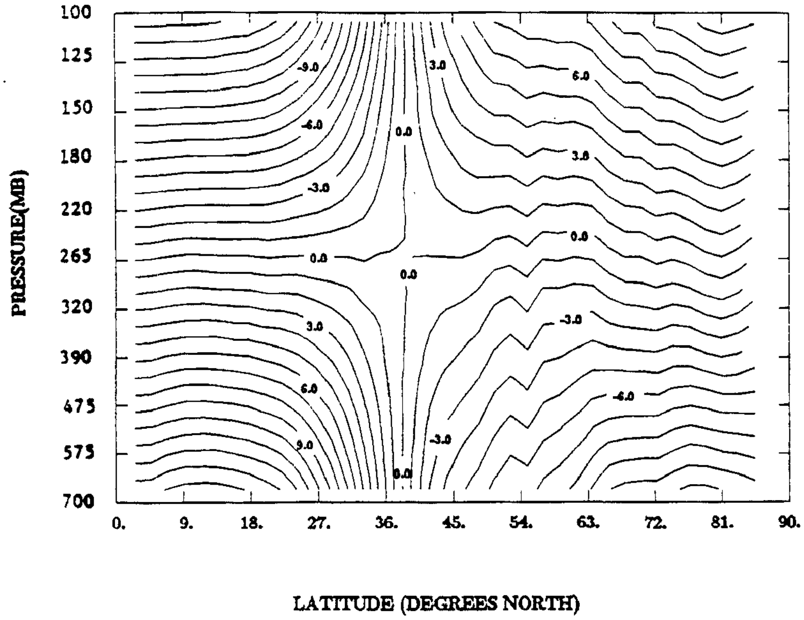

Figure 4.7a: Brightness Temperature Anomaly Field derived from MSU data for Northern Hemisphere along 165^{0}E longitude (contour interval = 1^{0}K)

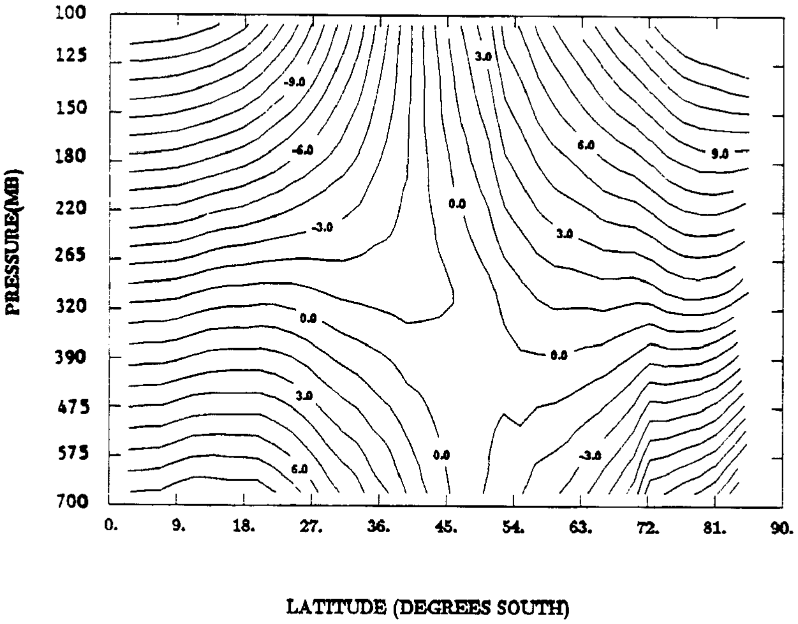

Figure 4.7b: Brightness Temperature Anomaly Field derived from MSU data for Southern Hemisphere along 165^{0}E longitude (contour interval = 1^{0}K)

each MSU channel seperately. The anomaly data set is then computed by taking the difference between the hemispheric average brightness temperature and each 2.5° latitude temperature value. Again this is computed for each MSU channel seperately, resulting in an anomaly data set for each channel. The final step before contouring the field is to interpolate brightness temperature anomaly values every 50 mb between 700 and 300 mb, and between 300 and 100 mb. A simple linear interpolation on a $\log_{10}$ scale was used to create a 13 vertical-level anomaly field (700 to 100 mb, every 50 mb). The anomaly data set used to produce the fields shown in Figure 4.7a and Chapter 4 is therefore a 13 X 35 matrix (13 vertical levels and 35 horizontal data points along the meridion from equator to pole). The NCAR graphics utility CONRAN, used to contour the MSU brightness temperature fields, is then called to contour the matrix at 1°K intervals.

Thermal wind theory dictates the jet core be centered in the 'col' between the two warm and the two cold temperature anomaly regions (Riehl,1962), as discussed in Section 4.4.2.

4.4.2 MSU Temperature Anomaly and ECMWF Jet Core Location

Knowledge of the thermal structure of the atmosphere provides a method for locating jet stream cores (Riehl 1962). Temperature anomaly fields provide an analysis tool for locating jet core position by discerning the thermal structure of the atmosphere. From thermal wind theory it may be shown that the jet stream core is situated at the altitude where the meridional temperature gradient reverses sign. Also, its north-south position can be determined by evaluating temperature gradients along the north-south direction.

The relation between the altitude of the jet stream core and the level of reversal of temperature gradient may be seen using the thermal wind relations shown in Equation 4.4 and 4.6. Equation 4.6 shows the relationship between the geostrophic wind at pressure level P_1 and mean-layer meridional temperature gradient. A positive south-to-north (meridional) temperature gradient indicates negative or easterly zonal flow, and a negative meridional temperature gradient indicates westerly zonal flow. In the mid-latitude troposphere, zonal winds are predominately westerly (and increasing with height, see Equation 4.4) because of a negative equator-to-pole temperature gradient. In the stratosphere, however, meridional temperature gradients are reversed and easterly zonal flow exists, also from Equation 4.4 we see that the positive meridional temperature gradient equates to a decrease in westerly zonal wind with height. The altitude of the jet stream core, the region of strongest westerly flow is therefore expected to occur at the altitude where the meridional temperature gradient reverses. Some attempt to observe this gradient switch is provided using MSU temperature anomaly fields. Figure 4.7a shows negative meridional temperature anomaly gradient below about 350 mb and a positive gradient above this level. From the above argument, 350 mb may be considered an estimate of the jet stream core's altitude.

The north-south position of the jet stream core can be determined using a similar thermal wind argument. The jet core is located where a reversal of the vertical temperature anomaly gradient occurs. From the equator poleward to the jet core temperature anomaly decreases with height resulting in increasing westerly zonal flow. The temperature anomaly from the jet core to the pole temperature anomaly reverses in sign and increases with height indicating decreasing westerly zonal flow. The region of strongest vertical anomaly contour packing correlates to the region of strongest meridional temperature gradient. Equation 4.6 shows the magnitude of zonal wind proportional to the magnitude of meridional temperature gradient In Figure 4.7b, this occurs about 47^{o}S latitude.

In summary, the MSU brightness temperature anomaly fields together with interpolation point to the location of temperature gradient reversals, and hence the jet core, as centered in the 'col' between the two warm (positive) and two cold(negative) temperature anomaly regions.

ECMWF zonal wind meridional cross-section are used to examine the relation between MSU temperature anomaly fields and jet stream altitude and north-south location. Figures 4.8a-c shows time-averaged zonal wind (U) cross-sections for 8 Jan - 31 Jan at 165^{o}E, 110^{o}W, and 75^{o}W longitude. Contours are every 5 ms^{-1} with eastery flow dashed and maximums and minimums labeled. From these figures jet stream core altitude (in mb) and north-south location (in degrees latitude) can be extracted for both hemispheres. Figures 4.9a-f show averaged meridional MSU temperature anomaly cross-sections for the same time period at 165^{o}E, 110^{o}W, and 75^{o}W longitude. Anomaly fields are shown for both the northern and southern hemispheres. In these figures Channel 2 was assumed the temperature at 700 mb, Channel 3 the temperature at 300 mb, and Channel 4 the temperature at 100 mb (weighting function peaks). Figures 4.10a-f shows the same averaged MSU temperature anomaly cross-section except Channel 2 was assumed the temperature at 500 mb (Section 4.2 showed Channel 2 to best represent the 500 mb temperature) and the anomaly field was run from 20^{o}-70^{o} instead of 0^{o}-90^{o}. The latter was done to eliminate polar and equatorial extremes along with Channel 2 cold bias over Greenland and the

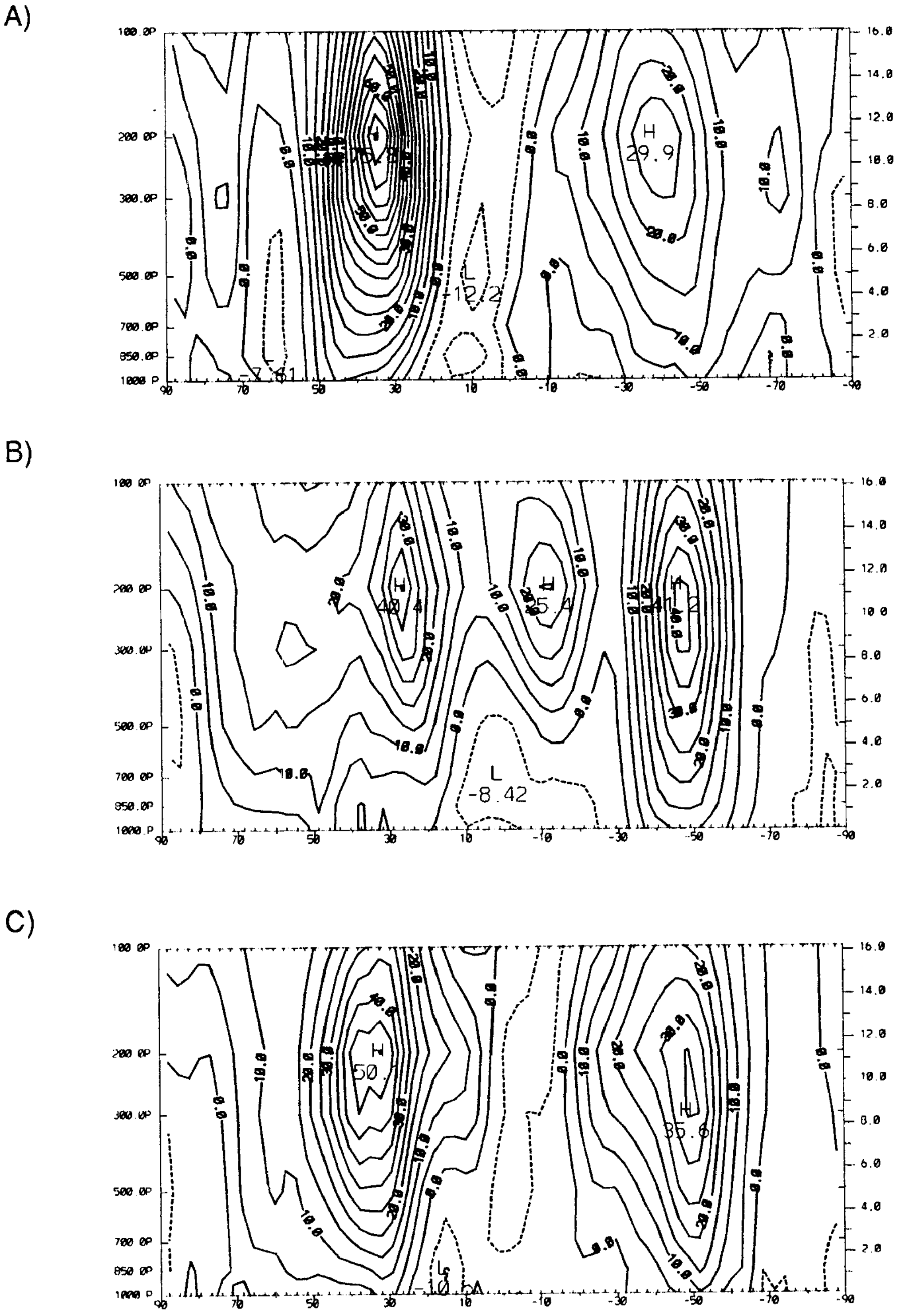

Figure 4.8: ECMWF Zonal Wind Cross-Sections for 8-31 Jan 87 along A) 165 East longitude, B) 110 West longitude, and C) 75 West longitude. All contour intervals are 5 m/s.

Antartica. Jet stream core altitude (in mb) and north-south location (in degrees latitude) can also be extracted from Figures 4.9 and 4.10 by locating the center of the col point. Figures 4.8-11 can be used to show the ability of MSU anomaly fields to locate jet stream cores.

Table 4.2 shows a comparison of jet stream altitude between ECMWF and MSU fields for seven meridions in both hemispheres. Column 1 show the location of the comparison, column 2 shows jet altitude from ECMWF U fields similar to Figure 4.8, column 3 shows jet altitude from MSU temperature anomaly fields similar to Figure 4.9, and column 4 shows jet altitude from MSU temperature anomaly fields similiar to Figure 4.10. Figures 4.11a-b are scattergrams of the observations in Table 4.2 for the Northern and Southern Hemispheres, respectively. In both hemispheres the MSU anomaly fields predict a jet core altitude lower than that shown in the ECMWF fields. The difference is mostly a result of treating the MSU brightness temperature as a constant pressure-level temperature. As seen from its weighting function curve, MSU channels measure over a large vertical range. From Section 4.2 it was shown that Channel 2 most closely resembled 500 mb temperature instead of the temperature at the level where its weighting function peaked. Figure 4.11 consistently shows a closer altitude comparison when Channel 2 was taken as 500 mb temperature.

Table 4.3 shows a comparison of jet stream north-south location between ECMWF and MSU fields using the same meridional locations, and Figure 4.12 is a scattergram of the results. In both hemispheres the MSU anomaly fields show the jet location poleward of the ECMWF field's location. Changing Channel 2 to 500 mb and running the anomaly field from 20^{o}-70^{o} had little (only a slight poleward push) effect on north-south location of the jet. The

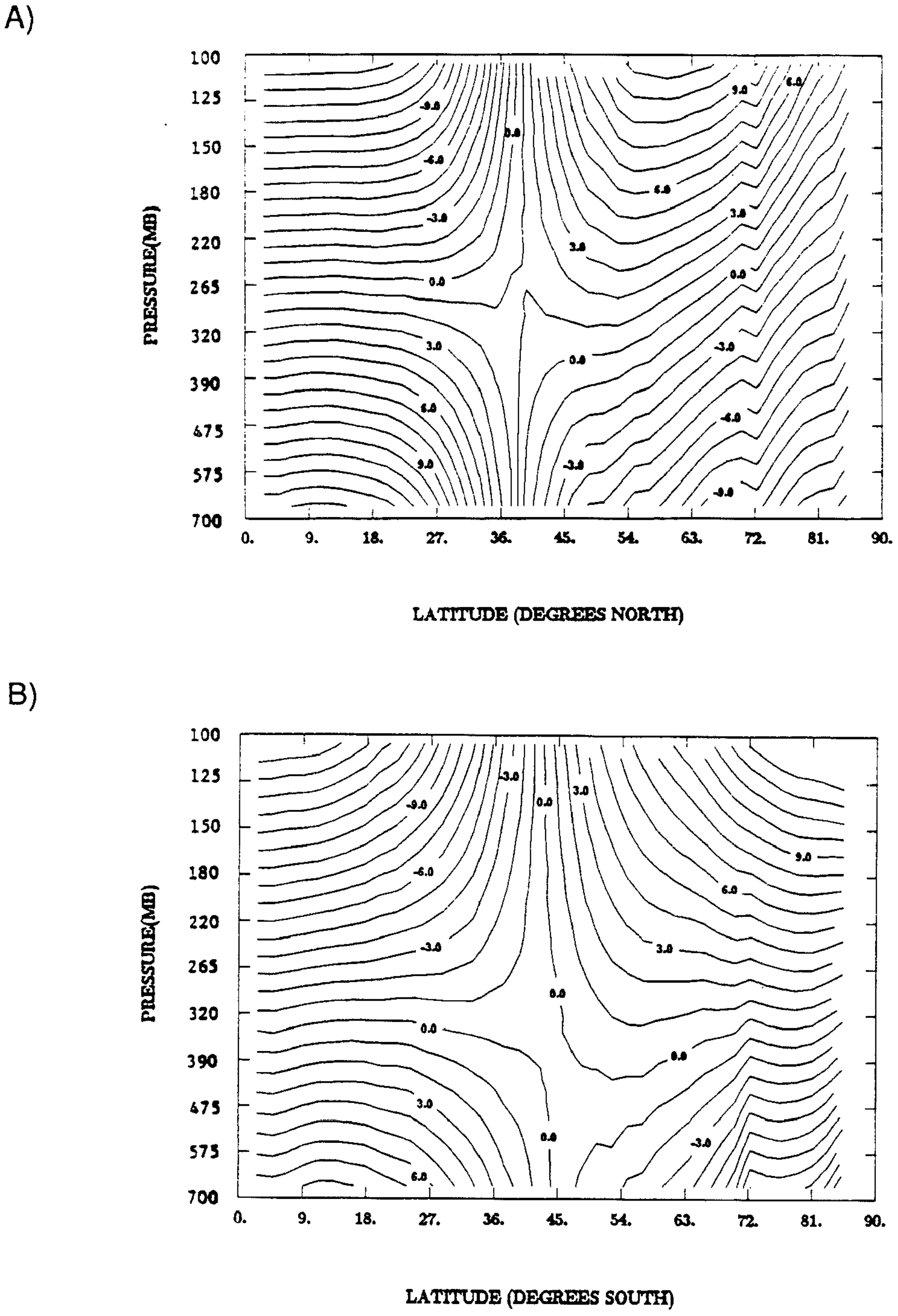

Figure 4.9: MSU Temperature Anomaly Fields for 8-31 Jan 87 along A) 165^{o} East (NH), B) 165^{o} East (SH), C) 110^{o} West (NH), D) 110^{o} West (SH), E) 75^{o} West (NH), F) 75^{o} West (SH). Anomaly fields are determined using CH2=700 mb, CH3=300 mb, and CH4=100mb and run from 2.5 - 87.5^{o} latitude.

C)

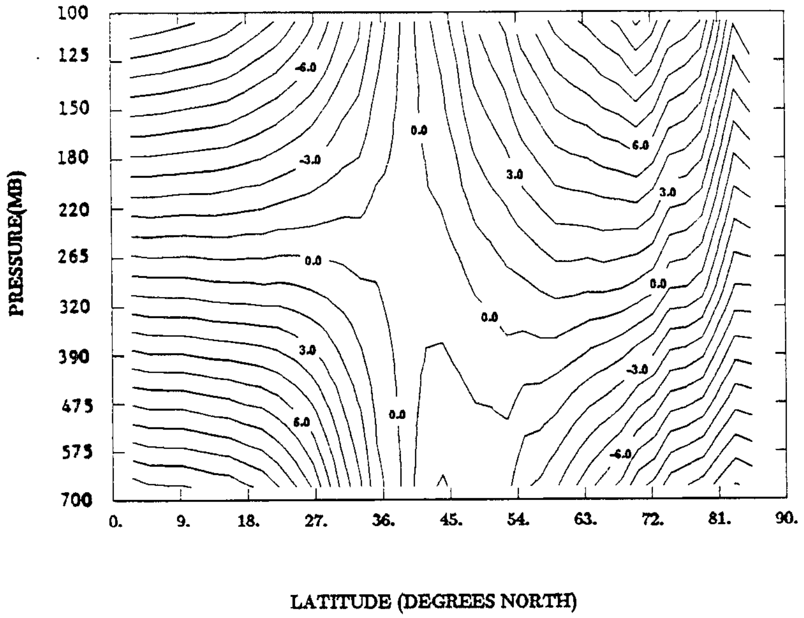
PRESSURE(MB)
100
125
150
180
220
265
320
390
475
575
700
0.
9.
18.
27.
36.
45.
54.
63.
72.
81.
90.
LATITUDE (DEGREES NORTH)
-6.0
-3.0
0.0
0.0
3.0
6.0
3.0
0.0
6.0
3.0
0.0
0.0
3.0
-3.0
-6.0

D)

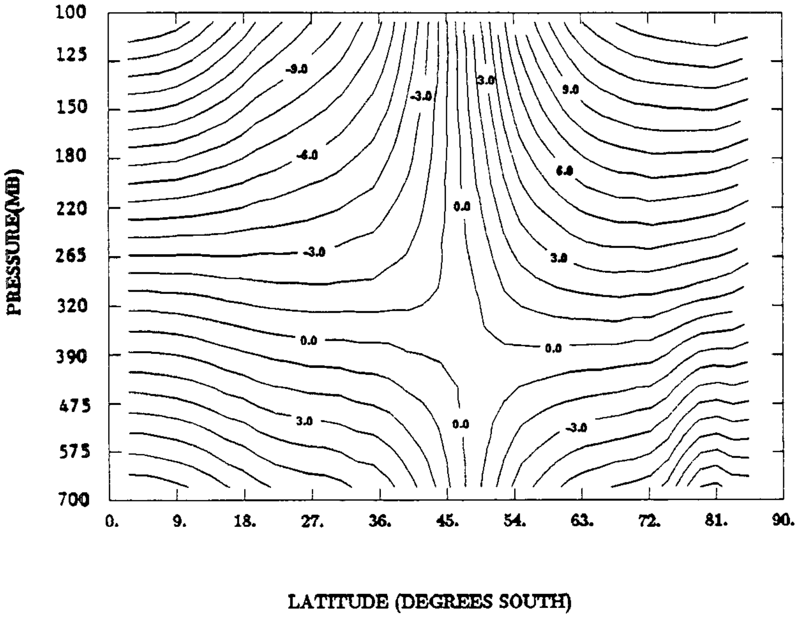
PRESSURE(MB)
100
125
150
180
220
265
320
390
475
575
700
0.
9.
18.
27.
36.
45.
54.
63.
72.
81.
90.
LATITUDE (DEGREES SOUTH)
-9.0
-3.0
3.0
9.0
-6.0
6.0
0.0
-3.0
3.0
0.0
0.0
3.0
0.0
-3.0

E)

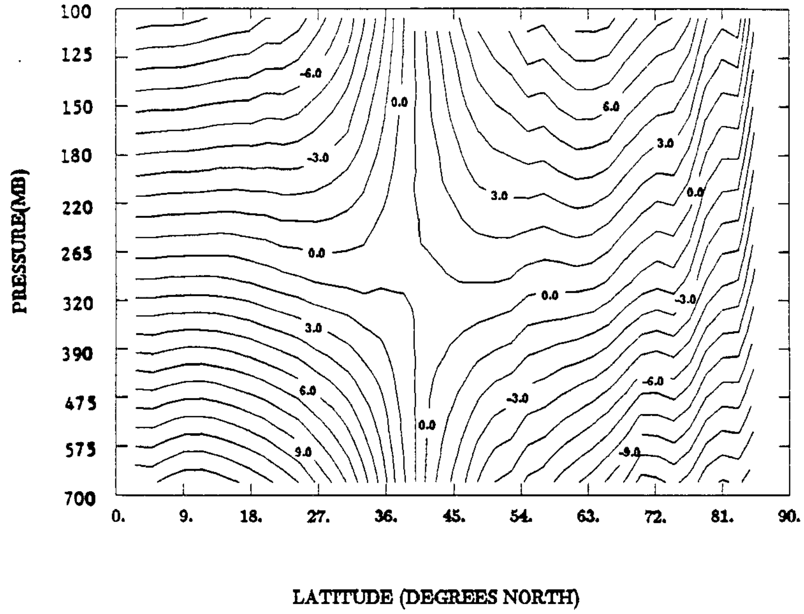
PRESSURE(MB)
100
125
150
180
220
265
320
390
475
575
700
0.
9.
18.
27.
36.
45.
54.
63.
72.
81.
90.
LATITUDE (DEGREES NORTH)
-6.0
0.0
-3.0
0.0
3.0
6.0
9.0
0.0
6.0
3.0
3.0
0.0
0.0
-3.0
-3.0
-6.0
-9.0

F)

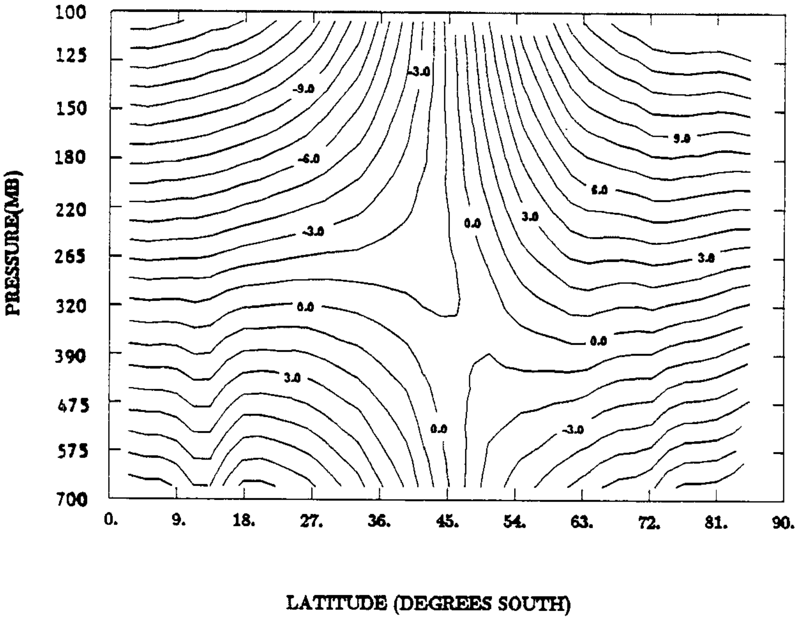
PRESSURE(MB)
100
125
150
180
220
265
320
390
475
575
700
0.
9.
18.
27.
36.
45.
54.
63.
72.
81.
90.
LATITUDE (DEGREES SOUTH)
-3.0
-9.0
-6.0
-3.0
0.0
3.0
0.0
0.0
3.0
6.0
9.0
3.0
0.0
-3.0

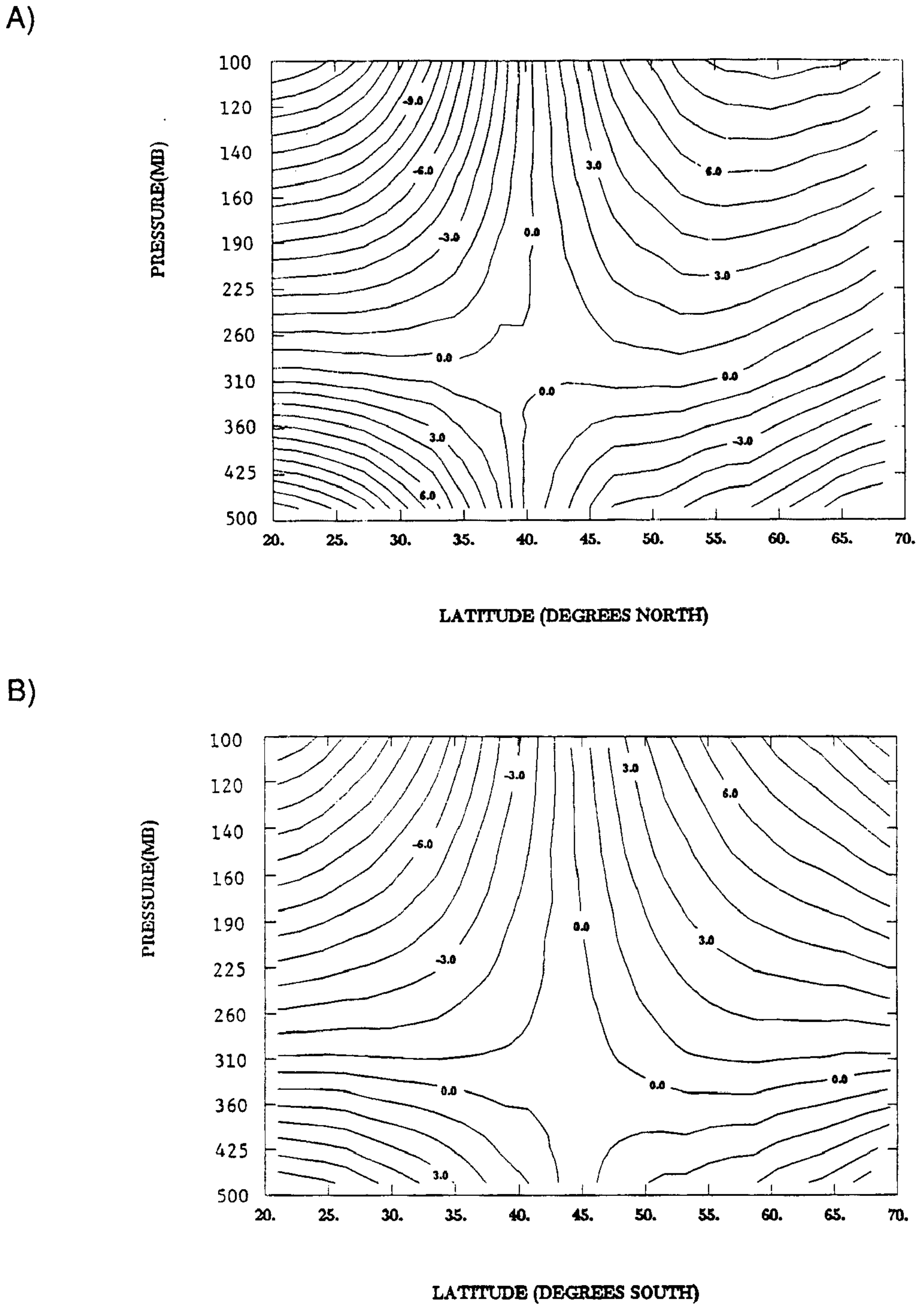

Figure 4.10: MSU Temperature Anomaly Fields for 8-31 Jan 87 along A) 165° East (NH), B) 165° East (SH), C) 110° West (NH), D) 110° West (SH), E) 75° West (NH), F) 75° West (SH). Anomaly fields are determined using CH2=500 mb, CH3=300 mb, and CH4=100mb and run from 20 -70° latitude.

C)

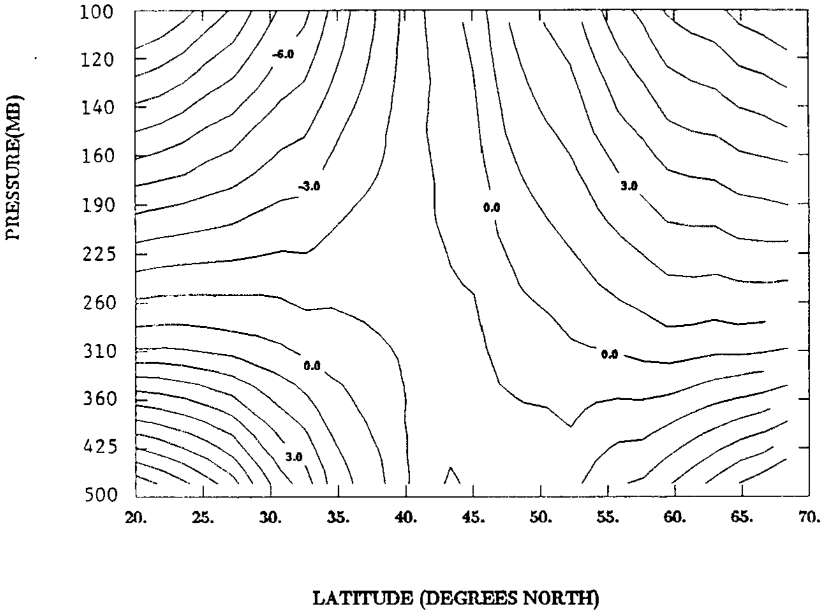
PRESSURE(MB)
100
120
140
160
190
225
260
310
360
425
500
-6.0
-3.0
0.0
3.0
0.0
0.0
3.0
20.
25.
30.
35.
40.
45.
50.
55.
60.
65.
70.
LATITUDE (DEGREES NORTH)

D)

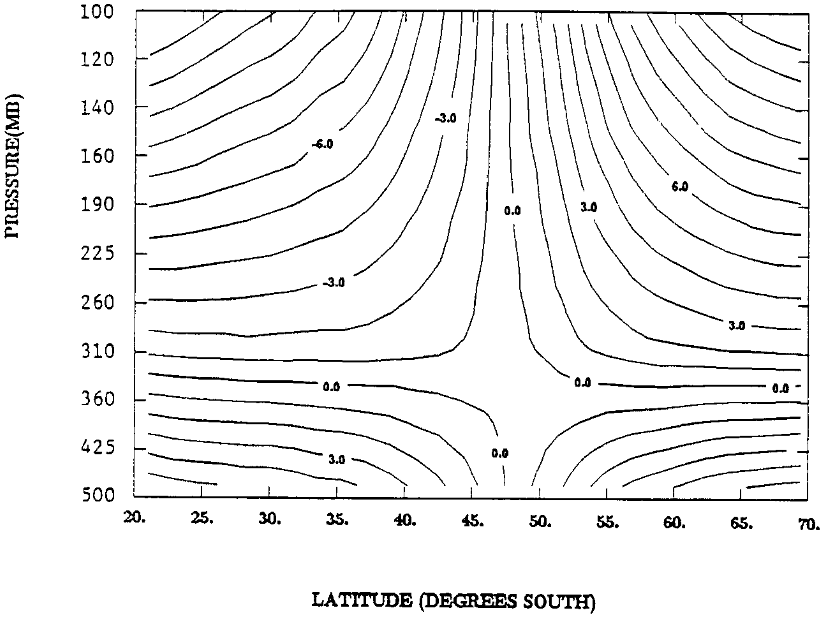
PRESSURE(MB)
100
120
140
160
190
225
260
310
360
425
500
-3.0
-6.0
0.0
3.0
6.0
-3.0
3.0
0.0
0.0
0.0
3.0
0.0
20.
25.
30.
35.
40.
45.
50.
55.
60.
65.
70.
LATITUDE (DEGREES SOUTH)

E)

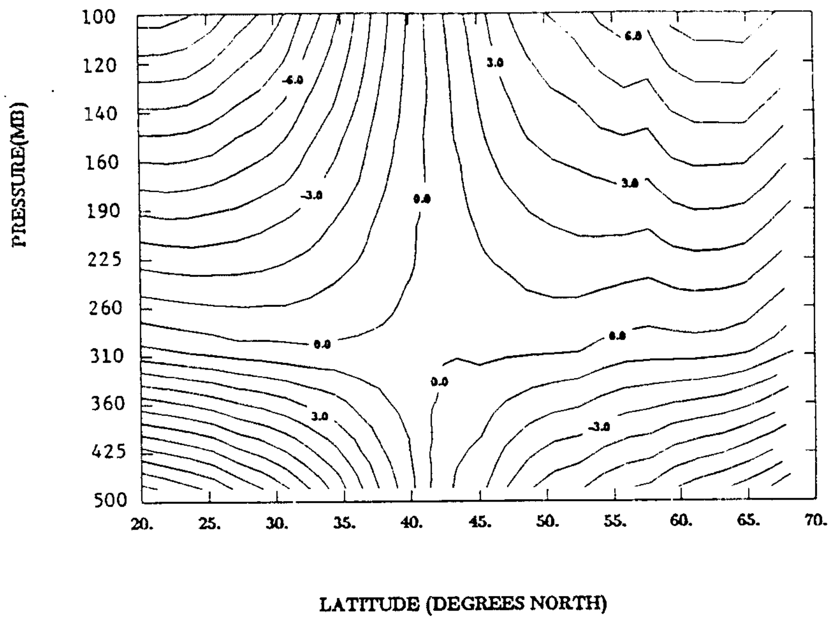
100
120
140
160
190
225
260
310
360
425
500
PRESSURE(MB)
20.
25.
30.
35.
40.
45.
50.
55.
60.
65.
70.
LATITUDE (DEGREES NORTH)
-6.0
3.0
6.0
-3.0
0.0
3.0
0.0
0.0
0.0
3.0
-3.0

F)

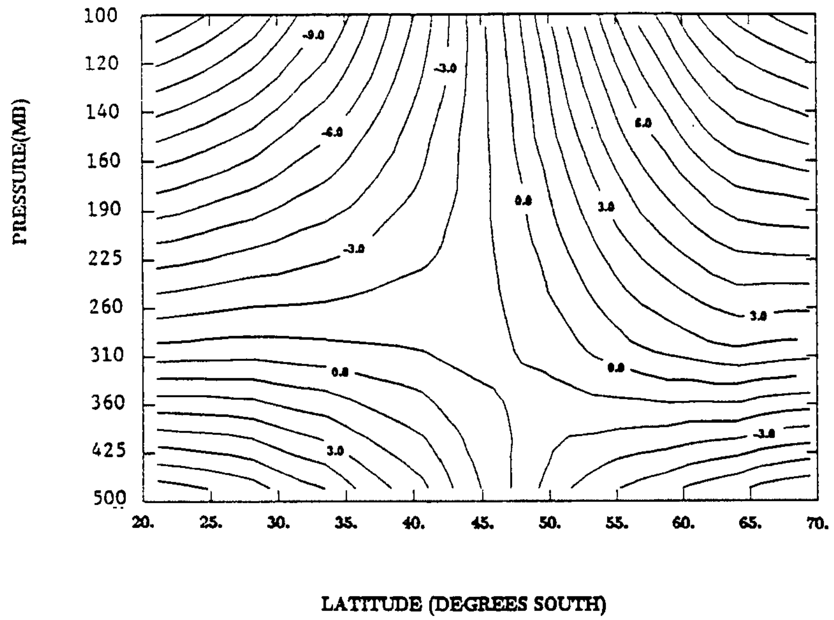
100
120
140
160
190
225
260
310
360
425
500
PRESSURE(MB)
20.
25.
30.
35.
40.
45.
50.
55.
60.
65.
70.
LATITUDE (DEGREES SOUTH)
-9.0
-3.0
-6.0
6.0
0.0
3.0
-3.0
3.0
0.0
0.0
-3.0
3.0

TABLE 4.2

JET STREAM ALTITUDE USING ECMWF AND MSU DATA

LONGITUDE	JET ALTITUDE IN MB (ECMWF)	JET ALTITUDE IN MB (MSU 700/300/100)	JET ALTITUDE IN MB (MSU 500/300/100)
150W NH	200	380	330
SH	250	380	350
110W NH	200	280	240
SH	250	390	340
75W NH	200	280	260
SH	260	360	320
30W NH	200	220	200
SH	200	350	330
30E NH	200	180	180
SH	210	350	330
100E NH	200	220	220
SH	220	390	340
165E NH	200	270	270
SH	200	390	350

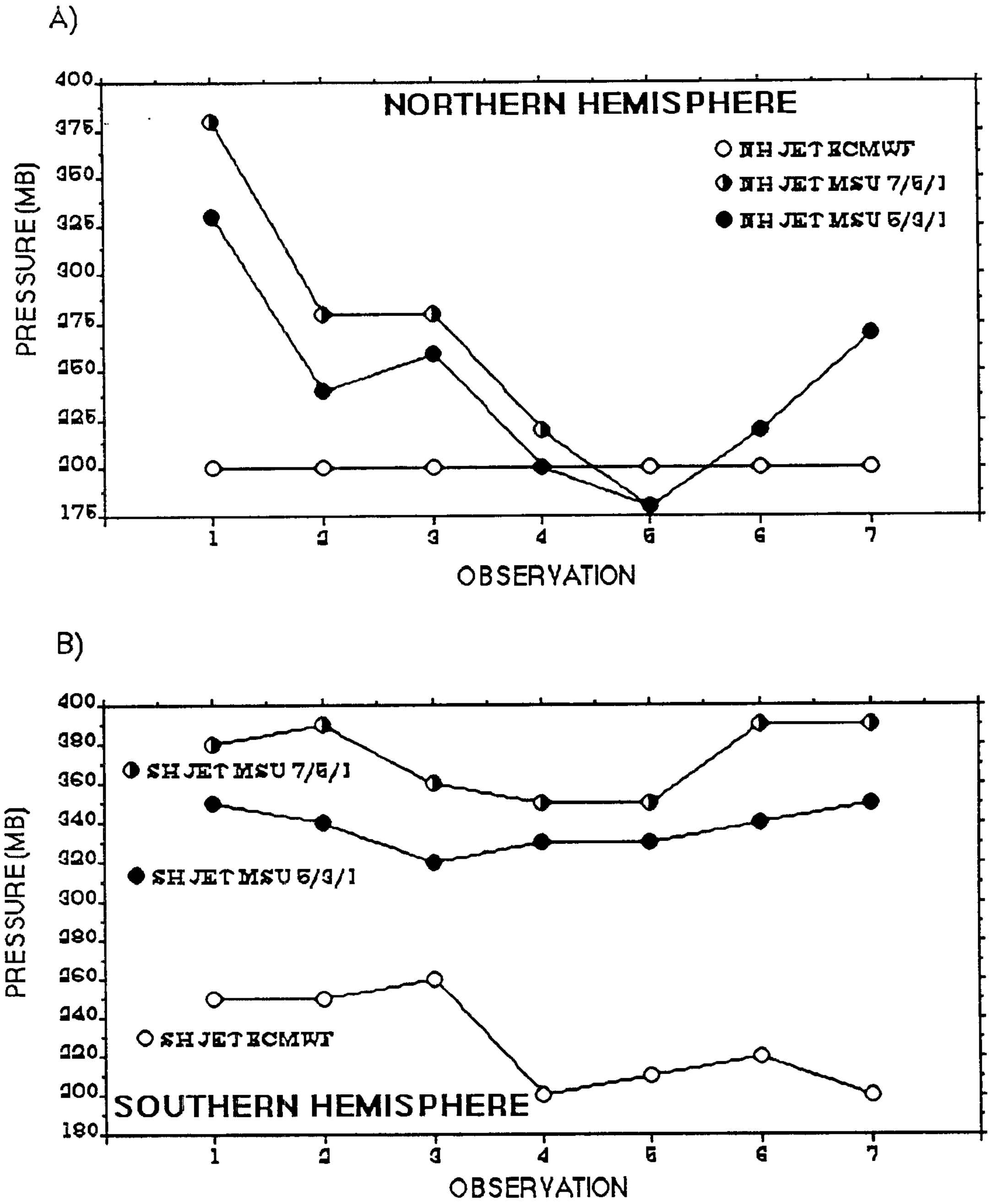

Figure 4.11: Scattergram of Observations in Table 4.2 for (Jet Stream Core Altitude A) the Northern Hemisphere, and B) the Southern Hemisphere.

TABLE 4.3

JET STREAM LOCATION USING ECMWF AN MSU DATA

LONGITUDE	JET LOCATION DEG. LAT. (ECMWF)	JET LOCATION DEG. LAT. (MSU 700/300/100)	JET LOCATION DEG. LAT. (MSU 500/300/100)
150W NH SH	33N 51 S	40N 50 S	40N 49 S
110W NH SH	28N 46 S	40N 48 S	40N 48 S
75W NH SH	33N 49 S	39N 48 S	41N 48 S
30W NH SH	35N 38 S	39N 43 S	40N 44 S
30E NH SH	28N 39 S	32N 46 S	35N 44 S
100E NH SH	32N 44 S	35N 49N	37N 47S
165E NH SH	35N 39 S	38N 44 S	41N 44 S

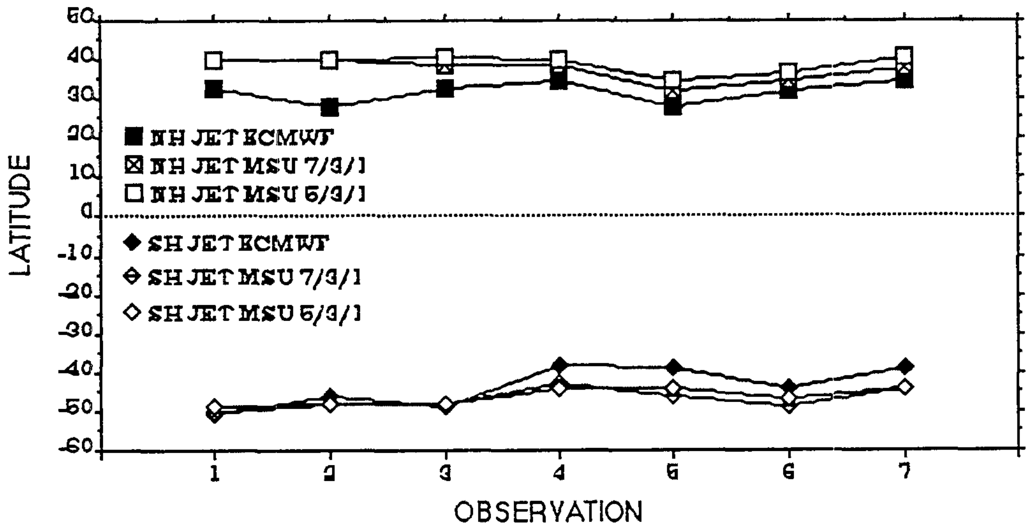

Figure 4.12: Scattergram of Observations in Table 4.3, showing latitudinal position of jet stream core from ECMWF and MSU data.

disagreement between the MSU observations and ECMWF analyses of the latitudinal position of zonal wind maxima is perhaps surprising especially since this disagreement, for the cases examined, is largest in the Northern Hemisphere. Further, more quantitative analysis of this correlation is required to establish whether this disagreement is a persistent one.

There are many sources of error involved in using MSU brightness temperature anomaly fields to locate jet stream cores. The nature of the weighting function as previously described, using linear interpolation between pressure-levels, and poor vertical resolution itself (only 3 channels). Using a temperature retrieval technique would yield better results as would more channels in the vertical with sharper-peaked weighting fuctions.

Another investigation of the anomaly fields to locate the jet core's latitudinal position could be undertaken by assigning N-S at the region of maximum meridional anomaly gradient. This would push the MSU predicted position equatorward, closer to the ECMWF position.

Figures 4.13a-b shows temperature anomaly fields constructed using ECMWF temperature anomalies along 165^{o}E, and 110^{o}W in the northern hemisphere. These figures were constructed using the same procedure as MSU temperature anomaly fields (700, 300, and 100 mb temperature anomaly values with linear interpolation every 50 mb inbetween). Jet stream altitude and north-south location are both much closer to those shown in the corresponding Figures 4.8a and b. This suggests that just applying a temperature retrieval scheme, obtaining 700, 300, and 100 mb temperatures from MSU data, may significantly improve the MSU anomaly field's ability to show jet stream core altitude and location.

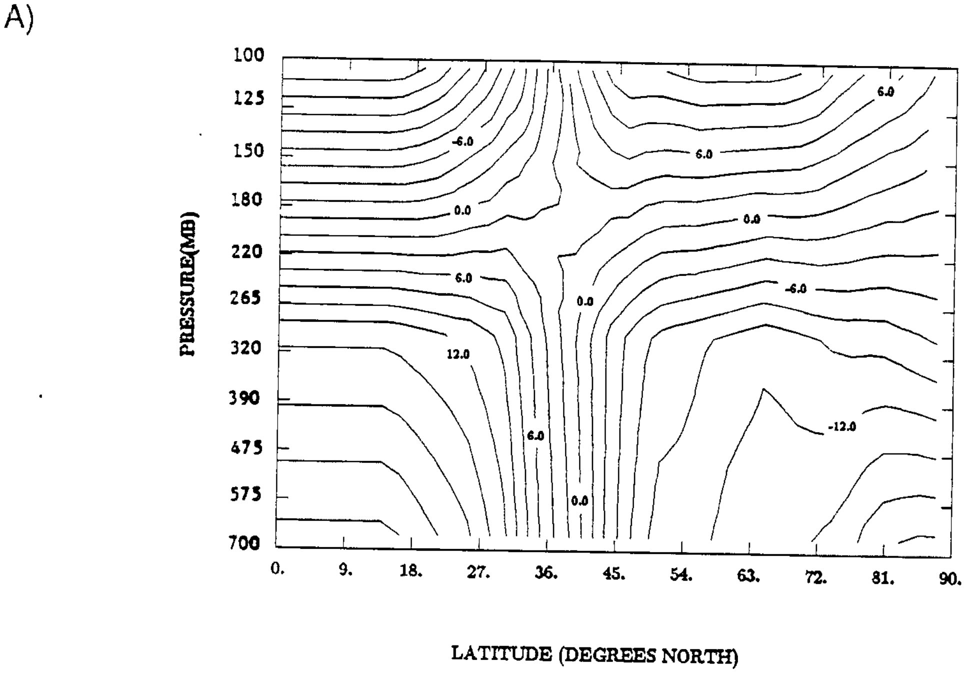

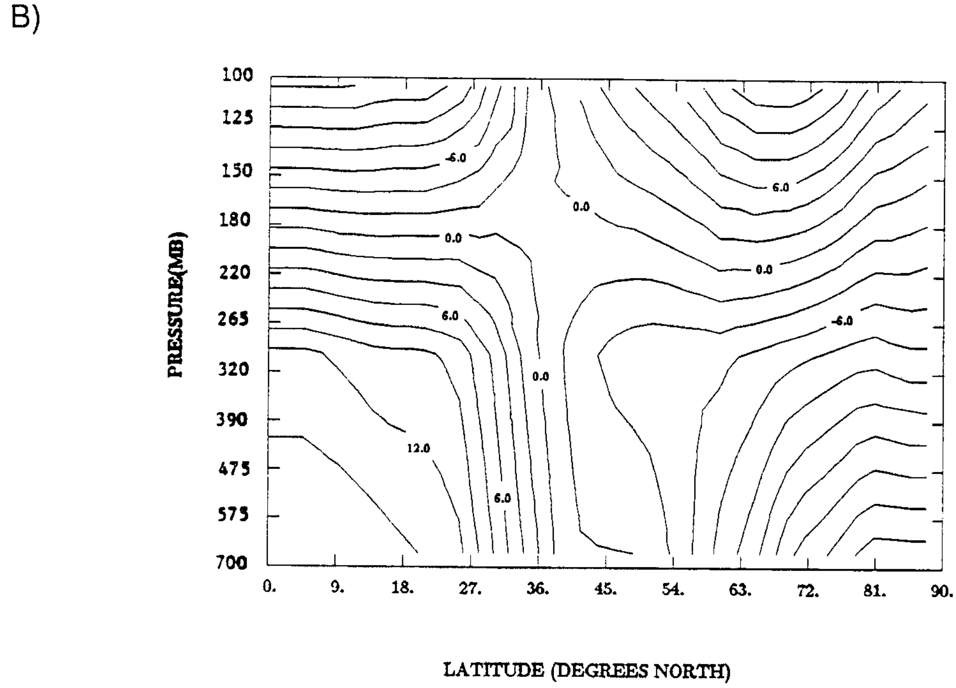

Figure 4.13: ECMWF Temperature Anomaly Fields for
A) 165° East longitude (NH), and B) 110° West longitude (NH).

4.5 THERMAL WIND AND GEOPOTENTIAL THICKNESS GRADIENT

This section explores another method of using the thermal wind concept to compare MSU temperature fields with observed ECMWF analyses. Section 4.5.1 examines the relation between MSU meridional brightness temperature gradients and ECMWF meridional geopotential thickness gradients. Section 4.5.2 compares MSU 'mean-layer' temperature fields with ECMWF geopotential thickness.

4.5.1 Temperature and Geopotential Thickness Gradients

Using the x-component of the geostrophic wind model in isobaric coordinates in Equation 4.2, a mathematical relationship between meridional temperature gradients and geopotential thickness gradients may be derived. Differentiating Equation 4.2 with respect to P yields the following

$$\frac{\partial u_g}{\partial P} = -\frac{1}{f}\frac{\partial}{\partial y}\left(\frac{\partial \Phi}{\partial P}\right) \tag{4.7}$$

By integrating Equation 4.7 from pressure level P_0 to pressure level P_1 ($P_1 < P_0$), and assuming $U_{g(P_0)} = 0$ we obtain

$$u_{g(P_1)} = -\frac{1}{f}\frac{\partial}{\partial y}(\Phi_0 - \Phi_1) \tag{4.8}$$

This expression shows the relationship between the geostrophic wind at level P_1 and meridional geopotential thickness gradient between P_1 and P_0. Substituting Equation 4.6 into 4.8 yields

$$\frac{\partial T_{msu}}{\partial y} = \left[R_d \ln\left(\frac{P_o}{P_1}\right)\right]^{-1} \frac{\partial(\Delta\Phi)}{\partial y} \tag{4.9}$$

indicating that the meridional brightness temperature gradient is proportional to the meridional geopotential thickness gradient.

An observational test of this relationship is presented by comparing MSU brightness temperature fields and ECMWF geopotential thickness fields. Channel 2, as shown by its weighting function, may be considered representative of the 850 - 300 mb weighted mean-layer temperature. Therefore, Channel 2 meridional temperature gradients should correspond approximately to ECMWF 850 - 300 mb thickness gradients. In the same way, Channel 4 meridional temperature gradients should correspond to ECMWF 200 - 100 mb thickness gradients (100 mb is the highest level available for ECMWF analyses).

Figures 4.14a and b provides a comparison of the MSU Channel 2 brightness temperatures and the ECMWF 850-300 mb geopotential thickness gradients for 8-31 Jan 87. The MSU observed thermal pattern and the ECMWF thickness pattern are remarkably similar except over the previously highlighted regions of elevated terrain. Regions of strong thermal gradients correspond to regions of strong thickness gradients, such as south of Japan and over the US east coast. Likewise, regions of weak thermal gradients correspond to regions of weak thickness gradients, such as over the North Atlantic Ocean and off the US west coast. Table 4.4 presents the results of several random numerical calculations using the data sets used to produce Figures 4.14a and b. Column 1 shows the meridional region used to make the calculations, column 2 shows the MSU Channel 2 meridional temperature

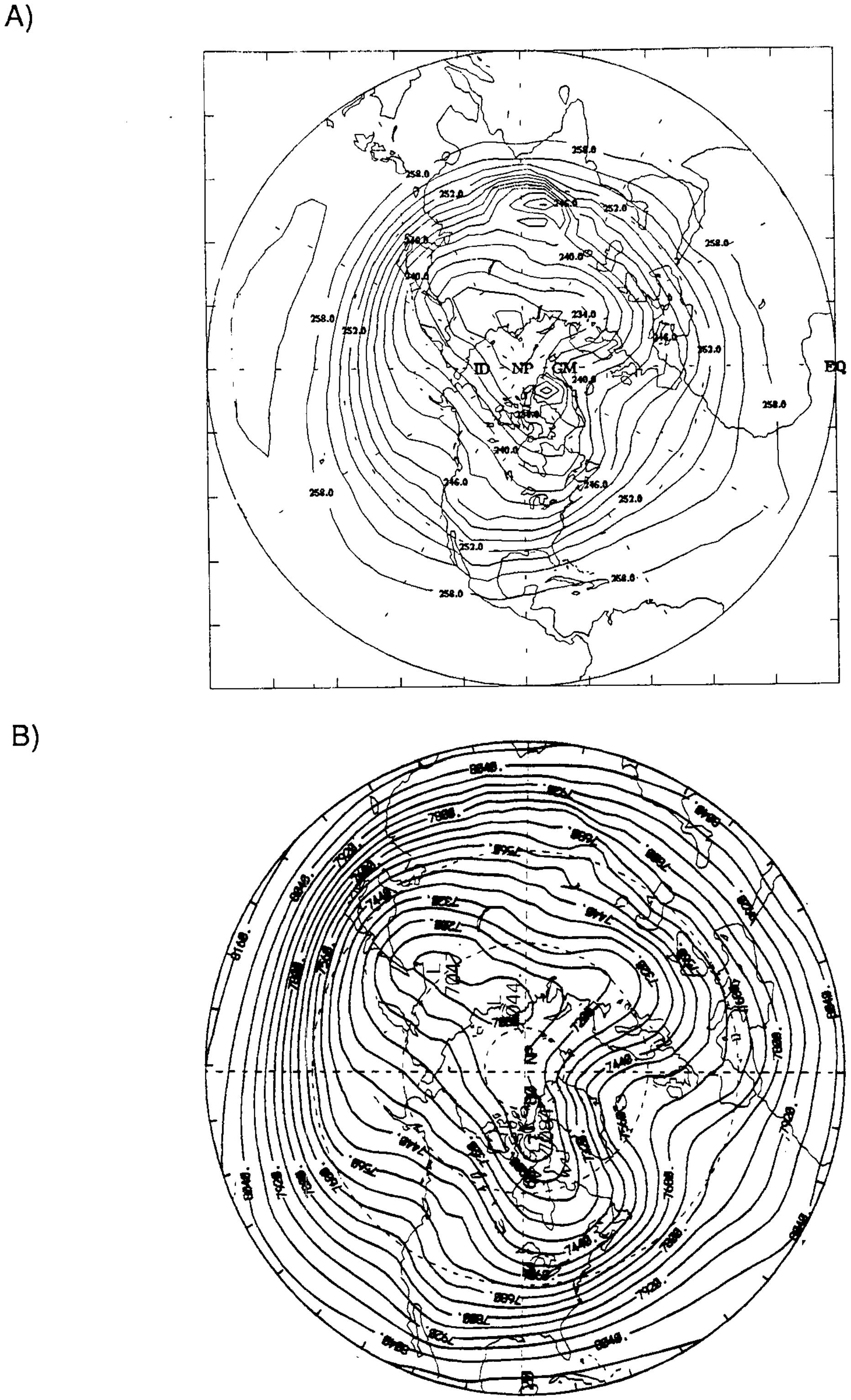

Figure 4.14: Comparison between MSU Channel 2 and ECMWF Thickness.
A) MSU Channel 2, 8-31 Jan 87, Contour Interval 2 K.
B) ECMWF 850-300 Geopotential Thickness Field, 8-31 Jan 87,

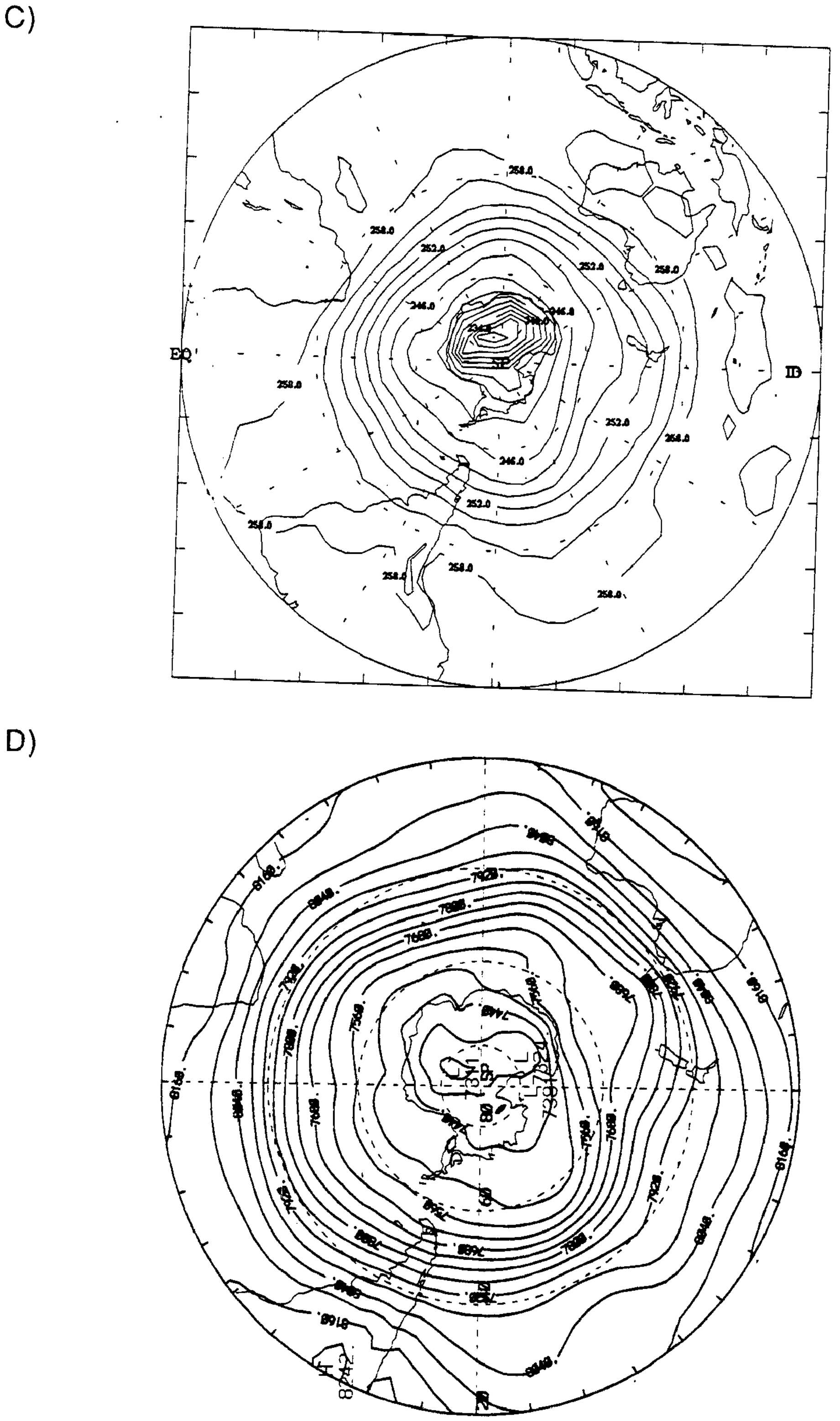

Figure 4.14: Comparison between MSU Channel 2 and ECMWF Thickness.
C) Same as Fig. 4.14a except SH.
D) Same as Fig. 4.14b except NH.

TABLE 4.4

MSU Channel 2 Meridional Temperature Gradient
vs.
850 - 300 ECMWF Geopotential Thickness Gradient

LONGITUDE LATITUDE	$-\frac{\delta T_{msu}}{\delta y}$ ($^oK\,km^{-1}$)	$-\frac{\delta \Phi}{\delta y}$ from ECMWF ($ms^{-2}m/km^{-1}$)	$-\frac{\delta T}{\delta y}$ calculated from ECMWF ($^oK\,km^{-1}$)
160E 20-60N	5.13×10^{-3}	2.16	7.23×10^{-3}
160E 20-60S	2.68×10^{-3}	1.28	4.29×10^{-3}
150W 20-40N	4.32×10^{-3}	1.89	6.33×10^{-3}
150W 40-60S	3.60×10^{-3}	1.66	5.58×10^{-3}
75W 20-60N	4.73×10^{-3}	2.00	6.71×10^{-3}
30W 20-60N	2.59×10^{-3}	1.04	3.47×10^{-3}
30W 40-60S	3.02×10^{-3}	1.44	4.82×10^{-3}
30E 20-60N	5.02×10^{-3}	1.87	6.25×10^{-3}
130E 20-60N	6.22×10^{-3}	2.45	8.21×10^{-3}

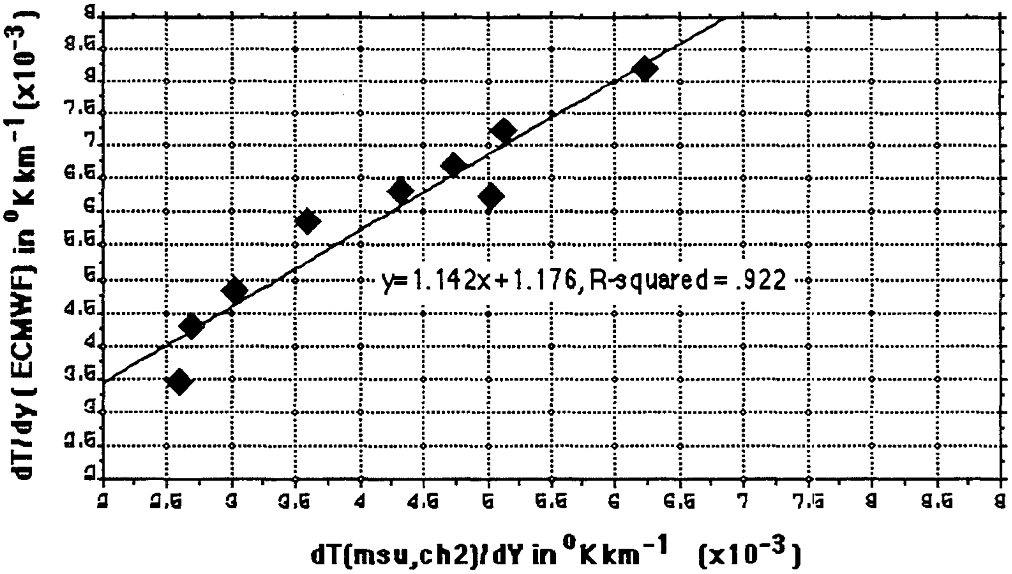

Figure 4.15: Comparison between MSU and calculated Temperature Gradients, CH2 vs. 850-300 ECMWF Thickness.

gradient, column 3 shows the ECMWF meridional geopotential thickness gradient and column 4 shows a calculated meridional temperature gradient using column 3 and Equation 4.9. The MSU thermal gradient is consistantly lower than the calculated gradient but within several ^{o}K per 1000 km. Figure 4.15 is a scattergram of the observation in Table 4.4. The black diamonds show the values of MSU meridional temperature gradient along the abscissa, and meridional temperature gradient calculated from 850-300 ECMWF geopotential thickness along the ordinate (in ^{o}K per 1000 km). Figure 4.15 also shows the resulting linear equation from a simple regression performed on the observations in Table 4.4.

Figures 4.16a and b are the same as Figures 4.14a and b except they show the results of the 1-18 Feb data set. Again regions of strong/weak thermal gradient patterns correspond to regions of strong/weak thickness gradient patterns.

Just as MSU Channel 2 corresponds to 850-300 mb thickness, MSU Channel 4 through its weighting function is representative of 200-100 mb thickness gradient. Figures 4.17a thru d allow a comparison between MSU Channel 4 thermal patterns and ECMWF geopotential thickness patterns for the 8-31 Jan data set. Again, the pattern similarity is remarkable, with a crescent-shaped high over the North Pacific and Canada and a bulls-eye low over Norway. Figures 4.18a thru d show the same comparison using the 1-18 Feb data set.

A similar relation exists between mean-layer temperature and geopotential height. This relationship is shown by intergrating both sides of the hydrostatic equation, Equation 4.3, from P_o to P_1, yielding the following equation

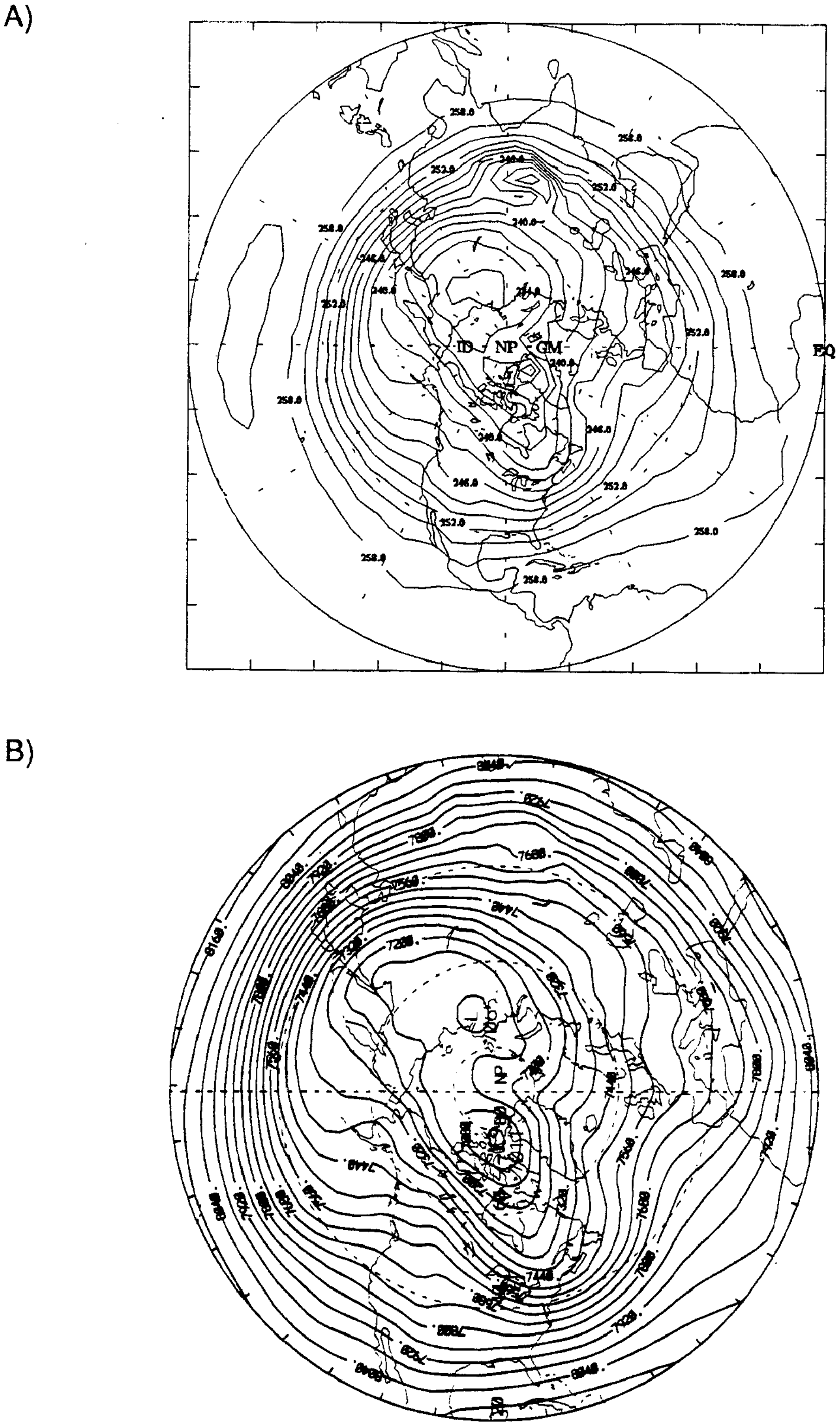

Figure 4.16: Comparison between MSU Channel 2 and ECMWF Thickness.
A) MSU Channel 2, 1-18 Feb 87, Contour Interval 2 K.
B) ECMWF 850-300 Geopotential Thickness Field, 1-18 Feb 87, NH, Contour Interval 60m.

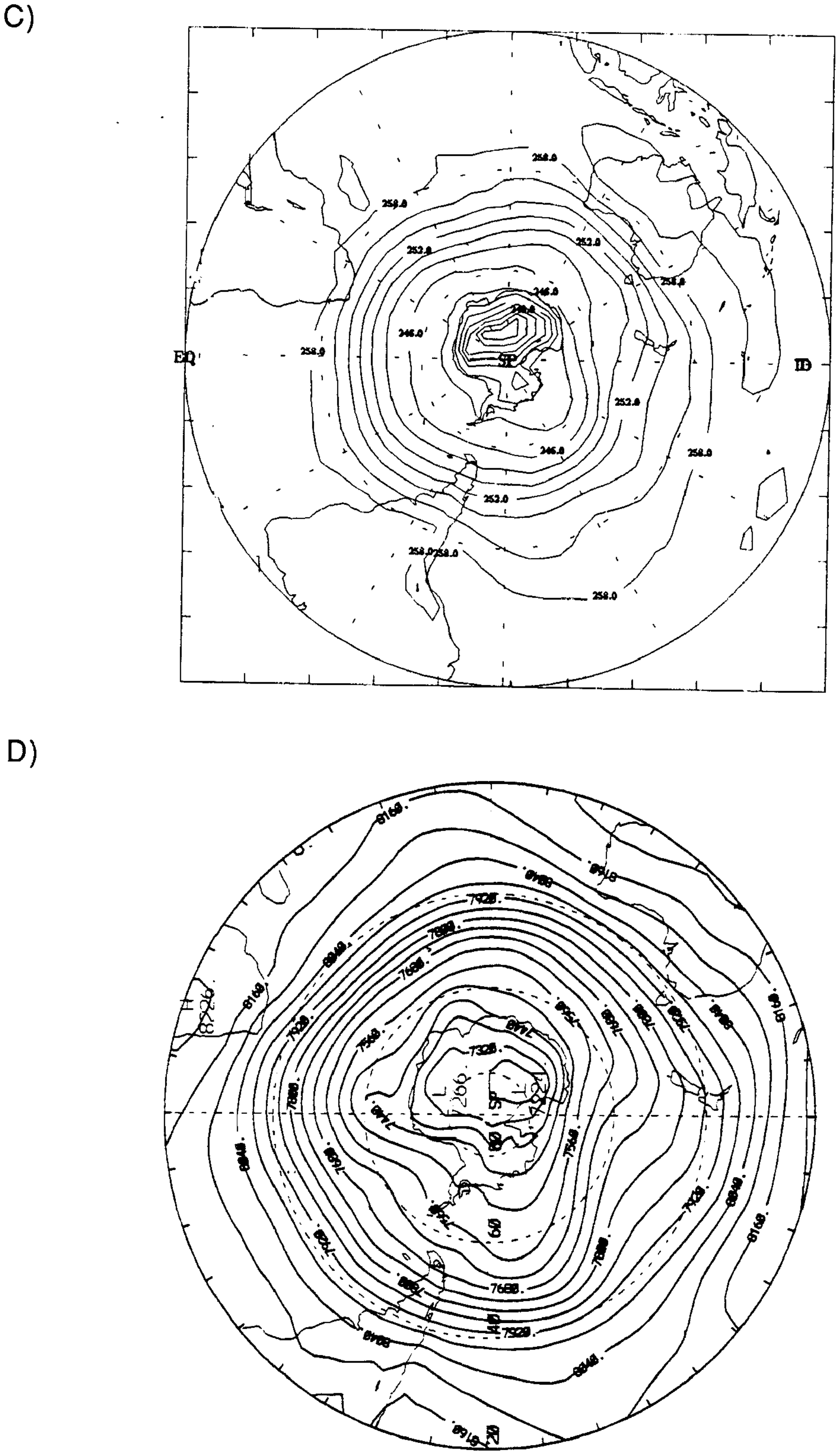

Figure 4.16: Comparison between MSU Channel 2 and ECMWF Thickness.
C) Same as Fig. 4.16a except SH.
D) Same as Fig. 4.16b except NH.

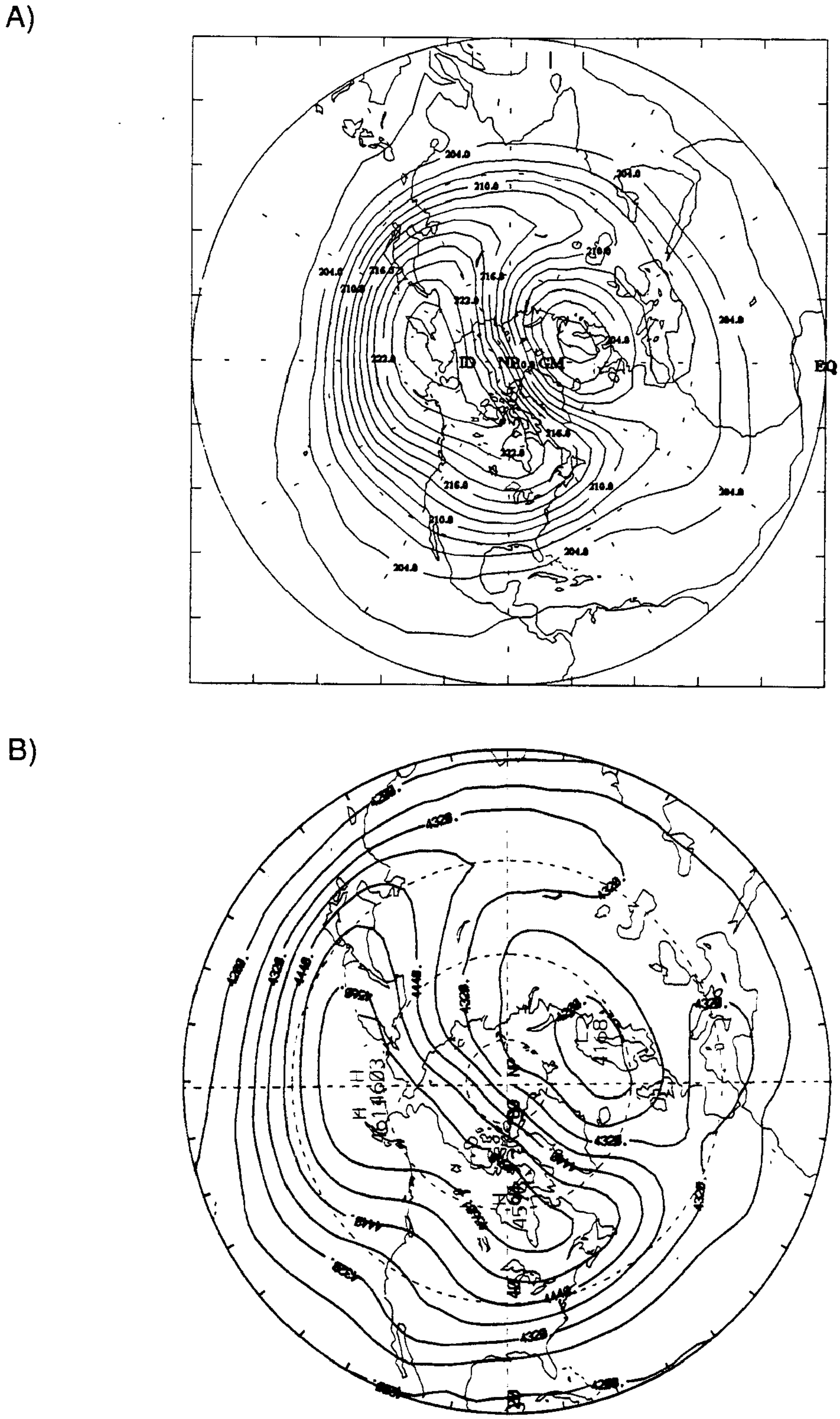

Figure 4.17: Comparison between MSU Channel 4 and ECMWF Thickness.
A) MSU Channel 4, 8-31 Jan 87, Contour Interval 2 K.
B) ECMWF 200-100 Geopotential Thickness Field, 8-31 Jan 87, NH, Contour Interval 60m.

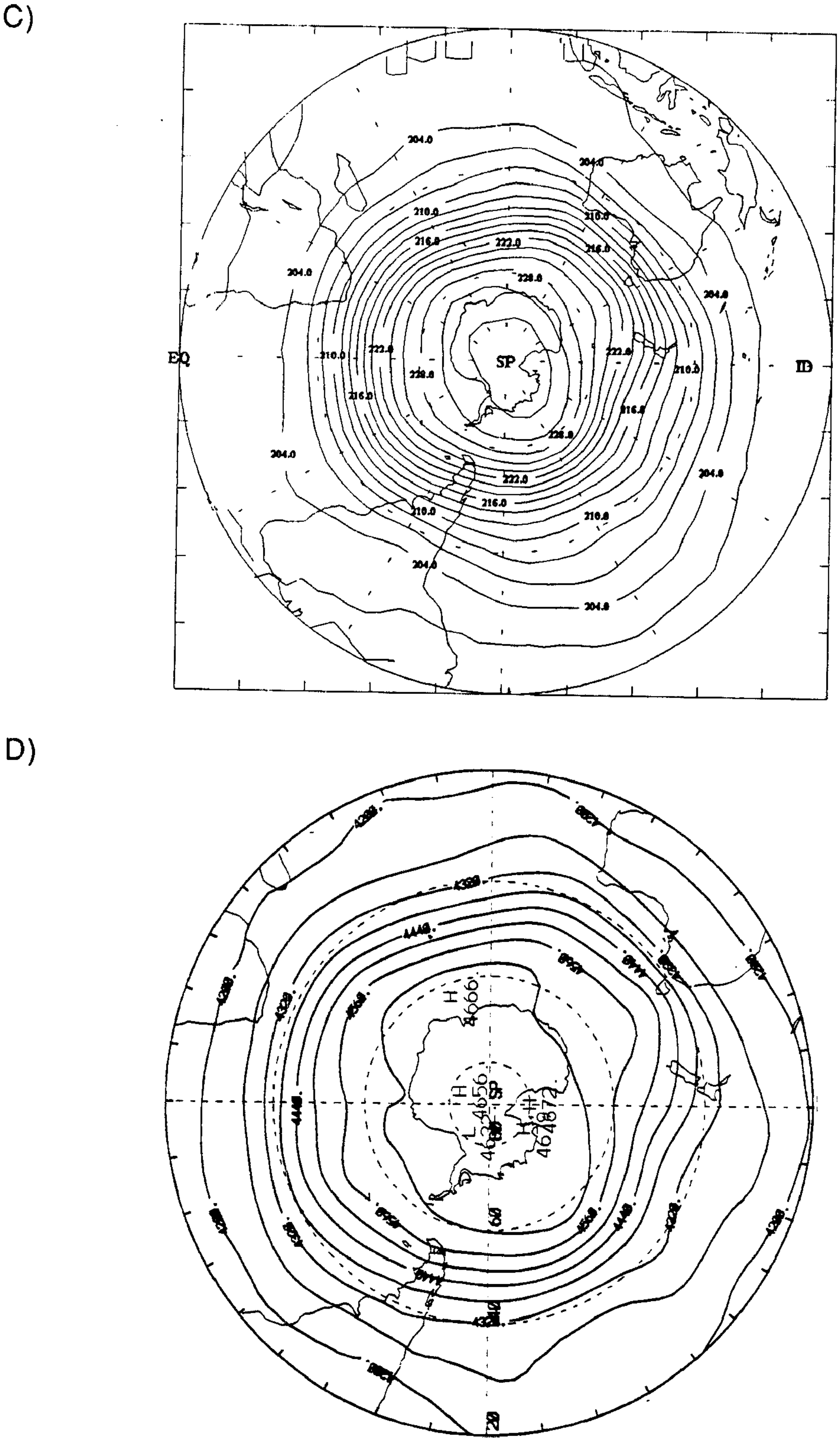

Figure 4.17: Comparison between MSU Channel 4 and ECMWF Thickness.
C) Same as Fig. 4.17a except SH.
D) Same as Fig. 4.17b except NH.

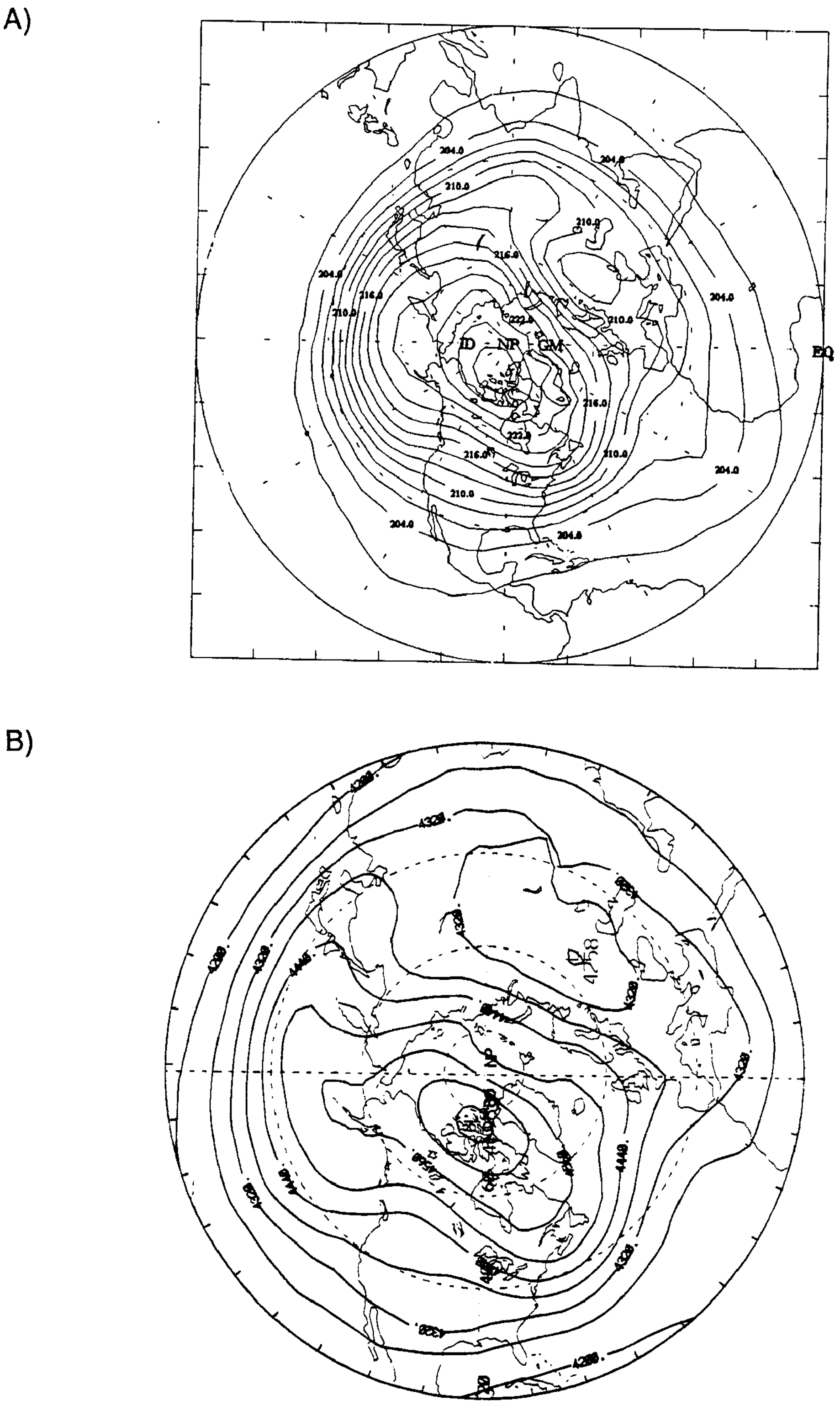

Figure 4.18: Comparison between MSU Channel 4 and ECMWF Thickness.
A) MSU Channel 4, 1-18 Feb 87, Contour Interval 2 K.
B) ECMWF 200-100 Geopotential Thickness Field, 1-18 Feb 87, NH, Contour Interval 60m.

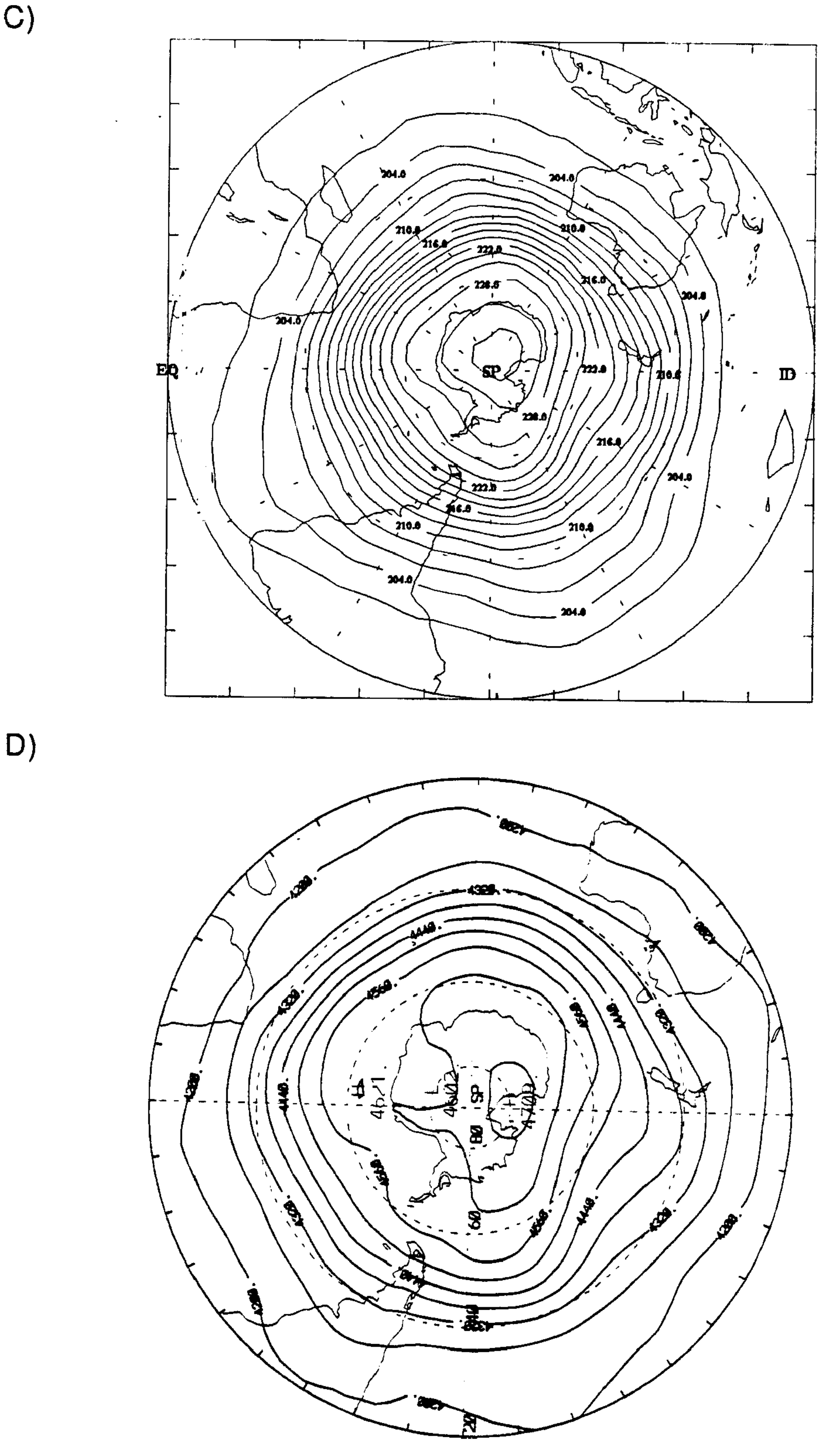

Figure 4.18: Comparison between MSU Channel 4 and ECMWF Thickness.
C) Same as Fig. 4.18a except SH.
D) Same as Fig. 4.18b except NH.

$$\delta\Phi = R_d \ln\left(\frac{P_0}{P_1}\right) T_{msu} \tag{4.10}$$

which shows isolines of thickness proportional to isotherms of mean-layer temperature.

An observational comparison between mean-layer temperature and geopotential thickness can be made using the same figures as in the previous section. Again since MSU Channel 2 can be considered an estimate of 850-300 mb mean-layer temperature, through Equation 4.10 it can be used to estimate the 850-300 mb geopotential thickness field. The calculated thickness field can then be compared with the ECMWF 850-300 mb geopotential thickness field. Table 4.5 presents 15 random calculations which compare observed MSU Channel 2 brightness temperature, Figure 4.14a, to the temperature calculated from Equation 4.10 using 850-300 mb geopotential thickness values from Figure 4.14b. Column 1 shows the latitude/longitude that applies to the calculation, column 2 shows the observed MSU brightness temperature of that point, column 3 shows the observed ECMWF geopotential thickness and column 4 shows the calculated temperature using column 3 and Equation 4.10. From Table 4.5 it is evident that MSU Channel 2 temperature is consistantly lower than the temperature calculated from thermal wind theory, Equation 4.10 due to the shape of the weighting function of Channel 2. Figure 4.19 shows a scattergram of the observations in Table 4.5. The black diamonds represent MSU Channel 2 temperature along the abscissa and temperature calculated from ECMWF 850-300 geopotential thickness along the ordinate (column 4). This comparison shows that MSU Channel 2 seems to be a good indication of 850-300 mb geopotential thickness using the simple regression equation displayed in Figure 4.19. From Equation 4.10, the

TABLE 4.5

MSU Channel 2 Temperature and ECMWF 850-300 Geopotential Thickness

LATITUDE LONGITUDE	$T_{MSU,CH2}$ (°K)	$\partial\Phi$ from ECMWF ($ms^{-1}m$)	$T_{calculated\ from\ ECMWF}$ (°K)
60N 160E	236.6	72000	240.9
40N 160E	243.9	74900	250.6
60S 160E	247.9	75900	253.9
60N 150W	242.7	74100	247.9
40N 150W	247.2	76400	255.6
60S 150W	245.5	75600	252.9
60N 75W	237.1	72300	241.9
40N 75W	246.2	76200	254.9
40S 75W	254.0	79500	265.9
60N 30W	243.9	75700	253.3
40N 30W	249.8	78000	261.0
40S 30W	252.2	78700	263.3
60N 30E	234.7	72600	242.9
40N 30E	244.8	76300	255.3
40S 30E	252.6	78900	264.0

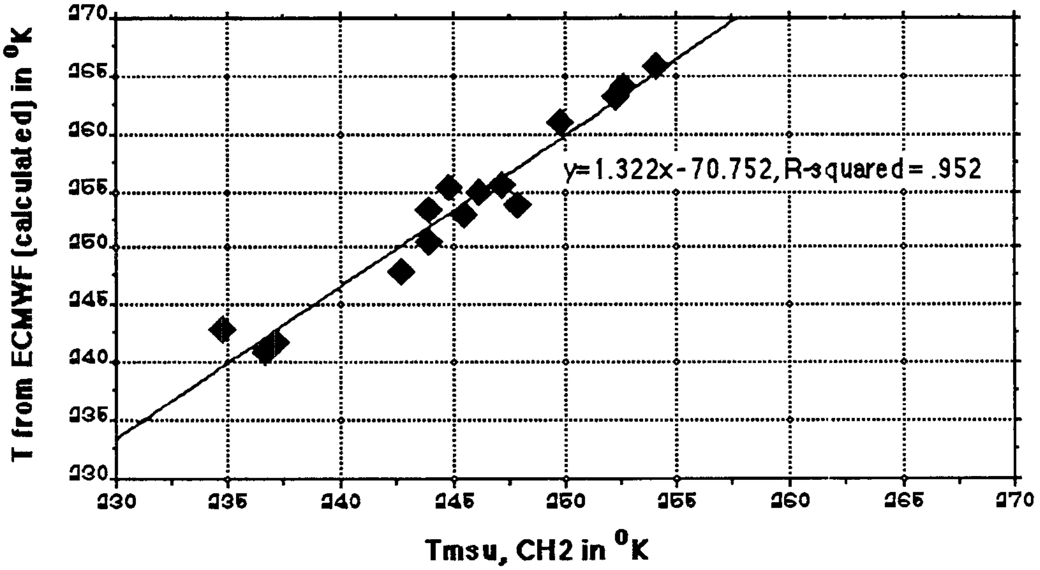

Figure 4.19: Comparison between MSU and calculated Temperature

TABLE 4.6

MSU Channel 4 Temperature and ECMWF 200-100 Geopotential Thickness

LATITUDE LONGITUDE	$T_{MSU, CH4}$ (°K)	$\partial\Phi$ from ECMWF ($ms^{-1}m$)	$\bar{T}$ calculated from ECMWF (°K)
60N 160E	227.2	45500	228.8
40N 160E	217.9	45000	226.2
40S 160E	215.3	43800	220.2
60N 150W	224.4	45700	229.3
40N 150W	215.5	44400	223.2
60S 150W	227.3	45900	230.8
60N 75W	222.1	45600	229.3
40N 75W	213.5	44400	223.2
40S 75W	212.9	43400	218.2
60N 30W	207.0	43400	218.2
40N 30W	208.4	43400	218.2
40S 30W	215.5	43800	220.2
60N 30E	200.2	42000	211.2
40N 30E	208.6	42800	215.2
40S 30E	215.5	43600	219.2

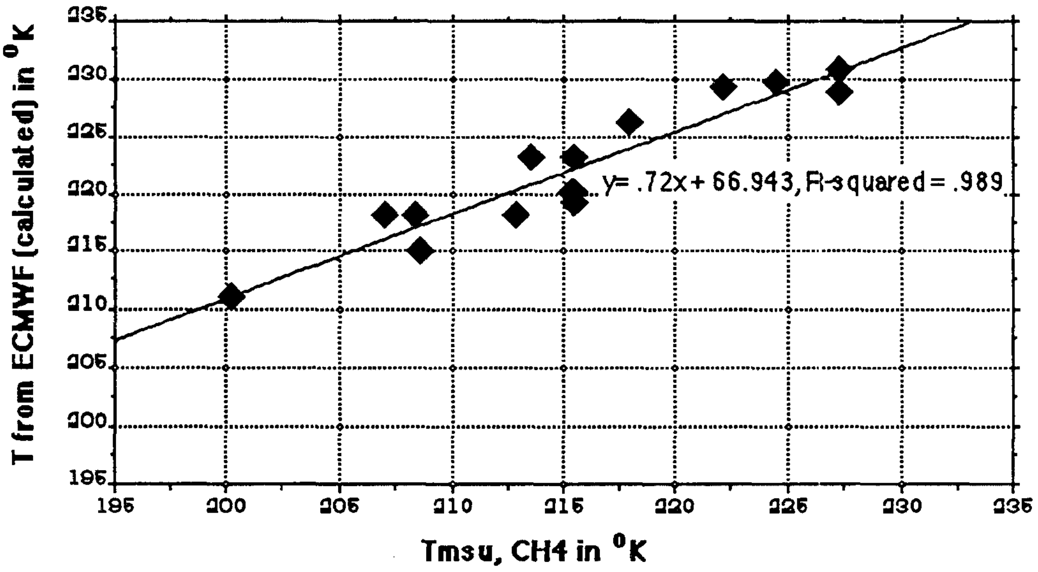

Figure 4.20: Comparison between MSU and calculated Temperature

850-300 geopotential thickness field can be predicted using MSU Channel 2 and the regression equation.

Table 4.6 presents a similar comparison calculation, instead MSU Channel 4 brightness temperature, Figure 4.17a, is compared to a calculated temperature using the 200-100 mb ECMWF geopotential thickness, Figure 4.17b. Results show MSU Channel 4 temperature consistantly lower than the calculated temperature. This is expected since the upper half of Channel 4's weighting function exists above 100 mb. The corresponding scattergram, Figure 4.20, shows MSU Channel 4 may be used to approximate the 200-100 mb geopotential thickness field using the regression formula.

4.6 MSU Thermal Fields and Streamfunction Fields

The horizontal velocity field may be partitioned into nondivergent and irrotational components (Lorenz,1963). The nondivergent part of the two dimensional velocity field can be expressed using the streamfunction in the following manner (Holton, 1979)

$$\tilde{V}_{\psi} = \hat{k} \times \tilde{\nabla}\Psi \qquad (4.11)$$

where its zonal wind component is given as

$$u_{\Psi} = -\frac{\partial(\Delta\Psi)}{\partial y} \qquad (4.12)$$

Isolines of the streamfunction thus correspond to streamlines of the nondivergent velocity field and the meridional gradient of streamfunction is proportional to the magnitude of the nondivergent velocity. Therefore plotting lines of constant streamfunction on a map gives a spatial distribution of the nondivergent velocity field. A scale analysis of the vorticity equation indicates that midlatitude synoptic scale motions are quasi-nondivergent, that is horizontal divergence must be small compared to the vorticity. Therefore, in the midlatitudes, the horizontal streamfunction field should be a good representation of the velocity field.

Streamfunction may be related to MSU thermal fields through thermal wind theory. In Equation 4.6, it was shown that the magnitude of zonal geostrophic wind at a pressure level P_1 is proportional to the meridional gradient of mean-layer temperature. In a similar fashion, Equation 4.12 shows the magnitude of zonal nondivergent wind proportional to the meridional gradient of streamfunction values. Mean-layer brightness temperatures fields should therefore correspond to streamfunction fields.

MSU Channel 2 may be considered representative of surface-to-300 mb mean-layer temperature, except in extensive regions of elevated terrain as previously discussed. The MSU Channel 2 brightness temperature field should correspond to the difference between streamfunction fields at 300 mb and the surface. Two assumptions should be kept in mind when evaluating this comparison. First, as is the case in Equation 4.6, $U_{g[p_{sfc}]}$ is assumed zero, and second MSU Channel 2 is assumed a true measure of 300 mb - surface mean-layer temperature. Figures 4.21a-d show the comparison between MSU Channel 2 brightness temperature and 1000-300 mb streamfunction difference from the 8-31 Jan ECMWF data. Figures 4.22a-d show the same comparison using 1-18 Feb MSU and ECMWF data sets. The pattern correlation for both data sets is again excellent. Figures 4.21a-b show a wave number 3 pattern with troughs located over the northeast Canada, northwest Europe, and eastern Asia. Figures 4.22a-b show a transition to a wave number 2 pattern as the ridge in the North Atlantic weakens. Troughs

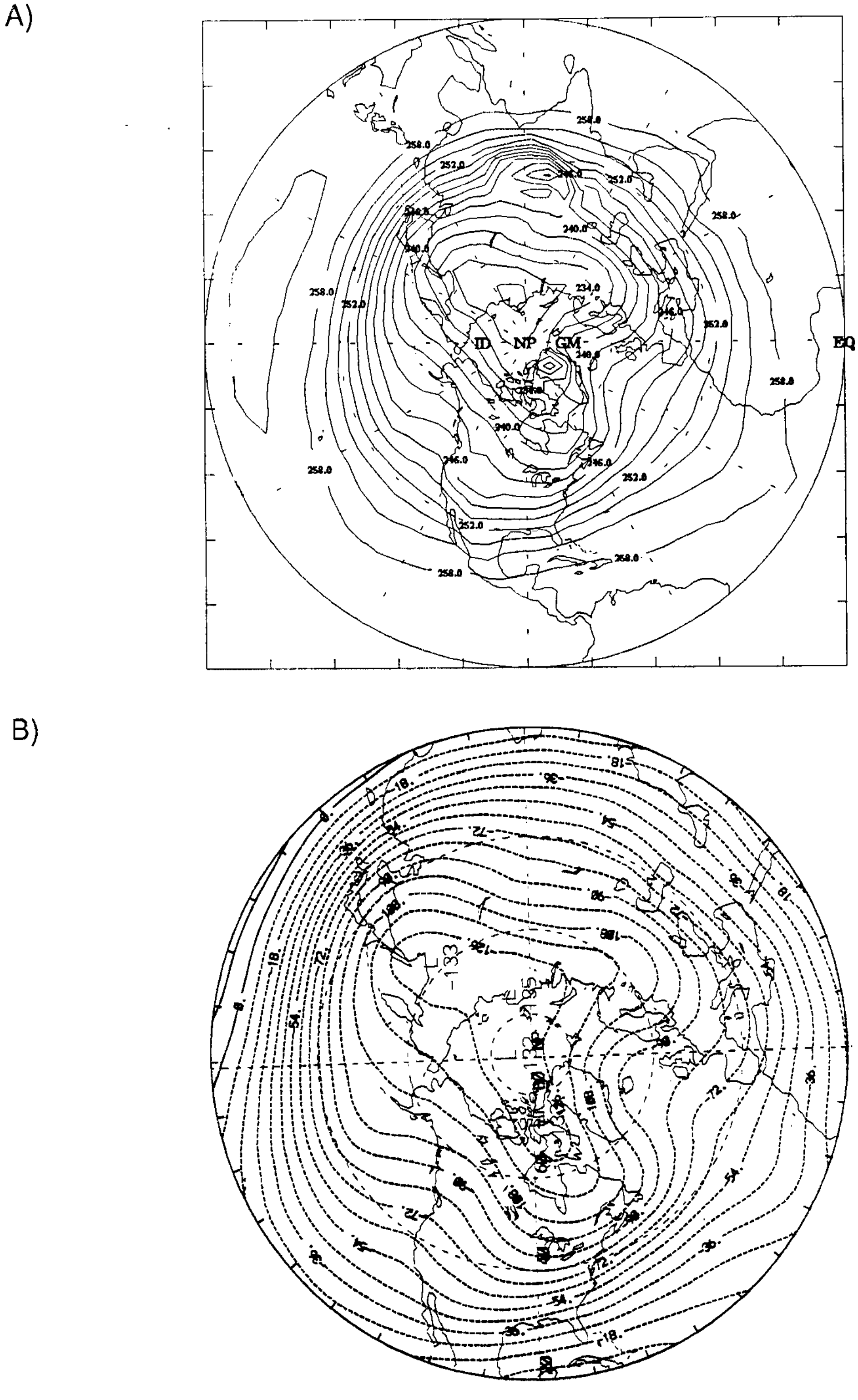

Figure 4.21: Comparison between MSU Channel 2 and ECMWF Streamfunction Thickness.

A) MSU Channel 2, 8-31 Jan 87, Contour Interval 2 K.

B) ECMWF 1000-300 Streamfunction Difference, 8-31 Jan 87, NH.

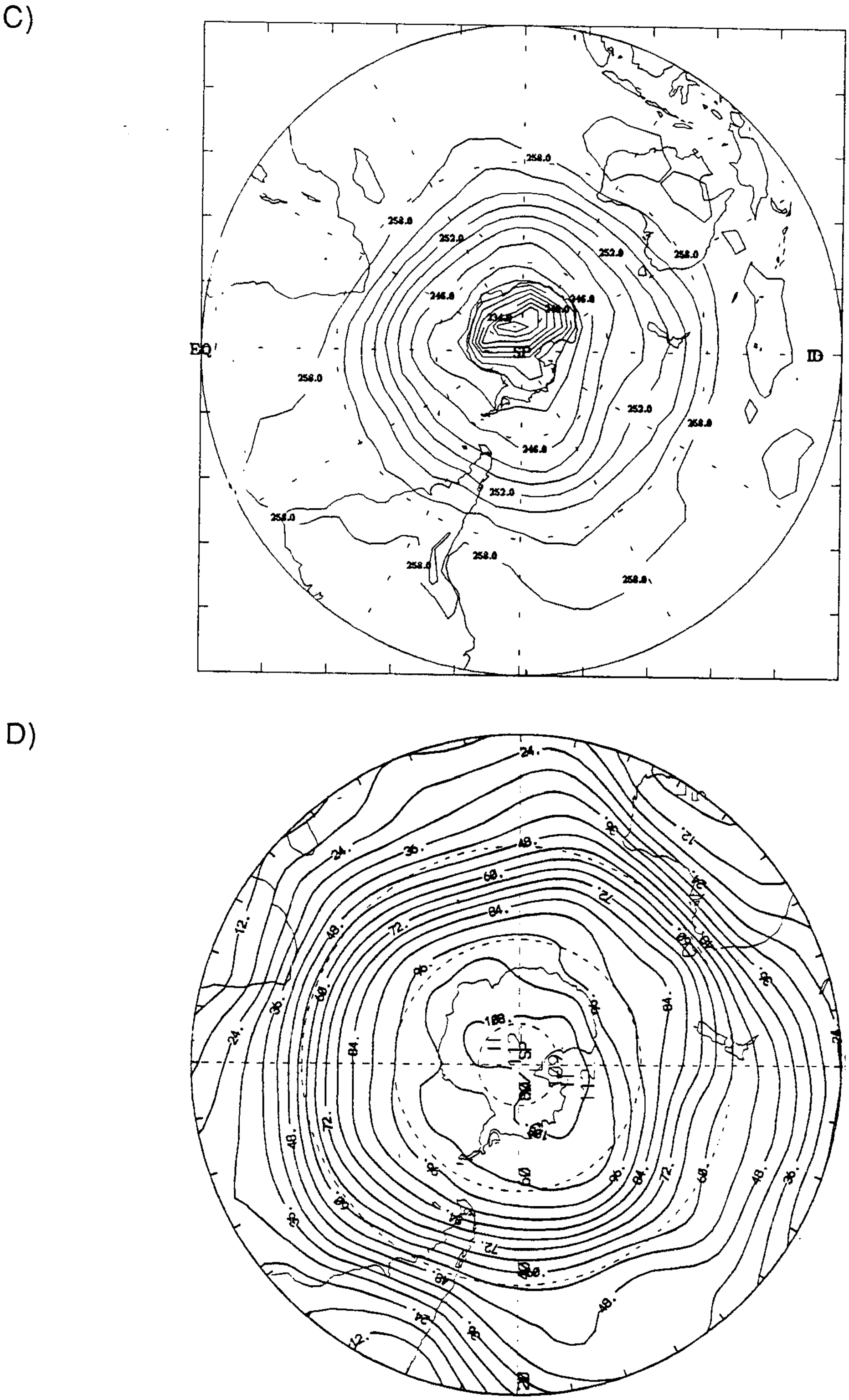

Figure 4.21: Comparison between MSU Channel 2 and ECMWF Streamfunction Thickness.
C) Same as Figure 4.21a except SH.
D) Same as Figure 4.21b except SH.

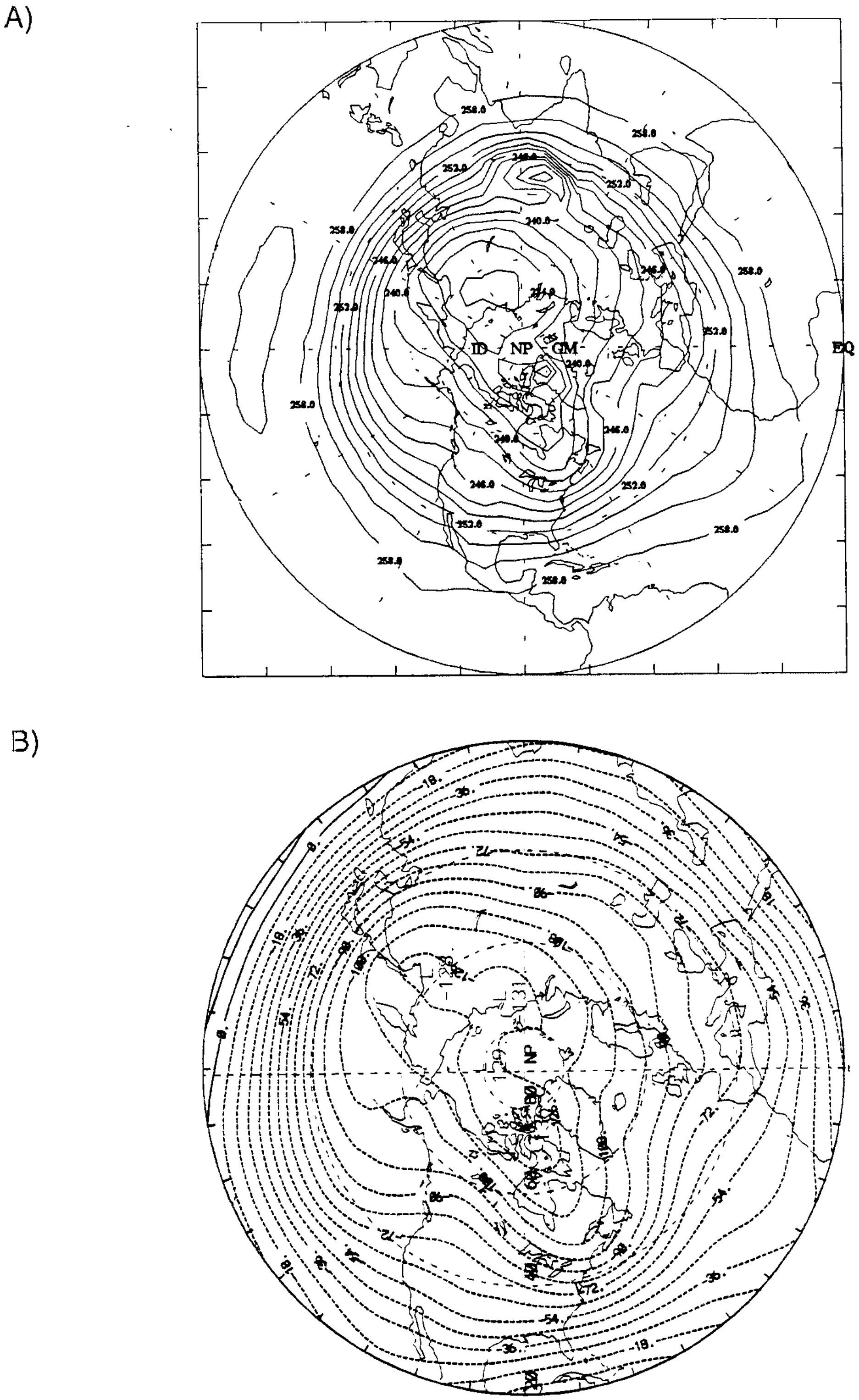

Figure 4.22: Comparison between MSU Channel 2 and ECMWF Streamfunction Thickness.

A) MSU Channel 2, 1-18 Feb 87, Contour Interval 2 K.

B) ECMWF 1000-300 Streamfunction Difference, 1-18 Feb 87, NH.

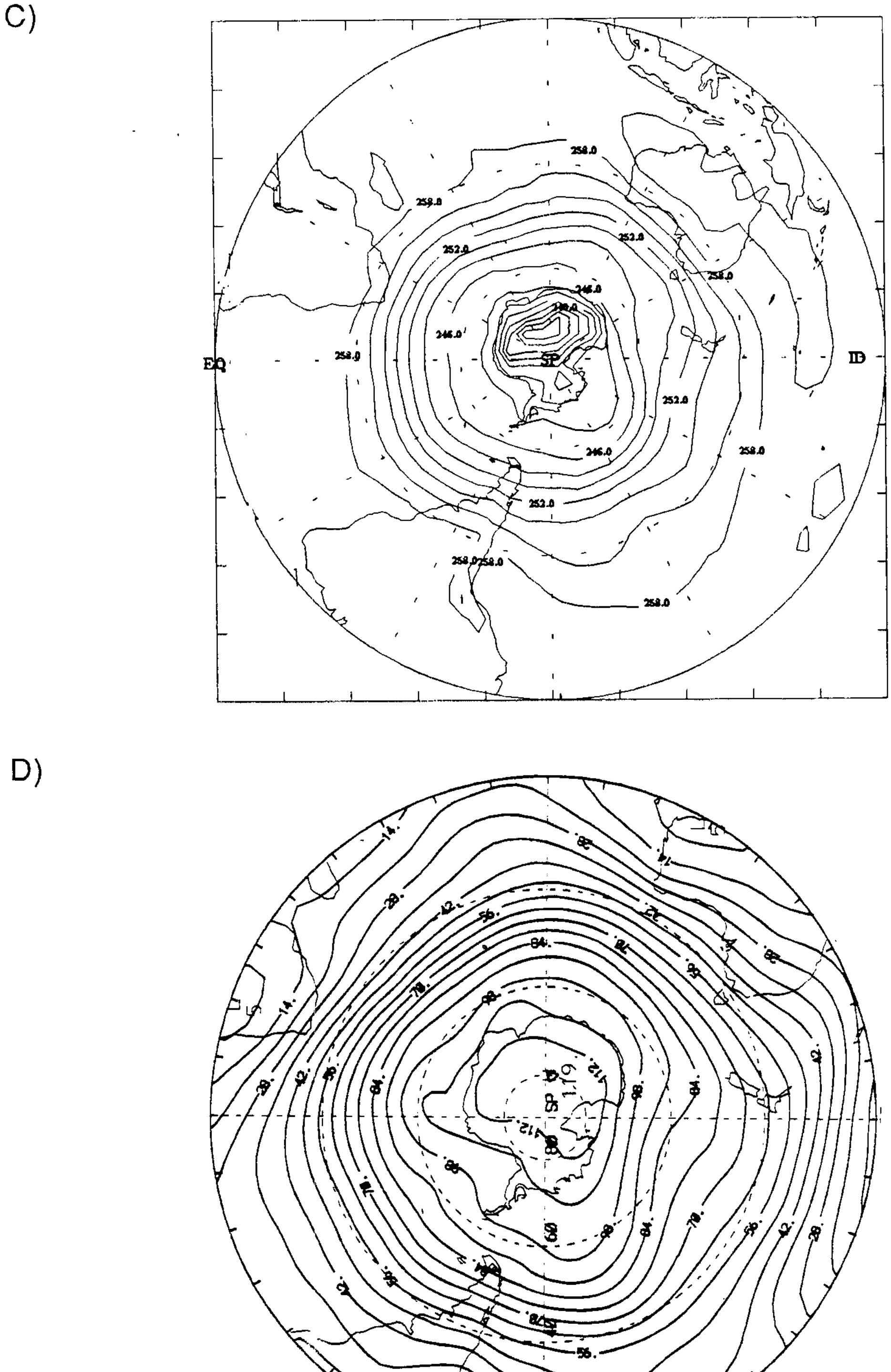

Figure 4.22: Comparison between MSU Channel 2 and ECMWF Streamfunction Thickness.
C) Same as Figure 4.22a except SH.
D) Same as Figure 4.22b except SH.

are located over northeast Canada and eastern Asia. From these figures it is evident Channel 2's thermal pattern correlates well with 1000-300 mb streamfunction difference.

4.7 UPPER-LEVEL WARMING OBSERVED BY MSU, ECMWF AND NMC DATA SETS

One of the most interesting features to appear from analysis of the Microwave Sounding Unit data set used in this study was a regional upper-level warming between the 8-31 Jan and 1-18 Feb data sets. The warming is observed between 50^{O}N latitude and the North Pole. Figures 4.23a-c show average brightness temperature as a function of latitude for MSU Channels 2, 3, and 4, respectively. An average brightness temperature value for each channel was computed for every 10^{O} latitude belt using the January and then the February data set. Latitude belt 1 represents the $90\text{-}80^{O}$S latitude belt, belt 2 represents $80\text{-}70^{O}$S, and so on to belt 18 which

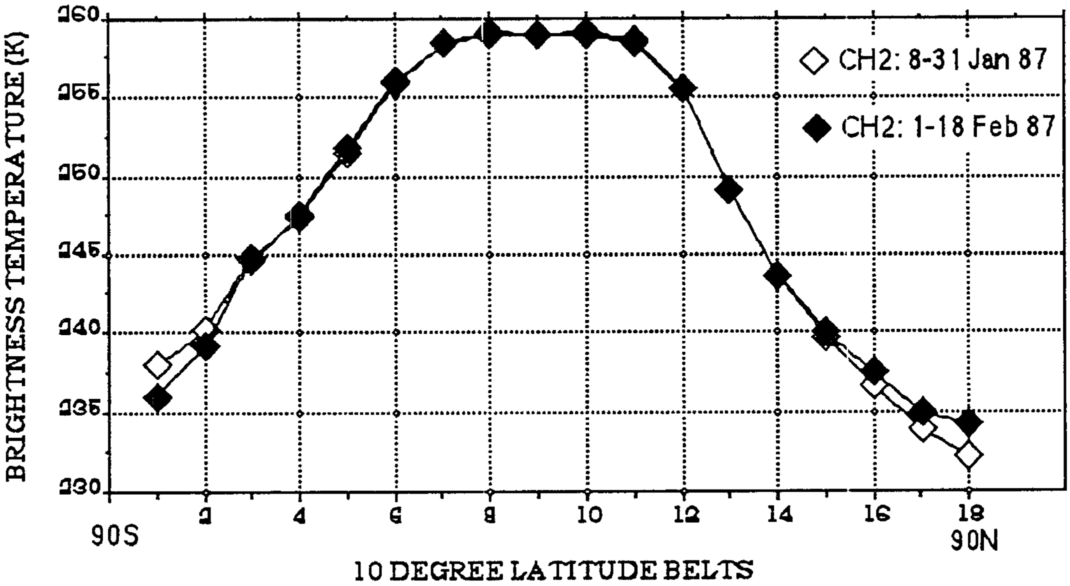

Figure 4.23a: 10^{O}-Latitude Belt Average Brightness Temperatures for MSU Channel 2: 53.74 GHz, for 8-31 Jan 87 (white diamonds), and 1-18 Feb 87 (black diamonds).

represents 80-90°N. In Figure 4.23a, Channel 2 shows little average brightness temperature difference between the January and February data sets, only a slight warming over the North Pole(≈1-2°K) and slight cooling

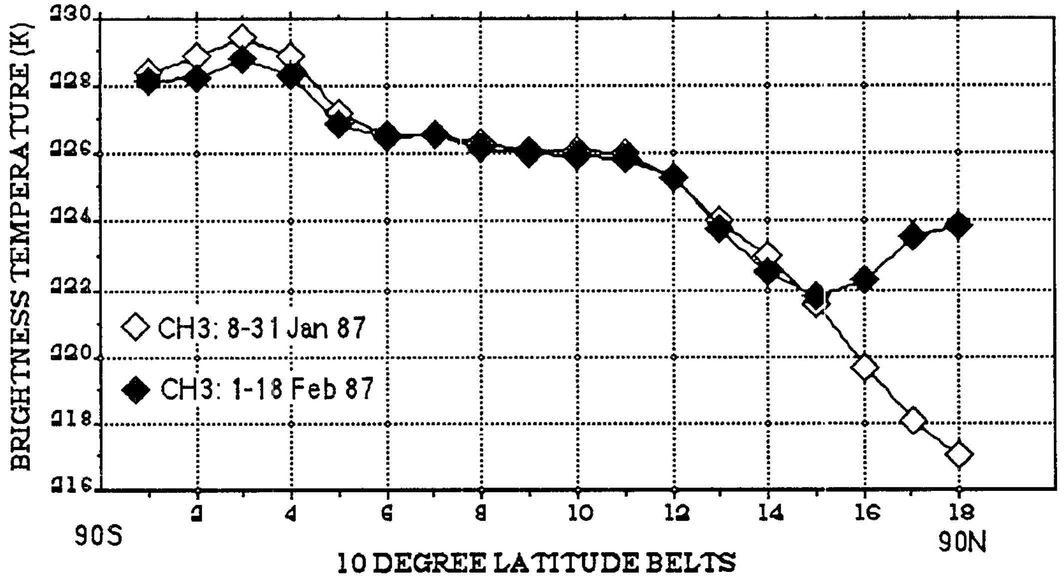

Figure 4.23b: 10°-Latitude Belt Average Brightness Temperatures for MSU Channel 3: 54.96 GHz, for 8-31 Jan 87 (white diamonds), and 1-18 Feb 87 (black diamonds).

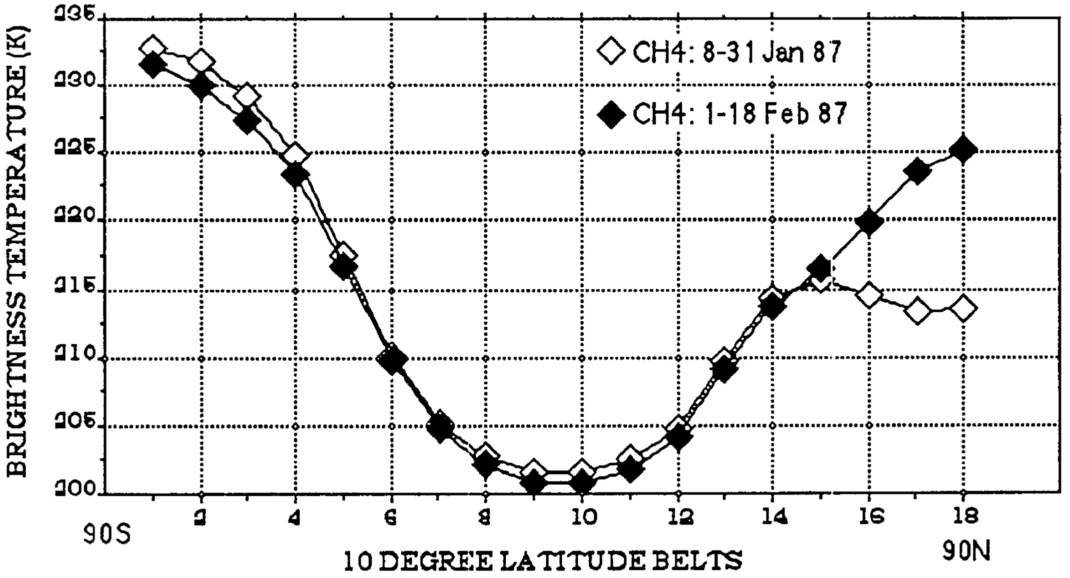

Figure 4.23c: 10°-Latitude Belt Average Brightness Temperatures for MSU Channel 4: 57.95 GHz, for 8-31 Jan 87 (white diamonds), and 1-18 Feb 87 (black diamonds).

over the South Pole(≈1-2°K). Channels 3 and 4, Figures 4.23b and c, show similar patterns of small differences between the two data sets from 90°S to 50°N, however from 50°N north to the pole they both show a considerable warming occured.
Average latitude belt brightness temperatures for Channel 3 increased from 2-7°K north of 50°N, while Channel 4's increased 2-12°K in this same region.

Review of the MSU brightness temperature fields in Chapter 2 show this observed warming to be regional. Global and northern hemispheric projections of the 8-31Jan and 1-18 Feb MSU Channel 3 and 4 data sets are shown in Figures 2.16 thru 2.19. Figure 2.16b shows a 214 K cold pool centered over the Barents Sea in the 8-31 Jan Channel 3 data set. Figure 2.17b, the 1-18 Feb MSU Channel 3 temperature field, shows brightness temperatures between 219 K and 222K over that same region indicating in a 5-8°K increase. Likewise, the Channel 4 projection for 8-31 Jan, Figure 2.18b, shows a 200 K cold pool centered over Norway while the1-18 Feb projection, Figure 2.19b, shows brightness temperatures in this region between 212 K and 216 K, a 10-16°K warming. In other regions north of 50°N no warming is observed. This is the case over Eastern Siberia and the North Pacific Ocean for Channels 3 and 4. Since portions of Channel 3's weighting function and most of Channel 4's exists in the lower stratosphere this warming phenomenon detected by the MSU may be the result of a sudden stratospheric warming (no such warming was evident from Channel 2).

To determine if this upper-level warming was detected by a data set other than MSU we may use ECMWF analyses up to 100mb. ECMWF meridional cross-section of temperature are shown in Figures 4.24 for this purpose. The strongest warming observed poleward of 50°N by MSU Channel 4 was

A)

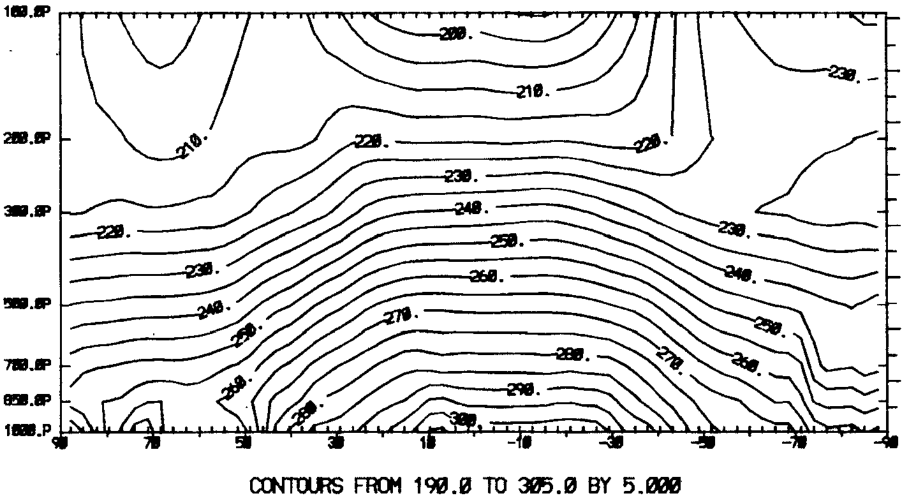

B)

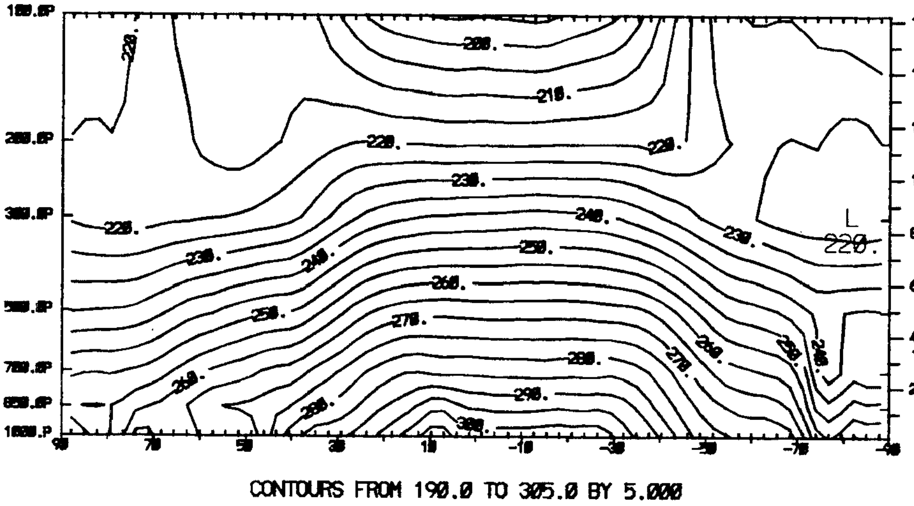

Figure 4.24: ECMWF Temperature Cross-sections along A) 30^{O} East for Jan 8-31, B) 30^{O} East for Feb 1-18, C) 75^{O} West for Jan 8-31, and D) 75^{O} West for Feb 1-18.

C)

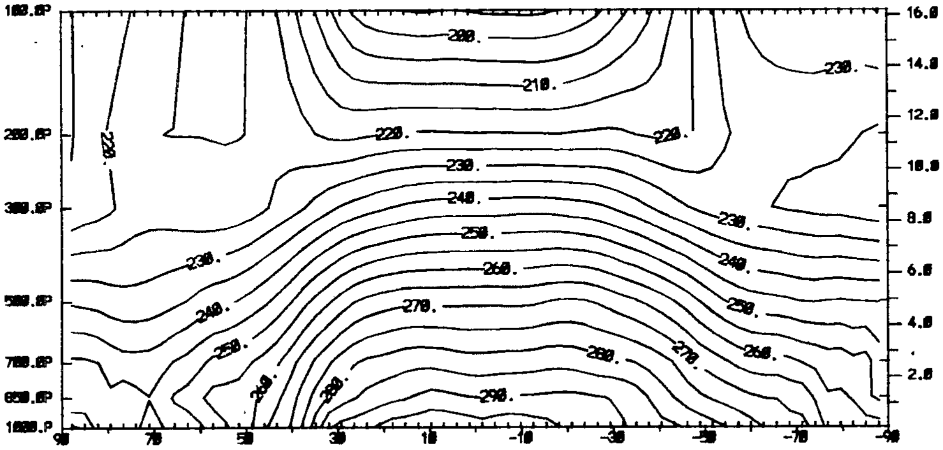

CONTOURS FROM 190.0 TO 295.0 BY 5.000

D)

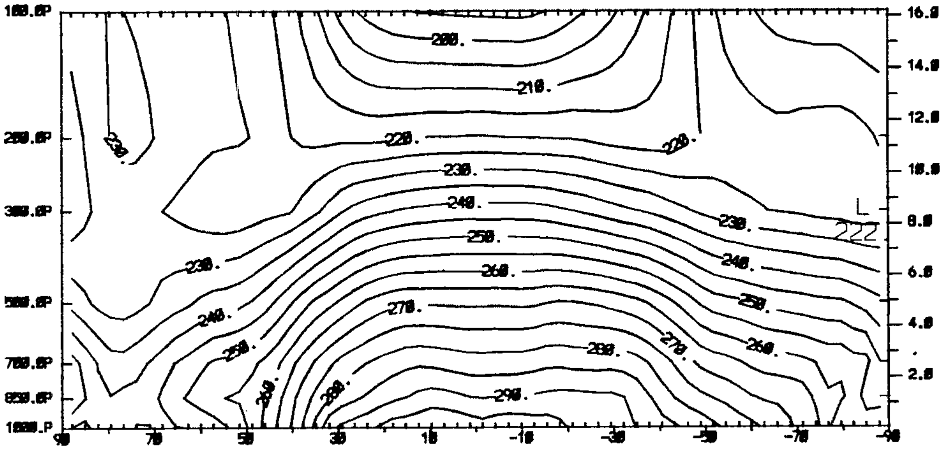

CONTOURS FROM 190.0 TO 295.0 BY 5.000

centered along 30^{O}E longitude. Figures 4.24a-d show ECMWF temperature cross-sections along 30^{O}E and 75^{O}W longitude for 8-31 Jan and 1-18 Feb. Comparing Figure 4.24a with b shows a warming of up to 15 K poleward of 50^{O}N between 200 and 100 mb from the January and February data sets along 30^{O}E. A slightly weaker warming is seen from comparing Figures 4.24c and d along 75^{O}W (up to 10 K) north of 50^{O}N. From these analyses it is evident that both the ECMWF and MSU data sets show indications of significant warming north of 50^{O}N. A comparison of global ECMWF 100 mb temperature fields for 8-31 Jan 87 and 1-18 Feb 87, Figures 3.3b and 3.4b, also indicate warming patterns similar to those seen in the MSU data set. The January data set shows the 203 K cold region over Norway warming to near 220 K in the February data set. The pattern similarity between MSU Channel 4 for 8-31 Jan and 1-18 Feb (Figures 2.18a and 2.19a), and ECMWF 100 mb temperature fields for that same period (Figures 3.3b and 3.4b) are self-evident.

To determine if this observed warming is actually the result of sudden stratospheric warming several of characteristics must be evaluated. First, the MSU and ECMWF brightness temperature fields show a warming only in the Northern Hemisphere. This agrees with the sudden stratospheric warming hypothesis, since warmings of sufficient amplitude to reverse the zonal wind have not been observed in the Southern Hemisphere (Levoy and Webster 1976). Sudden stratospheric warmings are theorized to be a result of vertical energy propagation from planetary scale waves in the troposphere below (Holton, 1979). Large-amplitude planetary waves appear to pump heat northward from the tropical troposphere into the polar regions (Mahlman, 1969). Vertical propagation can only occur, however, when zonal winds are westerly and weaker than a critical value defined as the Rossby critical velocity. Sudden stratospheric warmings do not occur during summer when stratospheric winds are easterly. Winter statospheric circulation over the north pole is dominated by a strong zonal polar vortex of westerly winds, driven by the positive meridional temperature gradient. During a warming event the cold polar vortex is observed to break down (Schoeberl, 1978) allowing the critical velocity needed for vertical energy propagation to occur to be reached. A rapid warming may then occur over the polar region, at times even to the point of reversing the meridional temperature gradient and creating a circumpolar easterly current in stratosphere.

Several time-series graphs of MSU brightness temperature are presented to narrow down when the warming occured. Figure 4.25 shows average MSU brightness temperature on a daily basis from 8 Jan thru 18 Feb. This figure shows the zonal average brightness temperature of 5^{o} latitude belts center on 80^{o}N and 50^{o}N computed daily for Channels 3 and 4. The 80^{o}-50^{o} brightness temperature difference is plotted as a line chart. This temperature difference criteria was chosen to allow a comparison with work done by Labitzke, 1977 in classifying a stratrospheric warming a major or minor warming. Figure 4.25 gives a view of near-polar warming with mid-latitude contributions subtracted out. Two seperate periods of warming are evident from this time series, 21-25 Jan and 3-6 Feb. As expected Channel 3 doesn't show as strong a warming as Channel 4 since its weighting function is mainly in the troposphere. Labitzke considered a major warming event one where the 80^{o}N-50^{o}N temperature difference becomes positive and approaches +10^{o}C. The 21-25 Jan warming meets this criteria, with the 3-6 Feb warming either a minor warming or an extension of the initial warming. Figure 4.26 shows the daily change in

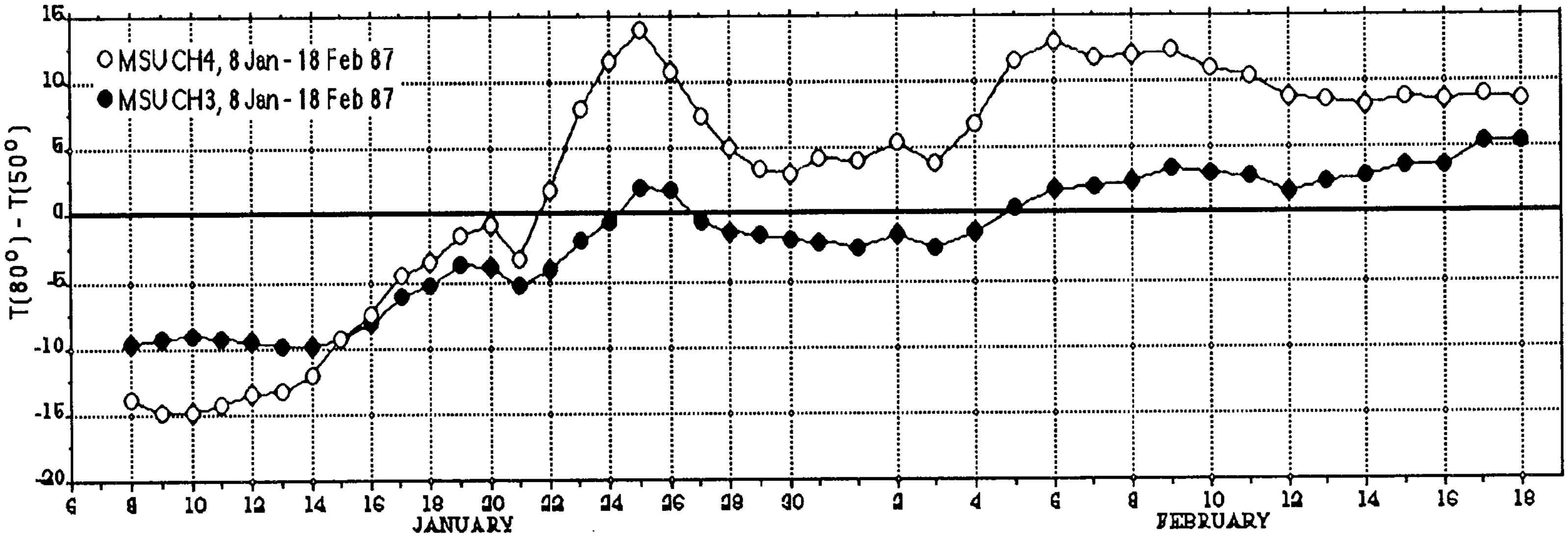

Figure 4.25: Daily Brightness Temperature Trend as Observed by MSU Channels 3 and 4, for 8 Jan - 18 Feb 87.

(Latitudinal Average at 80°N - Latitudinal Average at 50°N in °K)

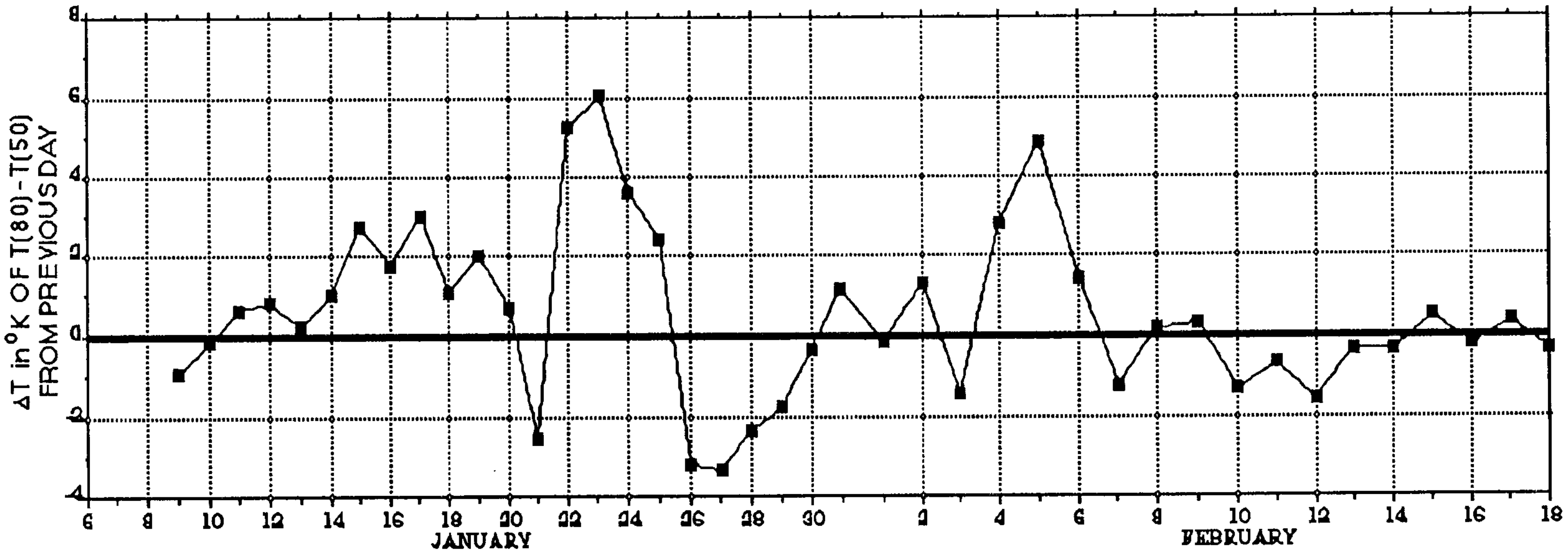

Figure 4.26: Daily Warming/Cooling Trend as Observed by MSU Channel 4, 8 Jan - 18 Feb 87.

(ΔT from Figure 4.25 minus ΔT of previous day)

80^{O}N-50^{O}N brightness temperature from the previous day on a line chart. For example, on Jan 22 the 80^{O}-50^{O} brightness temperature was 7 K higher than on 21 Jan. Days of warming are above the zero line, days of cooling below.

ECMWF data used in this study is only available up to the100 mb level. This limitation requires the upper-level warming observed by the MSU to be compared with another analysis data set above 100 mb. National Meteorological Center (NMC) daily analysis of temperature, and geopotential height at 50 mb is used in this research to study the observed warming higher in the stratosphere. Like the ECMWF data, NMC data is available on mass store files at NCAR. The northern hemispheric NMC anlaysis presented in this section were computed on the CRAY computers at NCAR.

Daily northern hemisphere projection of NMC 50 mb temperature and geopotnetial height were produced for the 8 Jan - 18 Feb 87 time period. Figure 4.26 is a time series of 80^{O}N - 50^{O}N temperature difference constructed to compare with the MSU data in Figure 4.25. From previous discussion it was shown the strongest warming was centered along 30^{O} East longitude. Figure 4.27 was constructed by subtracting the temperature at 50^{O}N from that at 80^{O}N along 30^{O} E from the NMC maps. A comparison of Figures 4.25 (Channel 4) and 4.27 reveals that MSU Channel 4 and NMC 50 mb data have similar temperature difference trends throughout the period. Both show pronounced warmings between 21 - 25 Jan and 3 - 6 Feb 87. Figure 4.28 shows 80^{O}N - 50^{O}N geopotential height difference along 30^{O} East longitude. This figure shows an average wind reversal (westerly to easterly) between 80^{O}N and 50^{O}N which appears to coincide with reversal of the meridional temperature gradient associated wiht the two warming events.

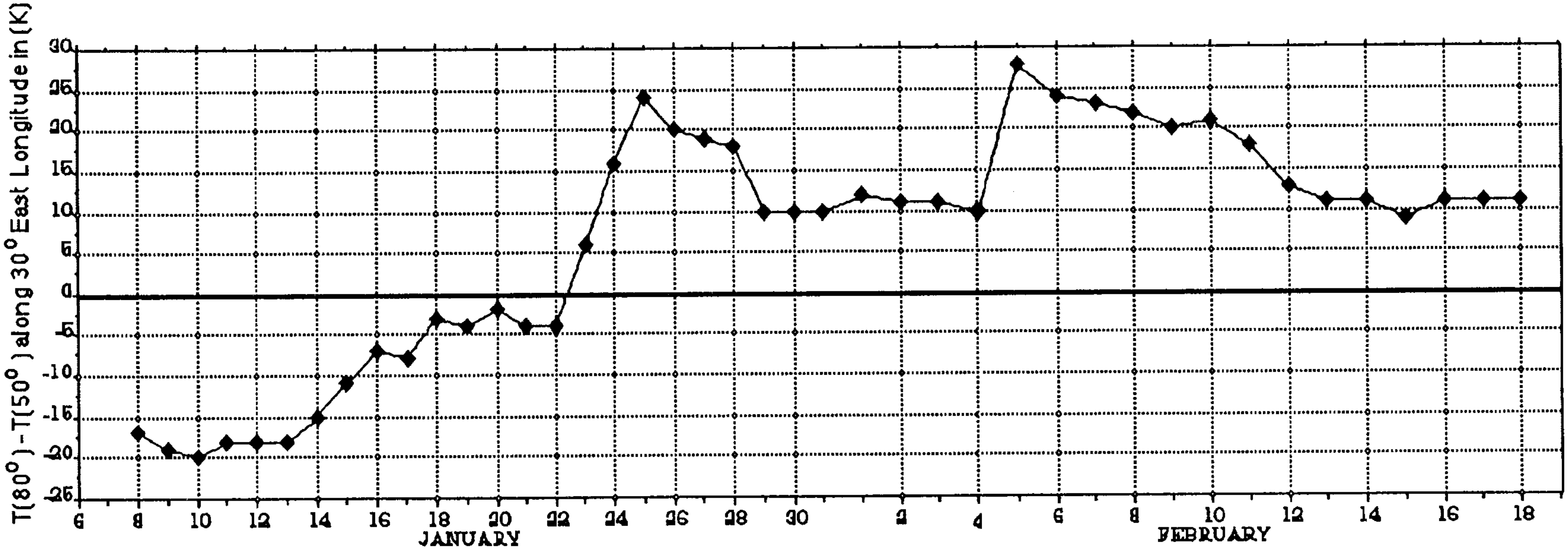

Figure 4.27: NMC 50 MB TEMPERATURE AT 80°N - 50°N ALONG 30° EAST LONGITUDE, 8 JAN - 18 FEB 87.

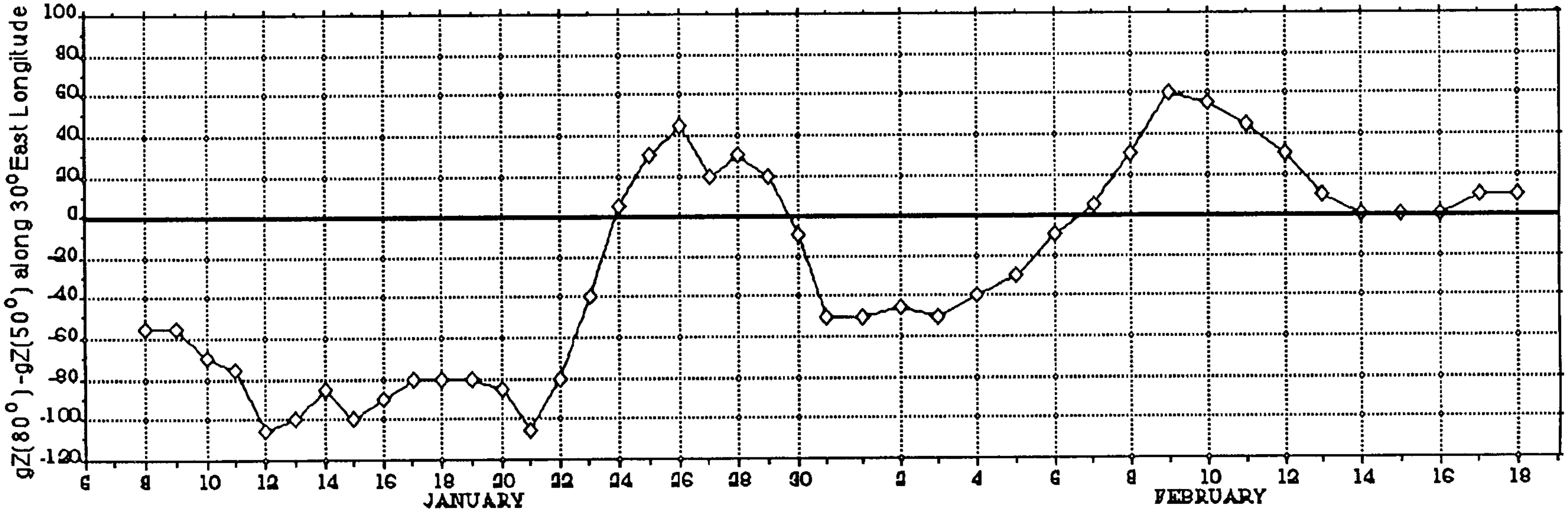

Figure 4.28: NMC 50 MB GEOPOTENTIAL HEIGHT AT 80°N - 50°N ALONG 30° EAST LONGITUDE, 8 JAN - 18 FEB 87. [Δ(gZ) is proportional to $-u_g$]

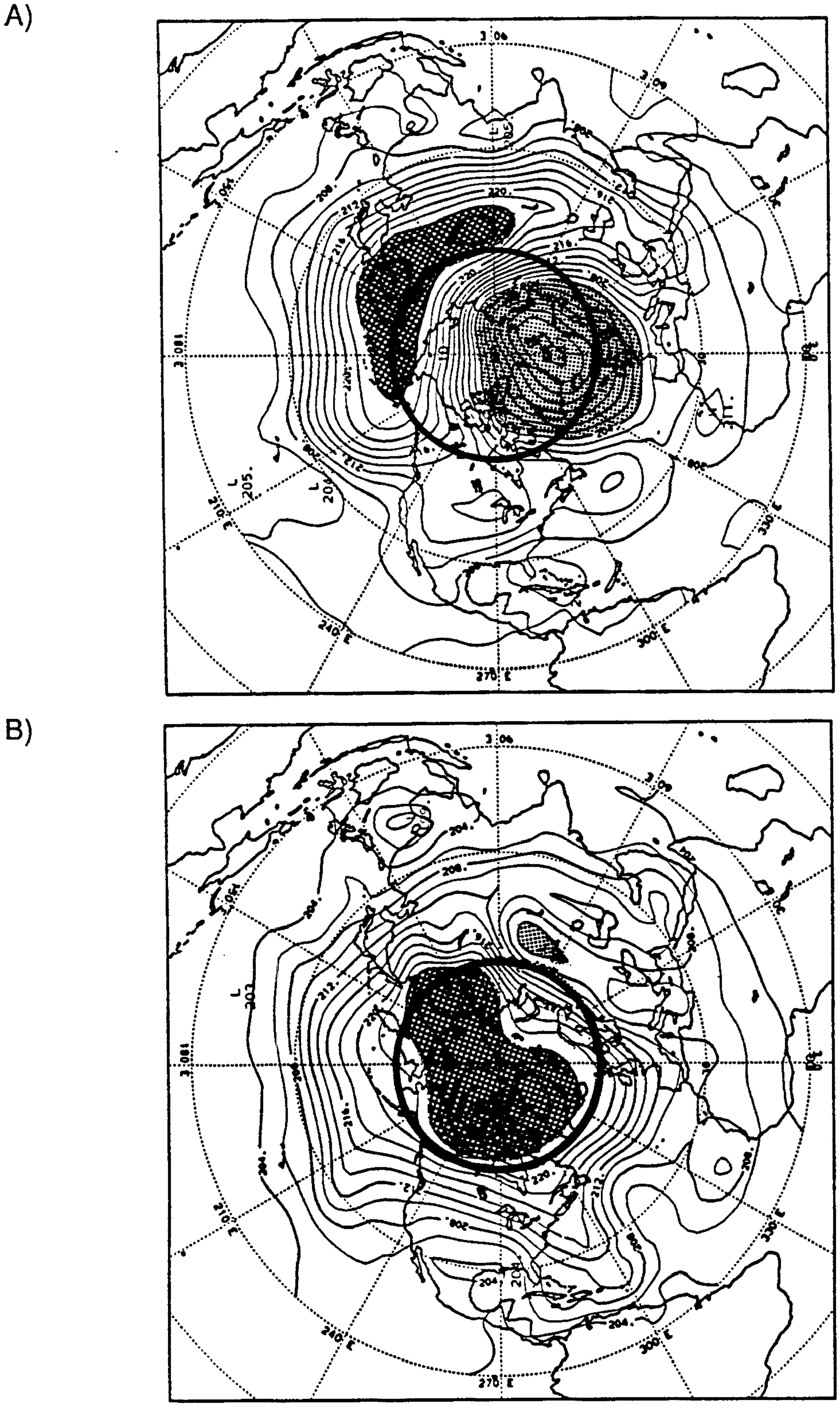

Figure 4.29: NMC 50 mb Temperature (K)Field for A) 12Z Jan 10 1987, and B)12Z Feb 10 1987 with regions colder than 204 K shaded and regions warmer than 224 K hatched; and NMC 50 mb Geopotential Height (GPM) Field for C) 12Z Jan 10 1987, and D) 12Z Feb 10 1987.

C)

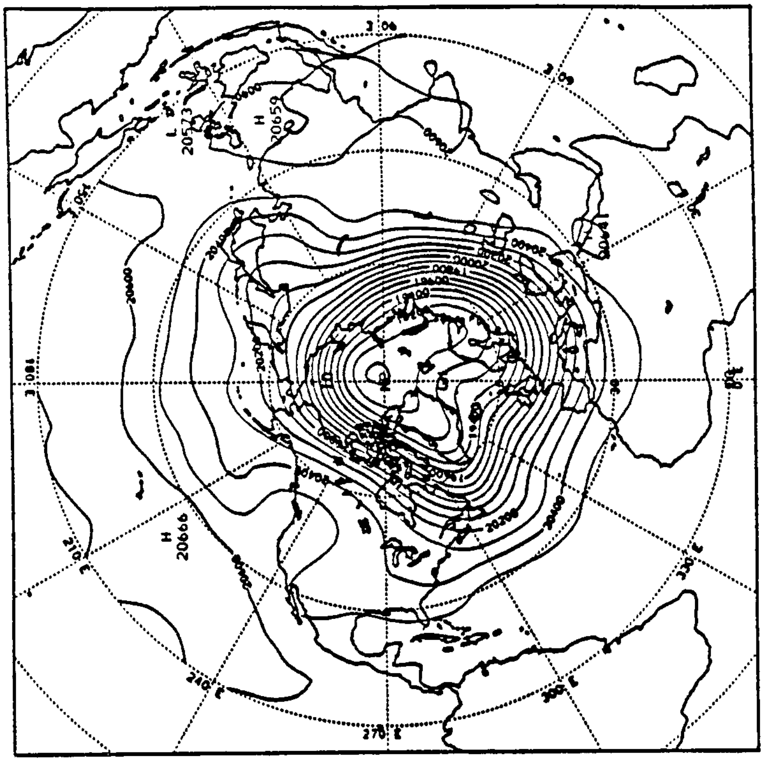
L
20523
H
20659
H
20666
20600
20200
240 E
270 E
300 E
210 E
330 E

D)

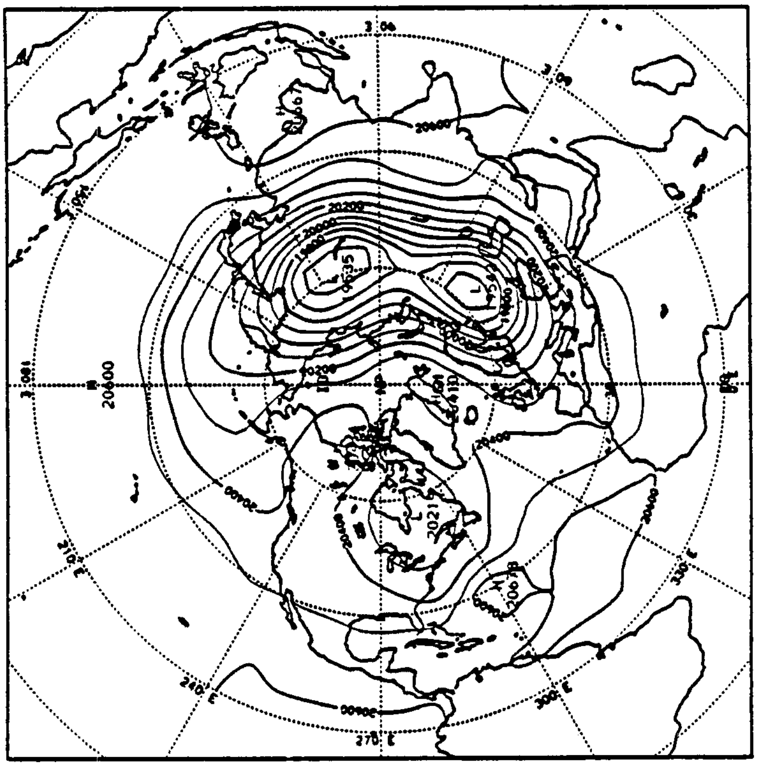
20600
20200
20000
H
20600
L
20213
240 E
270 E
300 E
210 E
330 E

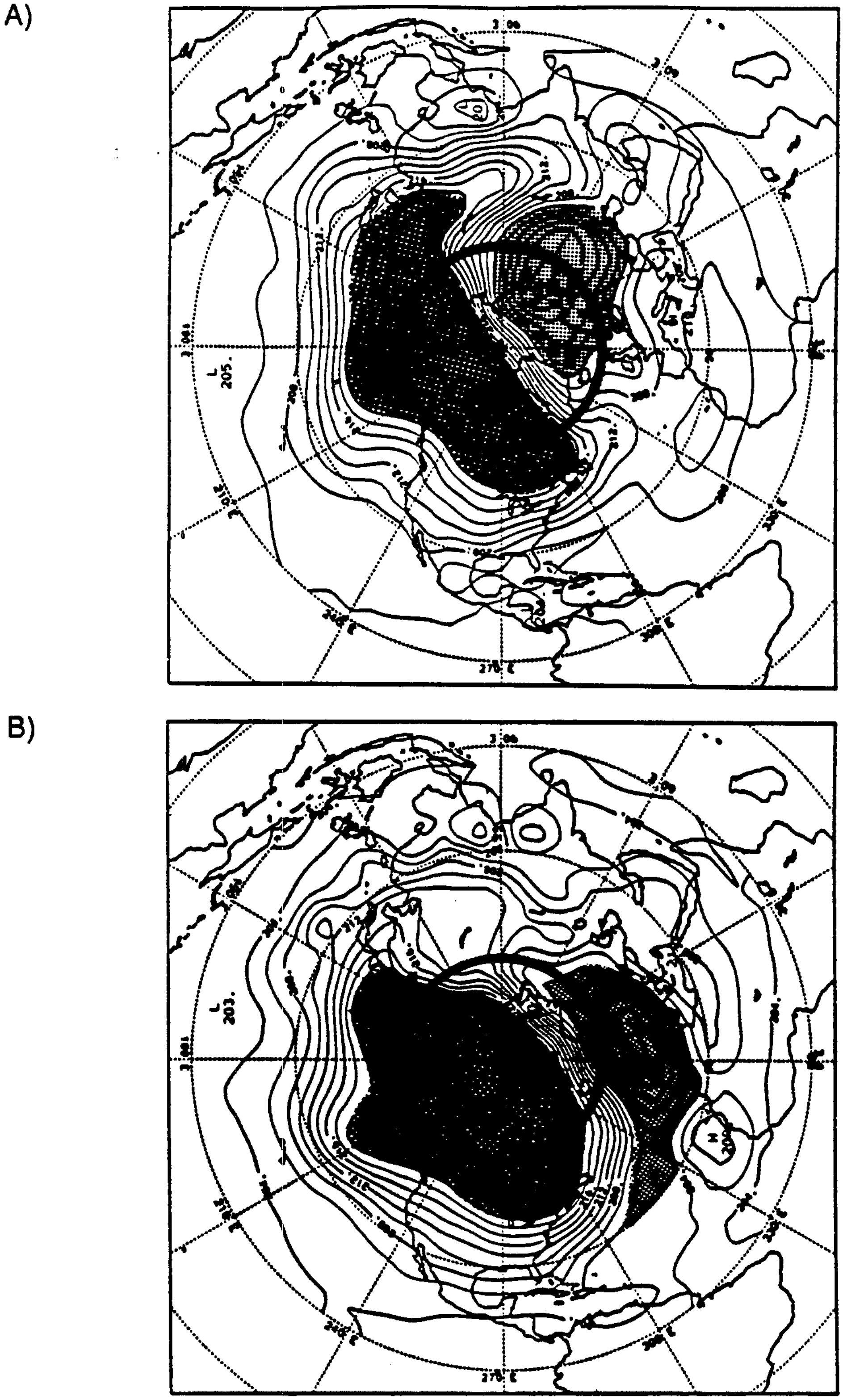

Figure 4.30: NMC 50 mb Temperature (K)Field for A) 12Z Jan 20 1987, and B)12Z Jan 25 1987 with regions colder than 204 K shaded and regions warmer than 220 K hatched; and NMC 50 mb Geopotential Height (GPM) Field for C) 12Z Jan 20 1987, and D) 12Z Jan 25 1987.

C)

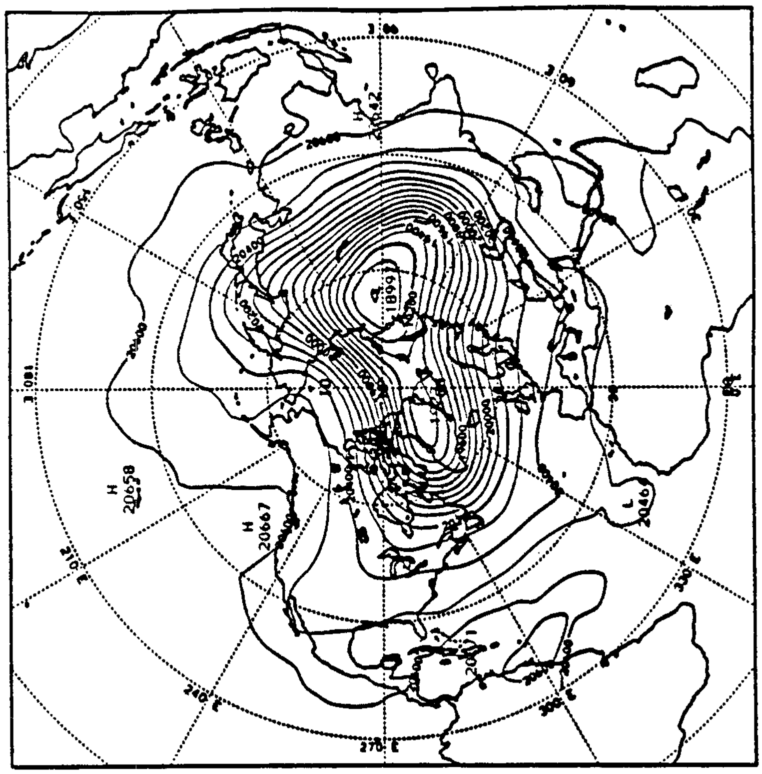
H
20658
H
20667
L
20461
H
20642
20000
210 E
240 E
270 E
300 E
330 E

D)

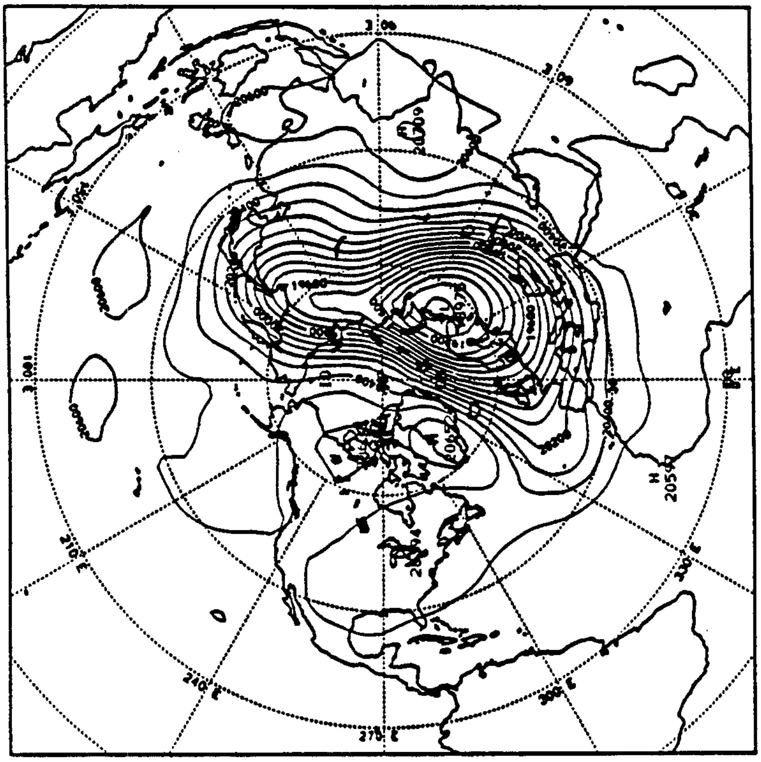
H
2054
20000
19800
210 E
240 E
270 E
300 E
330 E

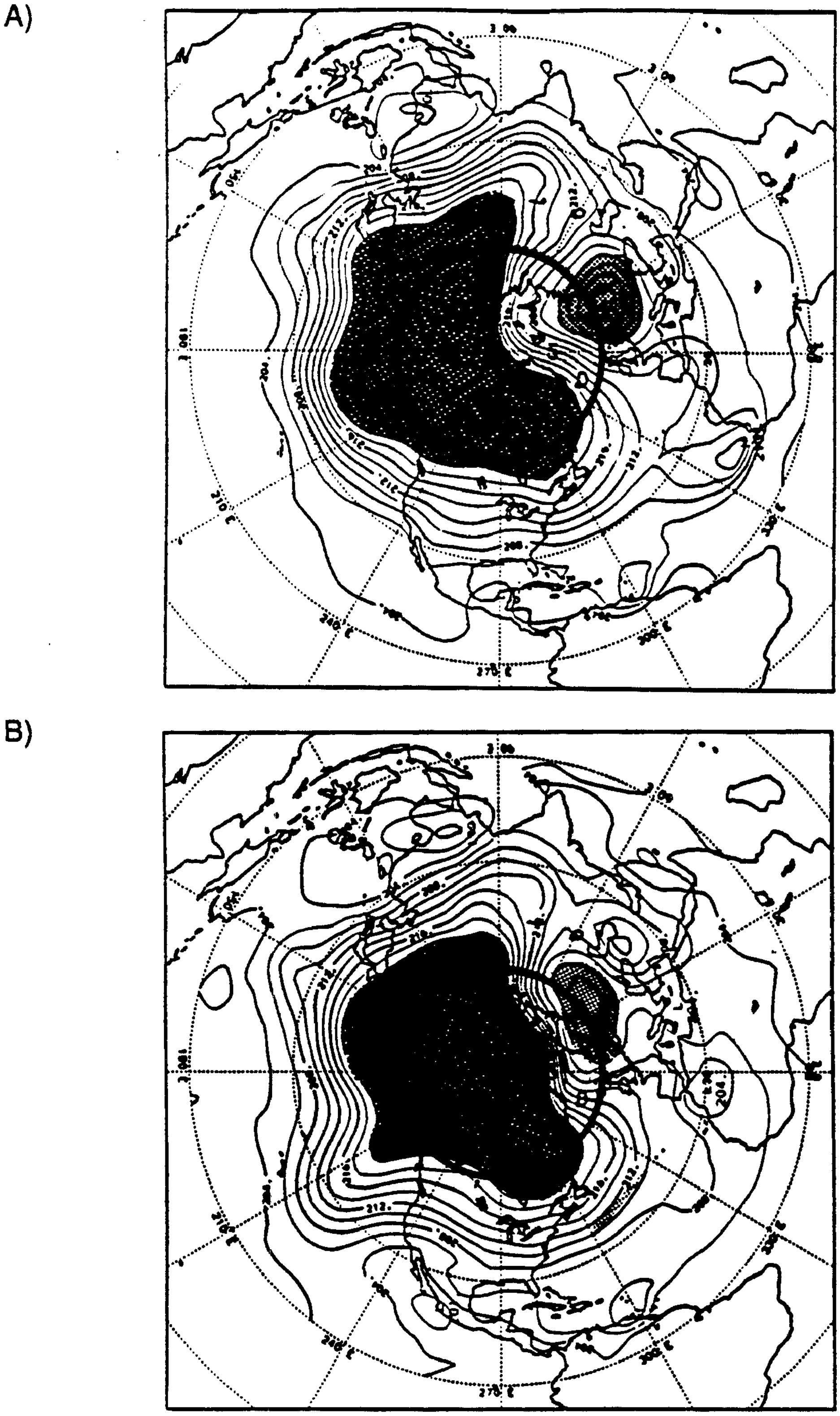

Figure 4.31: NMC 50 mb Temperature (K)Field for A) 12Z Feb 3 1987, and B)12Z Feb 5 1987 with regions colder than 204 K shaded and regions warmer than 220 K hatched; and NMC 50 mb Geopotential Height (GPM) Field for C) 12Z Feb 3 1987, and D) 12Z Feb 5 1987.

C)

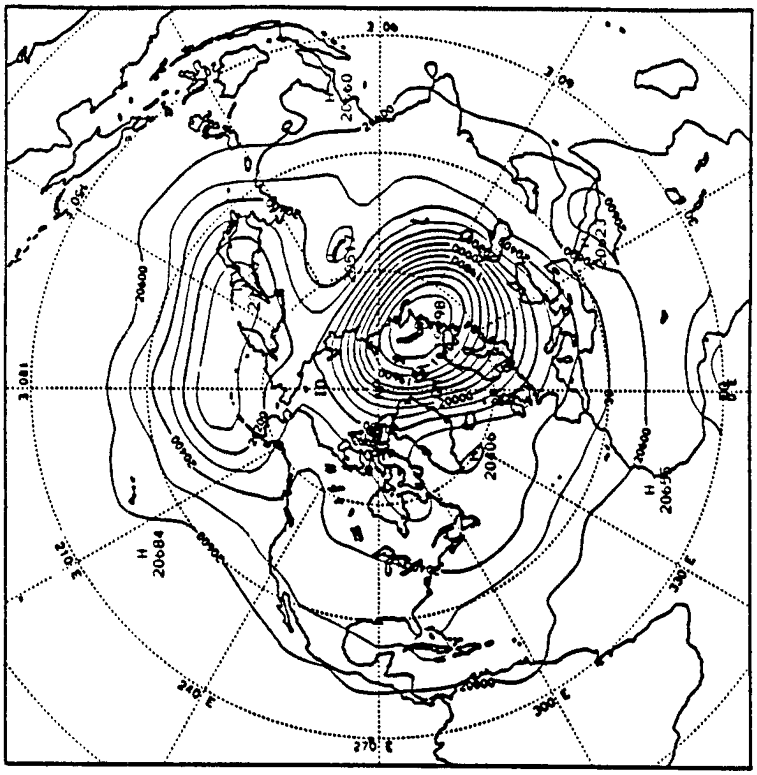
H
20684
H
20656
20400
20600
20806
20600
H
20560
210 E
240 E
270 E
300 E
330 E

D)

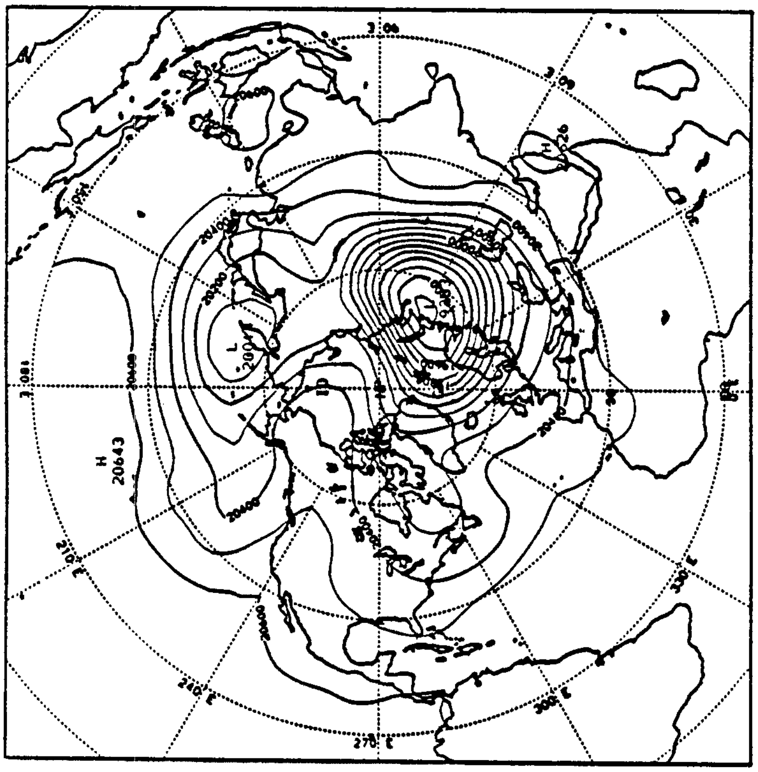
H
20643
L
20047
20400
20200
20400
20600
210 E
240 E
270 E
300 E
330 E

Figures 2.29 - 2.31 are northern hemispheric projections of NMC 50 mb temperature and geopotential height fields. These are presented to show a qualitative view of the statospheric warming and simulatneous breakdown of the zonal polar vortex. Figure 4.29 shows the temperature and geopotential height fields before both warming events (10 Jan 87) and one month later, after both (10 Feb 87). Figure 4.29a shows a cold pool centered over the Norwegian Sea with warmest regions along 50°N in the Eastern Hemisphere. The highlighted latitude circle shows 60°N latitude, hatched regions indicate temperature greater than 220 K and shaded regions temperature less than 204 K. One month later, Figure 4.29b shows the warmest temperatures over the polar region, decreasing with decreasing latitude. The winter circumpolar westerly vortex is clearly evident in Figure 4.29c on Jan 10, but by Feb 10, Figure 4.29d shows it broken down into a zonal wave number 2 pattern along 60°N.

The 21-25 Jan warming is shown in Figure 4.30 using 50 mb NMC data. The cold shaded region in figure 4.30a extends well north of the 60°N latitude line on Jan 20. Five days later, Figure 4.30b shows extensive warming north of 60°N, the north pole has increased form 216 K to 232 K and the shaded region is almost completely south of 60°N. The geopotential height fields, Figures 4.30c and d, show a zonal wave number 2 pattern move off the pole. The resulting weaker westerly winds, below the critical velocity, may have allowed energy from planetary waves to propagate vertically into the stratosphere resulting in the warming.

The 3-6 Feb warming is shown in Figure 4.31. Similar to the previous warming Figures 4.31 a and b show the shaded cold region pushed south of 60°N with the hatched warm region covering almost the entire polar region. The north pole increased from 222 K to 238 K with a 241 K maximum just to the south along 90°E. The geopotential height fields, Figures 4.31c and d continue to indicate weak westerly flow over the polar regions.

In conclusion, the warming observed by the MSU brightness temperature data was observed by both ECMWF data and at higher levels by NMC data. The structure of the NMC temperature fields and geopotential height fields indicates this to be a major stratospheric warming event.

CHAPTER 5

SUMMARY, CONCLUSION, AND RECOMMENDATIONS

5.1 REVIEW OF OBJECTIVES AND METHODOLOGY

This research project was inspired by a desire to expand the application of passive microwave remote sensing information to broader research topics in the atmospheric sciences. The Microwave Sounding Unit has been collecting radiometric data on a global basis since 1978 and thus offers a tremendous source of information on the thermal structure of the atmosphere. Another advantage of MSU data, and one not ot be overlooked, is the fact that the data now exists on a six year time series at NCAR (which was not available at the time of this research). Microwave remote sensing instruments with better vertical and horizontal resolution, such as the Advanced Microwave Sounding Unit, may not provide data for research until the mid-1990s (Murphy, 1987), and it is highly desirable to evaluate the utility of the existing data. Two objectives of this research were to develop MSU global brightness temperature fields and ECMWF complementary fields for comparison. A major portion of time spent on this project was devoted to developing programming techniques designed to take MSU thermal data from storage files and create global graphics output. Several of the programs used are contained in appendices, including a section on programming methods used to produce the ECMWF field. These programs are now available to manipulate the larger body of available MSU data, and hopefully these microwave data can be applied to research interests more readily. However, several details need to be considered by anyone desiring to work with MSU brightness temperature data sets. The enormous amount of data contained in MSU files requires large storage capabilities, not only storage for brightness temperature values (≈5.5 million for a 6-week time period) but also storage for graphics metacode files. Tape reading and limb-correction can be CPU consuming (expensive) when working with a data set covering an extensive period of time. This being the case it is best to create limb-corrected files, store them on magnetic tape or internal storage devices and perform desired processing from the these files.

The processing technique used in this research was sufficient for viewing the data on a global basis. Using 2.5^{o}-grid averaging without any weighting factor resolved global circulation features, as shown throughout Chapter 4. Since brightness temperature values are specified to the hundreth of a degree latitude/longitde an averaging scheme can be developed to research phenomenon on almost any meteorological scale. The nature of MSU's polar-orbiter satellite platform should also be considered before approaching a research project. Satellite overlap and underlap near the poles and equator were not dealt with in this project, since it concentrated on a global scale analyses and involved time-averaging over a six-week time period. Using data from a polar-orbiter platform also requires an awareness of satellite time passes, especially in research of a smaller spatial or temporal nature.

Proper attention should also be paid to limb-correction technique. The method used in this project was developed by Smith *et. al.*, 1974. Limb-corrected brightness temperature values from MSU Channel 1 (the surface channel) contained errors that made it unusable. None of the research in this study used information from this channel although it is desirable to incorporate this information to correct for the noted surface influences in Channel 2. Further study into this method is needed before proceeding on any project that requires limb-corrected brightness temperatures from Channel 1.

The second major objective of this project was to produce global fields of temperature, zonal wind, geopotential height, and streamfunction using the ECMWF data sets for the purpose of comparison with MSU fields. The CCM processor proved to be a system having a wide range of capabilities for manipulating ECMWF analysis data sets into user-specified fields. A user's guide and tutorial are available from the Climate and Global Dynamics Division at NCAR. The ability of the CCM processor to time-average user-specified days allowed producing ECMWF fields that time-corresponded to the MSU data set available for this study (8 Jan-18 Feb 87). The CCM processor capabilities combined with ten years of ECMWF analyses data provide unique system that can be applied to weather and climate research.

The third objective of this study was to determine the extent to which MSU brightness temperature fields relate to observed atmospheric circulations. This was accomplished through a series of global and hemispheric comparisons of MSU Channels 2, 3, and 4 brightness temperature fields with ECMWF temperature, zonal wind, geopotential height, and streamfunction fields for two time-periods (8-31 Jan and 1-18 Feb 87). The thermal wind concept is primarily used to relate MSU meridional temperature gradients to ECMWF observed zonal wind, and geopotential thickness fields. This comparison is possible since MSU brightness temperature fields may be considered mean-layer temperature fields. Jet stream core location is related to a reversal of meridional temperature gradient which may also be estimated from the MSU brightness temperature anomaly fields. Thermal wind theory also predicts MSU brightness temperature fields to be equivalent to fields of streamfunction thickness. These relations were observed through visual pattern comparison and random numerical calculations in this study. ECMWF and NMC data were combined to provide a record of temperature and zonal wind in the lower stratosphere in an effort to determine if the warming shown by MSU Channels 3 and 4 could be the result of a sudden-stratospheric warming.

5.2 SUMMARY OF RESULTS

The objectives of developing MSU brightness temperature fields and producing complementary ECMWF data sets were met. NCAR graphics routines sucessfully produced global and hemispheric projections of MSU brightness temperature fields and the CCM processor allowed for the production of complementary fields from ECMWF data sets. Results of the comparative study are summarized below:

- MSU Channel 2 brightness temperature most closely compared to the 500 mb level temperature field as shown by visual pattern comparison with ECMWF analyses. Likewise, Channels 3 and 4 most closely compared with the 300 and 100 mb ECMWF temperature fields.

- MSU Channel 2 meridional temperature gradients are highly related to ECMWF 300 mb geostrophic zonal wind. Regions of strongest MSU meridional temperature gradients correspond to jet stream locations. The coefficient of determination from a simple regression on 15 random numerical calculations (R^2=.921) shows a highly linear relation.

- Analysis of MSU brightness temperature anomaly fields for detecting temperature gradient reversals showed it to be be a poor predictor of jet core location as indicated by ECMWF zonal wind cross-sections. Jet core altitude results were slightly improved (30% closer in NH and 24% closer in SH cases) using Channel 2 as 500 mb temperature instead of 700 mb. The anomaly fields showed a striking difference between predicted NH and SH jet core altitude. ECMWF showed the jet core 27 mb higher on average in the SH, where the anomaly fields showed an average difference of 103 mb.

The brightness temperature anomaly fields consistantly predicted the north-south position of the jet core poleward of the ECMWF location, in both hemisphere. ECMWF showed average jet core locations of 32°N and 43°S for the locations in Table 4.3, where the anomaly fields predicted 38°N and 46°S. The anomaly fields do not appear to a show better correlation over land than ocean. Further comparison of the MSU data and the ECMWF analysis is recommended to explore these differences in more detail.

- MSU Channel 2 meridional temperature gradients highly relate to ECMWF 850-300 mb geopotential thickness gradients. This is seen in both visual pattern comparison and random numerical calculations. MSU meridional temperatue gradients were compared to a 'calculated' meridional temperature from ECMWF geopotential thickness gradients using Equation 4.9. A simple regression performed on the scattergram of Table 4.4 shows the coefficient of determination equal to .922.

- Likewise, MSU Channel 2 brightness temperature is highly related to ECMWF 850-300 mb geopotential thickness. Results from both hemispheres show strong pattern correlation. MSU brightness temperatures were compared to a 'calcluated' temperature from ECMWF geopotential thickness using Equation 4.10. A regression of 15 random numerical calculations show a coefficient of determination equal to .952. In a similar manner, MSU Channel 4 brightness temperature relates to 200-100 mb ECMWF geopotential thickness. Calculations at the same locations show a coefficient of determination equal to .989.

- MSU Channel 2 brightness temperature and brightness temperature gradient is related to ECMWF 1000-300 mb streamfunction difference and stramfunction thickness gradient. This is verified by the visual pattern comparison presented in Chapter 4 for both hemispheres and both time periods (8-31 Jan and 1-18 Feb).

- MSU Channels 3 and 4 have the capability of detecting lower stratospheric phenomenon. The warming observed poleward of 50$^{\mathrm{O}}$N by MSU was detected in both ECMWF data and at higher levels by NMC data. The simultaneous breakdown of the zonal polar vortex with extensive stratospheric warming in the polar region, as seen in the NMC data, is strong indication that at a major sudden-stratospheric warming occured and was detected by the MSU.

5.3 GENERAL CONCLUSIONS AND RECOMMENDATIONS

The broad implications of this study reveal the potential a microwave sounding instrument has for observing the atmospheric general circulation.

Possible applications exist in both global weather and climate studies. Global temperature trends can be observed and studied over long or short-range time periods. The MSU may provide an initialization or verification tool for weather and climate models in regions of sparse ground truth such as over oceans and in the southern hemisphere. To further study the relation between MSU brightness temperature and atmospheric general circulation, a numerical correlation method should be applied to better quantify the relations shown in this study by visual pattern comparisons. This is now possible since both the MSU and ECMWF data sets may be obtained in numerical form (ECMWF data is in packed format at NCAR).

In the future, mid-1990s, the Advanced Microwave Sounding Unit (AMSU) is proposed to become operational. The advantage of this new instrument over the MSU will be greater vertical resolution, 12 frequencies in the oxygen band (50-60 GHz) to profile temperature (Murphy, 1987). Weighting function curves will have sharper peaks and narrower ranges. A greater number of channels will allow more comparisons from different atmospheric levels and better comparisons because of increased vertical resolution. For example the brightness temperature anomaly fields in this study were produced having only three measurements in the vertical (linearly interpolated on a log scale inbetween). Having 12 measurements in the vertical should certainly improve jet stream core location predictions.

This study is a beginning effort to determine how MSU brightness temperature fields relate to atmospheric general circulation. Results show that further research is justified in an effort to better quantify these relations.

REFERENCES

Chandrasekhar, S., 1960: *Radiative Transfer.* Dover Publications Inc., New York, 393 pp.

Clare, F., L. Henderson, S. Henderson, B. Horner-Miller, J. Humbrecht, and D. Kennison, 1986: The NCAR GKS-Compatible Graphics System. *NCAR Technical Note NCAR/TN-267+1A.*

Dias, M.A., 1987: Introduction to the CCM Modular Processor (Version PROC02). *NCAR Technical Note NCAR/TN-289+1A.*

Goody, R. M., and J. C. G. Walker, 1972: *Atmospheres*, Prentice-Hall, Englewood Cliffs, N.J.

Grody, N. C., and W. C. Shen, 1982: Observations of Hurricane David (1979) using the microwave sounding unit. *NOAA Tech. Rep. NESS 88.*

Grody, N. C., 1983: Severe Storm Observations Using the Microwave Sounding Unit. *Journal of Climate and Applied Meteorology*, **22**, 609-625.

Holton, J.R., 1979: *An Introduction to Dynamic Meteorology.* Academic Press, Inc., New York, New York.

Kidder, S.Q., 1979: *Determination of Tropical Cyclone Surface Pressure and Winds from Satellite Microwave Data.* Colorado State University Department of Atmospheric Science Paper No. 307.

Kidwell, K.B., 1986: NOAA Polar Oribiter Data (TIROS-N, NOAA-6, NOAA-7, NOAA-8, NOAA-9, NOAA-10) Users Guide. U.S. Department of Commerce.

Labitzke, K., 1977: Interannual variability of the winter stratosphere in northern hemisphere. *Mon Weather Rev.*, **105**, 762-770.

Leovy, C. D., and P. J. Webster, 1976: Stratospheric Long Waves: Comparison of Thermal Structure in the Northern and Southern Hemispheres. *J. Atmos. Sci.*, **33**, 1624-1638.

Liou, K., 1980: *An Introduction to Atmospheric Radiation.* Academic Press, Inc., New York, New York.

Lubich, D. A., and R. M. Zehr, 1988: The Use of Polar Orbiter Data in Tropical Weather System Analysis, *Third Conf. on Satellite Meteorology and Oceanography*, Jan.31-Feb. 5, 1988, Anaheim, Ca.

Mahlman, J., 1969: Heat balance and mean meridional circulations in the polar stratosphere during the sudden stratospheric warming of January 1958. *Mon. Weather Rev.*, **97**, 534-539.

Murphy, R. 1987: High-Resolution Multifrequency Microwave Radiometer. Earth Observing System Reports, Volume IIe, NASA.

Njoku, E. G., 1982: Passive Microwave Remote Sensing of the Earth from Space--A Review. *Proceeding of the IEEE*, **70**, 728-750.

Planet, W. G., 1988: Data Extraction and Calibration of TIROS-N/NOAA Radiometers. *NOAA Technical Memorandum NESS 107 - Rev. 1.*

Prabhakara, C., H. D. Chang, and A. T. C. Chang, 1982: Remote sensing of precipitable water over the oceans from Nimbus 7 microwave measurements. *J. Applied Meteor.*, **21**, 59-68.

Prabhakara, C., I. Wang, A. T. C. Chang, andP. Gloersen, 1983: A statistical examination of Nimbus-7 SMMR data and remote sensing of sea surface temperature, liquid water content in the atmosphere and surface wind speed. *J. Climate and Applied Meteor.*, 22, 2023-2037.

Riehl, H., 1962: *Jet Streams of the Atmosphere.* Colorado State University Department of Atmospheric Science Technical Paper Number 32.

Schoeberl, M. L., 1978: Stratospheric Warmings: Observation and Theory. *Reviews of Geophysics and Space Physics*, **16**, 521-538.

Schwalb, A., 1978: The TIROS-N/NOAA A-G Satellite Series. *NOAA Technical Memorandum NESS 95.*

Sellers, W. D., 1965: *Physical Climatology.* The University of Chicago Press, Chicago, Illinois.

Smith, W. L., and H. M. Woolf, P. G. Abel,C. M. Hayden, M. Chalfant, and N. C. Grody, 1974: NIMBUS-5 Sounder Data Processing System, Part 1: Measurement Characteristics and Data Reduction Procedures. *NOAA Technical Memorandum NESS 57.*

Smith, W. L., and H. M. Woolf, C. M. Hayden, D. Q. Wark, L. M. McMillin, 1979: The TIROS-N Operational Vertical Sounder. *Bull. Am. Meteorol. Soc.*, **60**, 1177-1187.

Schmugge, T. J., 1985: *Remote Sensing of soil moisture.* Hydrological Forecasting, M. G. Anderson and T. P. Burt, Eds., Wiley, New York.

Staelin, D. H., 1969: Passive Remote Sensing at Microwave Wavelengths. *Proceedings of the IEEE*, **57**, NO. 4, 427-439.

Trenberth, K. E., and J. G. Olson, 1988: ECMWF Global Analyses 1979-1986: Circulation Statistics and Data Evaluation. *NCAR Tech. Note NCAR/ TN+300STR.*

Tsang, L., J. A. Kong, and R. T. Shin, 1985: *Theory of Microwave Remote Sensing.* John Wiley & Sons, Inc., New York, New York.

Ulaby, F. T., R. K. Moore, and A. K. Fung 1981: *Microwave Remote Sensing: Active and Passive.* Volume 1, Addison-Wesley, Reading, MA.

Wallace, J. M., and P. V. Hobbs, 1977: *Atmospheric Science: An Introductory Survey.* Academic Press Inc., New York, New York.

Wang, J. R., and T. J. Schmuggee, 1980: An empirical model for the complex dielectric permittivity of soils aas a function of water content. *IEEE Trans. Geosci. and Remote Sensing*, **GE-18**, 288-295.

Wolski, R. J., 1987: CCM Modular Processor Users' Guide (Version PROC02). *NCAR Tech. Note NCAR/TN-290+1A.*

Appendix A

FORTRAN - 77 PROGRAM MSUTAPE

This program reads MSU radiometric data in the form of raw voltage counts and converts it to a brightness temperature value. The MSU data tapes used in this study were obtained from NOAA-NEDSIS with the MSU data previously seperated from other TOVS instrument's data. Data is stored in the TOVS format shown in Table 2.2. The calibration technique used in program MSUTAPE is discussed in Section 2.4.2, and Figure 2.13a shows a sample output brightness temperature file. This program was run on a VAX 750 computer owned by the Atmospheric Science Department at Colorado State University.

```
      PROGRAM MSUTAPE
C
C       PROGRAM TO READ MSU DATA FROM TAPE
C
      REAL LAT(300,11),LON(300,11),CH(300,4,11)
      REAL*4 SCALE(4),COUNT,C1,C2,NORM(4,4),SAT_WAVEN(8,4),SLOPE(4),
     1     XINT(4),WAVEN(4)
      INTEGER*2 ICHAN,WORD
      INTEGER*4 ITEMP
      CHARACTER*20 COLFIL(300)
      CHARACTER CMON*2,ATYPE*4,BTIME*4,ETIME*4,FNAME*12,
     +          CY*2,CM*2,CD*2,ADATE*6,HEADER*80
      CHARACTER*6 SAT(8)
      BYTE IVAL(2),MBYTE,CHECK(4)
      LOGICAL REWIND,NSADJUST,EWADJUST

      DATA SAT/'TIROS ','NOAA6 ','      ','NOAA7 ','      ','NOAA8 ',
     +         'NOAA9 ','NOAA10'/
      DATA ((SAT_WAVEN(I,J),J=1,4),I=1,8) /1.6599,1.7734,1.6488,1.7385,
     1   1.6599,1.7734,1.6488,1.7385,
     1   0.,0.,0.,0.,
     1   1.6779,1.7927,1.8337,1.9331,
     1   0.,0.,0.,0.,
     1   1.6779,1.7927,1.8334,1.9331,
     1   1.6779,1.7927,1.8334,1.9331,
     1   1.6779,1.7927,1.8334,1.9331/
```

```
      EQUIVALENCE (WORD,IVAL)
      COMMON /INBYTE/ MBYTE(440)

      CALL TAPE_DRIVE (ICHAN)

      NSADJUST = .FALSE.
      EWADJUST = .FALSE.
C
C     LOOP THROUGH MSUTAPE TO PROCESS CONSECUTIVE FILES
C
      WRITE (6,*) 'ENTER NUMBER OF FILES TO PROCESS'
      READ (5,*) NFILE
C     COLLECT OUTPUT FILE NAMES IN FILE.COL
      OPEN (UNIT=11,FILE='FILE.COL',STATUS='NEW')

      DO 100 IFILE = 1,NFILE

C              READ TBM HEADER
C
      CALL MTREAD (ICHAN,MBYTE,122,ISTAT,IACTLN)
      DECODE(60,1,MBYTE) ATYPE,IDATE,BTIME,ETIME
    1 FORMAT(34X,A4,5X,I5,2X,A4,2X,A4)
      CALL MDCON2(IDATE,IY,IM,ID,CMON)
      CY = CHAR ((IY/10)+48) // CHAR (MOD(IY,10)+48)
      CM = CHAR ((IM/10)+48) // CHAR (MOD(IM,10)+48)
      CD = CHAR ((ID/10)+48) // CHAR (MOD(ID,10)+48)
      ADATE = CY // CM // CD
      FNAME = 'M' // ADATE(2:6) // BTIME(1:2) // '.DAT'
      COLFIL(IFILE) = FNAME
      WRITE (11,2) COLFIL(IFILE)
    2 FORMAT(A)
      OPEN(UNIT=1,FILE=FNAME,STATUS='NEW',FORM='FORMATTED')

C                READ DATA SET HEADER
C
      CALL MTREAD (ICHAN,MBYTE,440,ISTAT,IACTLN)
      ID = MBYTE(1)
      ENCODE(41,3,HEADER) SAT(ID),ATYPE,ADATE,BTIME,ADATE,ETIME
   3  FORMAT(A6,1X,A4,5X,A6,A4,5X,A6,A4)

      DO I = 1,4
         WAVEN(I) = SAT_WAVEN(ID,I)
      ENDDO
      ILINE = 0
      IZ = 0
      WRITE(1,4)HEADER
    4 FORMAT(A80)
      WRITE(*,*)
      WRITE(*,5)HEADER(1:41)
    5 FORMAT(1X,'DATA SET FOR: ',A41)
      TYPE 6,SAT(ID)
    6 FORMAT(' USING CAL. COEF. FOR: ',A6)
      C1 = 1.1910659 * 10.**-5
      C2 = 1.438833
      SCALE(1) = 2.**22
      SCALE(2) = 2.**30
      SCALE(3) = 2.**44
      SCALE(4) = 2.**56
   10 CALL MTREAD (ICHAN,MBYTE,440,ISTAT,IACTLN)
         IF (ISTAT .EQ. '870'X) GOTO 99
         IERR = 0
         ILINE = ILINE+1
         N = 9
```

```
         DO I = 1,4
            CHECK(I) = MBYTE(N)
            N = N+1
         ENDDO
         CALL SCAN_QUALITY (CHECK,ILINE,FNAME,IERR)

C
C           EXTRACT CALIBRATION INFORMATION
C
C              SLOPE AND INTERCEPT COEFICIENTS
         N = 17
         DO I = 1,4
            CALL BYTCON(N,ITEMP)
            SLOPE(I) = FLOAT(ITEMP)/SCALE(2)
            N = N+4
            CALL BYTCON(N,ITEMP)
            XINT(I) = FLOAT(ITEMP)/SCALE(1)
            N = N+4
         ENDDO
C              NORMALIZATION COEFICIENTS
         N = 49
         DO K = 1,4
            DO J = 1,4
               CALL BYTCON(N,ITEMP)
               NORM(K,J) = FLOAT(ITEMP)/SCALE(J)
               N = N+4
            ENDDO
         ENDDO
C
C            EXTRACT LAT/LON PAIRS FOR SCAN

C
         N = 117
         DO I = 1,11
            IVAL(1) = MBYTE(N+1)
            IVAL(2) = MBYTE(N)
            LAT(ILINE,I) = FLOAT(WORD)/128.
            N = N+2
            IVAL(1) = MBYTE(N+1)
            IVAL(2) = MBYTE(N)
            LON(ILINE,I) = FLOAT(WORD)/128.
            N = N+2
         ENDDO
C
C               CHECK SCAN FOR ERROR FLAGS
C
         IF (IERR .NE. 0) THEN
            CALL BADSCAN (ILINE,CH)
            GOTO 10
         ENDIF
C
C              EXTRACT DATA
C
      N = 167
      IREC = 0
   20 IREC = IREC+1
      DO I = 1,4
         IVAL(1) = MBYTE(N+1)
         IVAL(2) = MBYTE(N)
         COUNT = FLOAT(WORD .AND. 4095)
         COUNT = NORM(I,1) + (NORM(I,2)*COUNT) + (NORM(I,3)*
     +           (COUNT**2)) + (NORM(I,4)*(COUNT**3))
         ENERGY = (SLOPE(I)*COUNT) + XINT(I)
         TERM1 = C2 * WAVEN(I)
```

```
          IF (ENERGY .EQ. 0) THEN
             TERM2 = 0.
          ELSE
             TERM2 = (C1 * (WAVEN(I)**3))/ENERGY
          ENDIF

          IF ((1 + TERM2) .LE. 1.0) THEN
             TEMP = 0.0
          ELSE
             TEMP = TERM1/ALOG(1 + TERM2)
          ENDIF

          CH (ILINE,I,IREC) = TEMP
          N = N+2
       ENDDO
       N = N+8
       IF (N .GT. 334) THEN
          GOTO 10
       ELSE
          GOTO 20
       ENDIF
C
C       WRITE DATA TO FILE (INVERT IF SATELLITE WAS ASCENDING)
C
   99  CONTINUE
       TYPE 7,FNAME
7      FORMAT(1X,'WRITING OUTPUT FILE TO: ',A12)
       IF (LAT(1,1) .LT. LAT(ILINE,1)) NSADJUST = .TRUE.
       IF (LON(1,1) .GT. LON(1,11)) EWADJUST = .TRUE.
       DO I = 1,ILINE
          N = I
          IF (NSADJUST) N = (ILINE+1) - I
          DO J = 1,11
             M = J
             IF (EWADJUST) M = 12-J
             WRITE(1,8)J,I,LAT(N,M),LON(N,M),(CH(N,K,M),K=1,4)
8            FORMAT(1X,I2,I4,F6.2,F7.2,6X,4F6.1)
          ENDDO
       ENDDO
       TYPE *,'NO. OF LINES EXTRACTED: ',ILINE
       CLOSE (UNIT=1)
100    CONTINUE
       CLOSE (UNIT=11)
       END

        SUBROUTINE SCAN_QUALITY (CHECK,ILINE,FNAME,IERROR)

        CHARACTER*15 ERRORS(3,8)
        CHARACTER*12 FNAME,LOGFILE
        BYTE BYTE_VAL,MASK(8),CHECK(4),BIT

DATA ((ERRORS(I,J),J=1,8),I=1,3) /'FATAL FLAG','DATA GAP','DATA FILL',
1             'DWELL','TIME ERROR','DACS','NO EARTH LOC','LOC DELTA',
1             'CALIBRATION','     ','     ','SCAN DISABLE',
1             'SCAN SEQUENCE','MIRROR SEQUENCE','     ','     ',
1             'BIT SYNC STATUS','SYNC ERROR','FRAME SYNC LOCK',
1             'FLYWHEELING','BIT SLIPPAGE','TIP PARITY',
1             'AUX. FRAME SYNC','     '/

DATA MASK /1,2,4,8,16,32,64,128/
IERROR = 0
```

```
      IF (ILINE .EQ. 1) THEN
         LOGFILE = FNAME
         IPTR = INDEX(LOGFILE,'.')
         LOGFILE(IPTR+1:IPTR+3) = 'LOG'
         OPEN (UNIT=2,FILE=LOGFILE,STATUS='NEW',FORM='FORMATTED')
         WRITE (2,1) FNAME
1        FORMAT(A)
      ENDIF

      DO N = 1,3
         BYTE_VAL = CHECK(N)
         DO I = 1,8
            IF (N .EQ. 2 .AND. (I .EQ. 2 .OR. I .EQ. 3)) GOTO 10
            IF (N .EQ. 2 .AND. (I .EQ. 7 .OR. I .EQ. 8)) GOTO 10
            IF (N .EQ. 3. AND. I .EQ. 8) GOTO 10
            BIT = BYTE_VAL .AND. MASK(I)
            IF (BIT .NE. 0) THEN
               TYPE 2,ILINE,ERRORS(N,I)
               WRITE (2,2) ILINE,ERRORS(N,I)
2              FORMAT(1X,'ERROR ON LINE: ',I4,1X,A15)
               IERROR = 1
            ENDIF
10       ENDDO
      ENDDO
      RETURN
      END

      SUBROUTINE BADSCAN (ILINE,MSU)

      REAL*4 MSU(300,11,4),XMISS(4)
      DATA XMISS /4*999.9/
      TYPE *,' EDITING SCAN AT: ',ILINE
      WRITE (2,*) ' EDITING SCAN AT: ',ILINE
      DO J = 1,11
         DO K = 1,4
            MSU(ILINE,J,K) = XMISS(K)
         ENDDO
      ENDDO
      RETURN
      END
```

Appendix B

FORTRAN - 77 PROGRAM MSULIMB

The limb-correction procedure used in this program was developed by Smith and Woolf, 1974. The procedure is discussed in more detail by Grody, 1983. It uses regression equations to compute nadir brightness temperature of a given channel based on a linear combinatioon of all channel measurements at a particular scan angle. Synthesized clear and cloudy brightness temperatures computed from a climatological set of atmospheres are used to derive the regression equations. The coefficients for NOAA-10, used by program MSULIMB in this study, are included at the end of this appendix. Figure 2.13b shows a sample limb-corrected brightness temperature file that correspond to the uncorrected file shown in Figure 2.13a.

```
      PROGRAM LIMB_CORRECTION
C           READ, LIMB-CORRECT, AND OUTPUT TOVS-MSU DATA
C
      CHARACTER*20 COLFIL(300),FNAMEL(300)
      CHARACTER*80 HEADER,FNAME,OUTNAME,DUMMY*20
      CHARACTER*2 ISAT
      COMMON /MSU/ DLAT(300,11),DLON(300,11),Z(300,11),V(300,11,4)
      COMMON /MLC/ V2(300,11,4)

      WRITE (6,*) 'ENTER NUMBER OF FILES TO BE LIMB CORRECTED'
      READ (5,*) NFILE

C     OBTAIN FILES TO BE LIMB CORRECTED FROM FILE.COL
C      AND STORE LIMB CORRECTED FILE NAMES IN FILEL.COL.

      OPEN (UNIT=11,FILE='FILE.COL',STATUS='OLD')
      OPEN (UNIT=12,FILE='FILEL.COL',STATUS='NEW')

      DO 30 IFILE = 1,NFILE
       READ (11,1) COLFIL(IFILE)
       DUMMY = COLFIL(IFILE)
       OPEN (UNIT=3,FILE=DUMMY,STATUS='OLD',FORM='FORMATTED')
         READ (3,1) HEADER
1         FORMAT(A)
```

```
          ISAT = HEADER(5:6)
10        READ(3,2,END=20) J,I,DLAT(I,J),DLON(I,J),(V(I,J,K),K=1,4)
2         FORMAT(1X,I2,I4,F6.2,F7.2,6X,4F6.1)
          NLINE = I
          GOTO 10
2         CLOSE (UNIT=3)

      CALL MSULCS (ISAT,NLINE)

C           OUTPUT ARRAY OF LIMB CORRECTED DATA
C
      FNAME = COLFIL(IFILE)
      IPTR = INDEX(FNAME,'.')
      OUTNAME(1:IPTR-1) = FNAME(1:IPTR-1)
      OUTNAME(IPTR:IPTR+4) = 'L.DAT'
      FNAMEL(IFILE) = OUTNAME
      WRITE(12,1) FNAMEL(IFILE)
C
C     STORE LIMB CORRECTED FILE ON MAGNETIC TAPE ON DRIVE MUA12:

      OPEN (UNIT=1,FILE='ROMULS$MUA12:'//OUTNAME,
     1         STATUS='NEW',FORM='FORMATTED')
      WRITE (1,1) HEADER
      DO I = 1,NLINE
         DO  J = 1,11
            WRITE (1,3) J,I,DLAT(I,J),DLON(I,J),(V2(I,J,K),K=1,4)
3           FORMAT(1X,I2,I4,F6.2,F7.2,6X,4F6.1)
         ENDDO
      ENDDO
      TYPE 4,OUTNAME
4      FORMAT(' OUTPUT LIMB CORRECTED DATA FILE IS: ',A16)
3     CONTINUE
      CLOSE (UNIT=1)
      CLOSE (UNIT=11)
      CLOSE (UNIT=12)
      END

      SUBROUTINE MSULCS (ISAT,NLINE)
C        This version corresponds to MSULCS of 20 May 1983 as used by
C        MCIDAS TOVS processing system

      CHARACTER*2 ISAT
      COMMON /MSU/ DLAT(300,11),DLON(300,11),Z(300,11),V(300,11,4)
      COMMON /MLC/ V2(300,11,4)
      COMMON /MSULIM/ COEFL(5,5,18),ASYM(3,11),ASZM(3,5)
      DIMENSION CMSU(4),XMISS(4)
      DIMENSION C(4),CRIT(6)
      DATA CRIT/236.,238.,240.,245.,250.,260./
      DATA NC/4/,NI/5/,INIT/0/
      DATA XMISS /4*999.9/

      CALL RMLCOEF (ISAT)
C           DO FOR EACH FOV
C
      DO ILINE = 1,NLINE
         DO IELE = 1,11
            DO K = 1,4
               CMSU(K) = V(ILINE,IELE,K)
            ENDDO
            DO K = 1,4
               IF (CMSU(K) .EQ. XMISS(K)) GOTO 20
            ENDDO
             L = IABS(IELE-6)
             LS = 1
```

```
             IF (CMSU(1) .LT. CRIT(L+1)) LS=2
             IF (LS.NE.LST) LS=3
             K = 3*L+LS
            DO J = 1,NC
               SUM=COEFL(NI,J,K)
                 DO I = 1,NC
                    SUM = SUM + COEFL(I,J,K)*CMSU(I)
                 ENDDO
               C(J)=SUM
            ENDDO
               DO J = 1,NC
                  CMSU(J) = CMSU(J)+C(J)
               ENDDO
C
C         STORE NEW VALUES IN ARRAY V2
20          DO K = 1,4
               V2(ILINE,IELE,K) = CMSU(K)
            ENDDO
         ENDDO
      ENDDO
      RETURN
      END

      SUBROUTINE RMLCOEF (ISAT)

      CHARACTER*80 FNAME
      CHARACTER*2 ISAT
      COMMON/MSULIM/CBUF(498)

      TYPE 1,ISAT
1      FORMAT(' READING COEFFICIENTS FOR NOAA',A2)
      IF (ISAT(2:2) .EQ. ' ') THEN



         FNAME = 'MCOEF'//ISAT(1:1)//'.DAT'
      ELSE
         FNAME = 'MCOEF'//ISAT(1:2)//'.DAT'
      ENDIF
      OPEN(2,FILE=FNAME,STATUS='OLD',ACCESS='SEQUENTIAL',READONLY)
C            READ COEFFICIENTS
      READ(2,100,END=10) CBUF
100   FORMAT(1X,9F8.4)
      CLOSE (2)
      RETURN
10    TYPE *,' ERROR IN RMLCOEF -- EOF ENCOUNTERED'
      STOP
      END
```

COEFFICIENTS FOR NOAA-10, USED IN MSULIMB

```
 -0.9268  1.5106 -0.4098  0.0728-43.6499 -0.0213  0.0191  0.0271 -0.0177
 -1.0023  0.0016  0.0133 -0.0411  0.0153  2.3994 -0.0025 -0.0195  0.0325
 -0.0167  1.7517  0.0038 -0.0099  0.0117 -0.0018 -0.7920 -1.0024  1.6211
 -0.4165  0.0624-45.5429 -0.0200  0.0191  0.0047 -0.0099  2.5237  0.0046
  0.0184 -0.0395  0.0141  0.4481 -0.0076 -0.0157  0.0461 -0.0204 -0.5433
 -0.0041 -0.0009 -0.0092  0.0049  1.8052 -1.0434  1.6671 -0.4152  0.0571
-47.4847 -0.0290  0.0260  0.0196 -0.0181  1.0938 -0.0005  0.0163 -0.0356
  0.0116  1.7217 -0.0001 -0.0256  0.0392 -0.0182  1.4341  0.0070 -0.0168
 -0.0034  0.0037  2.3386 -0.9205  1.5012 -0.3996  0.0682-43.9727 -0.0191
  0.0263  0.0172 -0.0158 -1.2232  0.0011  0.0252 -0.0492  0.0119  2.3148
 -0.0023 -0.0277  0.0433 -0.0228  2.6001  0.0159 -0.0291  0.0155 -0.0022
 -0.0263 -0.9978  1.6182 -0.4113  0.0597-46.1399 -0.0181  0.0266 -0.0047
 -0.0081  2.2235  0.0045  0.0301 -0.0484  0.0112  0.4686 -0.0083 -0.0233
  0.0583 -0.0274  0.2269 -0.0146 -0.0104 -0.0093  0.0052  6.5111 -1.0407
  1.6651 -0.4073  0.0528-48.1673 -0.0276  0.0344  0.0096 -0.0162  0.8116
 -0.0008  ).0283 -0.0441  0.0085  1.6858  0.0    -0.0338  0.0504 -0.0245
  2.2483  0.0063 -0.0233 -0.0069  0.0060  4.4755 -0.9006  1.4793 -0.3784
  0.0562-44.7704 -0.0127  0.0511 -0.0158 -0.0100 -1.8687  0.0     0.0621
 -0.0721 -0.0003  2.0022 -0.0019 -0.0544  0.0775 -0.0423  5.5604  0.0586
 -0.0975  0.0300 -0.0038  2.6470 -0.9864  1.6174 -0.4013  0.0514-47.9489
 -0.0132  0.0532 -0.0362 -0.0025  1.2826  0.0073  0.0642 -0.0743  0.0005
  0.3211 -0.0105 -0.0478  0.0963 -0.0494  2.9030 -0.0395 -0.0475 -0:0022
  0.0035 19.3197 -1.0331  1.6689 -0.3953  0.0422-50.1815 -0.0236  0.0634
 -0.0245 -0.0101 -0.0605 -0.0016  0.0650 -0.0677 -0.0037  1.4586  0.0005
 -0.0606  0.0858 -0.0446  5.0951  0.0194 -0.0636 -0.0136  0.0132 11.0341
 -0.8637  1.4512 -0.3686  0.0451-45.1978 -0.0013  0.0948 -0.0766  0.0023
 -2.7817 -0.0024  0.1313 -0.1177 -0.0195  1.2759 -0.0019 -0.1019  0.1405
 -0.0794 11.0196  0.1438 -0.2405  0.0660 -0.0089  8.0965 -0.9601  1.6334
 -0.4347  0.0587-49.8380 -0.0052  0.1034 -0.0987  0.0110 -0.1998  0.0040
  0.1325 -0.1225 -0.0175  0.3152 -0.0160 -0.0885  0.1636 -0.0905  7.8255
 -0.0571 -0.1324  0.0205 -0.0016 37.2787 -1.0215  1.6974 -0.4122  0.0374
-52.9309 -0.0174  0.1174 -0.0896  0.0036 -1.4556 -0.0034  0.1343 -0.1168
 -0.0215  1.0459  0.0005 -0.1082  0.1506 -0.0828 10.3966  0.0822 -0.1922
 -0.0153  0.0289 23.0101 -0.7972  1.4099 -0.3917  0.0439-43.6022  0.0177
  0.1617 -0.1814  0.0280 -3.1815 -0.0024  0.2401 -0.1919 -0.0479 -0.5407
 -0.0026 -0.1790  0.2537 -0.1492 19.5395  0.3104 -0.5419  0.1677 -0.0290
 18.3471 -0.9144  1.6604 -0.5239  0.0880-50.0130  0.0048  0.1872 -0.2103
  0.0399 -1.5365  0.0069  0.2354 -0.1991 -0.0435 -0.8069 -0.0249 -0.1489
  0.2758 -0.1639 15.3148 -0.0244 -0.3304  0.0845 -0.0149 59.1707 -1.0083
  1.7748 -0.4962  0.0525-55.4847 -0.0102  0.2081 -0.2060  0.0331 -2.7661
 -0.0027  0.2428 -0.1951 -0.0478 -0.4349  0.0003 -0.1856  0.2669 -0.1548
 18.6525  0.2846 -0.5880  0.0629  0.0410 45.0609 -0.6369  1.2593 -0.5037
  0.0978-30.9125  0.0613  0.2390 -0.3772  0.0927  1.3041 -0.0026  0.4314
 -0.3349 -0.0805 -4.4037 -0.0006 -0.3013  0.4911 -0.3086 29.6747  0.6918
 -1.2954  0.5527 -0.1403 34.5670 -0.7671  1.5644 -0.7343  0.2003-34.9743
  0.0276  0.3054 -0.4320  0.1164  2.0488  0.0106  0.4136 -0.3393 -0.0749
 -3.5728 -0.0358 -0.2312  0.4863 -0.3166 24.1373  0.1717 -0.8914  0.3573
 -0.0919 87.2581 -0.9874  1.9334 -0.8018  0.1691-49.1617 -0.0030  0.3591
 -0.4435  0.1120 -0.0016 -0.0020  0.4318 -0.3437 -0.0764 -3.6227 -0.0005
 -0.2997  0.5039 -0.3164 28.1553  0.9880 -2.0509  0.7081 -0.0959 92.5724
  0.4358  0.7288 -0.0466  0.3952  0.4060  0.0326  0.3220  0.2124  0.0060
  0.1146  0.1272  0.0105  0.0436  0.0578  0.0051  0.0     0.0     0.0
  0.0372  0.0010  0.0205  0.1236  0.0195  0.0344  0.2959  0.0505  0.0587
  0.4527  0.2227  0.0756  0.3305  0.4517  0.0776  0.2071  0.2579 -0.3120
 -0.0047  0.2226 -0.1308  0.0351  0.1771 -0.0889 -0.0123  0.1192 -0.0399
 -0.0011  0.0609 -0.0209
```

Appendix C

FORTRAN - 77 PROGRAM MSUMAP

Program MSUMAP is used to to produce the global MSU brightness temperature fields shown in Section 2.5.2. It calls the CONRAN (contouring objective analysis routine) and EZMAP (map projection routine) utilities, along with other graphics options. Subroutine MAPTRAN translates each latitude/longitude data point onto a u/v - plane, subroutine CONRAN performs a user specified contour analysis, and subroutine SUPMAP creates a map according to the desired projection. A linear interpolation scheme was called by CONRAN for all the MSU fields contoured in this study.

```
      PROGRAM MSUMAP
C **********************************************************************
C  THIS PROGRAM DRAWS AN EARTH-BASED PROJECTION MAP AND CONTOURS DATA
C  USING LINEAR INTERPOLATION AND NCAR GRAPHICS ROUTINES.

C  THE OUTPUT GRAPHIC CAN BE SEND TO A SCREEN (0) OR A PRINTER (1).
C
C  THE SUBROUTINE "SUPMAP" PLOTS THE MAP.
C
C  THE COORDINATE TRANSFORMATION IS HANDLED BY SUBROUTINE MAPTRN.
C
C  THE CONTOURING IS PERFORMED BY SUBROUTINE CONRAN.
C
C  THE NUMBER OF DATA POINTS MUST BE SPECIFICED BY THE USER BY RESETTING
C  THE PARAMETER VARABLE "MDATA" AND RECOMPILING THE PROGRAM.
C
C  THE INPUT FILES ARE MAPDRI.DAT: CONTAINING DRIVER FOR EARTH-BASED
C                                  PROJECTION MAP
C                       IRMAP.DAT: CONTAINING DRIVER FOR CONTOURING
C                                  IRREGULAR DATA FILE
C
C  THE OUPUT FILE IS ERROR.DAT: CONTAINING THE ERROR MESSAGE.
```

```
C
C  THE INPUT VARIABLES ARE THE FOLLOWS:
C     MAPDRI.DAT (UNIT=1) : XLOW,XROW,YBOW,YTOW = SIZE OF THE WINDOW
C                           JPRJ = TYPE OF MAP PROJECTION
C                           PLAT = SUB-POINT IN LATITUDE
C                           PLON = SUB-POINT IN LONGITUDE
C                           ROTA = ROTATING THE MAP
C                           PLM1,PLM2,PLM3.PLM4 = SIZE OF THE MAP
C                           JLTS = USE WITH PLM1,PLM2,PLM3 AND, PLM4
C                          JGRID = DRAWING LONGITUDE AND LATITUDE
C                           IOUT = TYPE OF OUTLINES
C                           IDOT = OUTLINES PATTERN
C                            SSA = HEIGHT OF THE SATELLITE IN TERMS OF
C                                  EARTH RADIUS FROM EARTH CENTER
C                          (FOR MORE SPECIFIC DEFINITATION SEE NCAR MANNULS)
C     IRDATA.DAT (UNIT=2) : FILENM = NAME OF THE INPUT DATA FILE
C                             ILOC = FLAG FOR DISPLAYING DATA POINT
C                                    (ANYTHING BUT ZERO)
C                             IDEF = FLAG FOR DETERMINING CONTOURING
C                                    (ANYTHING BUT ZERO)
C                         ARRAY(1) = HIGH
C                         ARRAY(2) = LOW
C                             CINC = CONTOUR INCREMENT
C                             IEXT = FLAG FOR DETERMINING EXTRAPOLATION
C                                    (ANYTHING BUT ZERO)
C     FILENM (UNIT=3)     : DLON(K) = LONGITUDINAL POSITION WITH ELEMENT K
C                           DLAT(K) = LATITUDINAL POSITION WITH ELEMENT K
C                             ZD(K) = DATA VALUES WITH ELEMENT K
C
C   THE OUTPUT VARIABLE IS :
C       ERROR.DAT (UNIT=20) : IERR = ERROR MESSAGE
C
C ***********************************************************************
      PARAMETER (MDATA=11000)
      DIMENSION ZD(MDATA),DLON(MDATA),DLAT(MDATA),XD(MDATA),YD(MDATA),
     1          WK(13*MDATA), IWK(31*MDATA), SCRARR(40**2), ARRAY(2),
     2          DNUM(MDATA)
      CHARACTER*30 FILENM
C
C  OPTION: SCREEN OF PRINTER
C
      WRITE (6,'(1X,A)') 'DISPLAY OR PRINTER (0/1)'
      READ (5,'(I1)') ICH
      IF (ICH .GT. 1) GOTO 10
C
C  OPTION: MAP ONLY OR MAP WITH DATA OVERLAYED
C
      WRITE (6,'(1X,A)') 'MAP ONLY OR MAP WITH OVERLAYING DATA (0/1)'
20    READ (5,'(I1)') IMAP
      IF (ICH .GT. 1) GOTO 20
C
C  INPUTTING DATA FROM MAPDRI.DAT AND IRDATA.DAT
C
      OPEN (UNIT=1,FILE='MAPDRI.DAT',STATUS='OLD')
        READ (1,*) XLOW,XROW,YBOW,YTOW
        READ (1,*) JPRJ
        READ (1,*) PLAT,PLON,ROTA
        READ (1,*) PLM1,PLM2,PLM3,PLM4
        READ (1,*) JLTS,JGRID,IOUT,IDOT
        READ (1,*) SSA
      CLOSE (UNIT=1)
      IF (IMAP.EQ.1) THEN
          OPEN (UNIT=2,FILE='IRDATA.DAT',STATUS='OLD')
           READ (2,*) FILENM
           READ (2,*) ILOC
           READ (2,*) IDEF,ARRAY(1),ARRAY(2),CINC
           READ (2,*) IEXT
          CLOSE (UNIT=2)
```

```
           OPEN (UNIT=3,FILE=FILENM,STATUS='OLD')
               DO 250 K=1,MDATA
               READ (3,*,END=260,ERR=270) DLAT(K),DLON(K),DNUM(K),ZD(K)
  250          CONTINUE
           NDP = MDATA
           GOTO 280
  260      NDP = K-1
           GOTO 280
  270      PRINT *, 'ERRORS DETECTED IN READING DATA FILE'
           GOTO 280
  280      CLOSE (UNIT=3)
        ENDIF

C  BEGIN PLOTTING ROUTINE
           CALL OPNGKS
           CALL GSCLIP(0)
C  INCREASE RESOLUTION FOR LASERPRINTER
           CALL MAPSTI('RE',1024)
           CALL MAPSTI('EL',1)
C  SET UP WORKING AREA ON THE SCREEN/PAPER
           CALL MAPPOS(XLOW,XROW,YBOW,YTOW)
C  FOR SATELLITE PROJECTION ONLY
           IF (IABS(JPRJ).EQ.7) THEN
             CALL MAPSTR('SA',SSA)
           ENDIF
           CALL SUPMAP (JPRJ,PLAT,PLON,ROTA,PLM1,PLM2,PLM3,PLM4,JLTS,
     1                 JGRID,IOUT,IDOT,IERR)
C
C  CALL MAPPING AND CONTOURING USING CONREC OR CONRAN
           IF (IMAP.EQ.1) THEN
             DO 400 IJ= 1,NDP
             CALL MAPTRN (DLAT(IJ),DLON(IJ),XD(IJ),YD(IJ))
400          CONTINUE
             IF (ILOC.EQ.0) THEN
               IF (IDEF.EQ.0) THEN
                 CALL CONOP1 ('DEF')
               ELSE
                 CALL CONOP1('ITP=LIN')
                 CALL CONOP1('LAB=ON')
               ENDIF
               IF (IEXT.EQ.0) THEN
                 CALL CONOP1 ('EXT=OFF')
               ELSE
                 CALL CONOP1 ('EXT=ON')
               ENDIF
             ELSE
                 CALL CONOP1('ITP=LIN')
                 CALL CONOP3('CHL=ON',ARRAY,2)
                 CALL CONOP3('CIL=ON',CINC,1)
             ENDIF
             CALL CONOP1 ('SCA=OFF')
             CALL CONRAN (XD,YD,ZD,NDP,WK,IWK,SCRARR)
          ENDIF
C
C  OUTPUT ERROR MESSAGE TO FILE
C
          OPEN (UNIT=20,FILE='ERROR.DAT',STATUS='UNKNOWN')
           WRITE (20,*) IERR
          CLOSE (UNIT=20)
          CALL FRAME
          CALL CLSGKS
      STOP
      END
C
      SUBROUTINE SUPMAP (JPRJ,PLAT,PLON,ROTA,PLM1,PLM2,PLM3,PLM4,JLTS,
     1                   JGRID,IOUT,IDOT,IERR)
```

```
C  CALL UP DIFFERENT MAP PROJECTIONS

C  STEREOGRAPHIC---1
      IF (IABS(JPRJ).EQ.1) THEN
        CALL MAPROJ('ST',PLAT,PLON,ROTA)
C  ORTHOGRAPHIC---2C
      ELSE IF (IABS(JPRJ).EQ.2) THEN
        CALL MAPROJ('OR',PLAT,PLON,ROTA)
C  LAMBERT CONFORMAL CONIC---3
      ELSE IF (IABS(JPRJ).EQ.3) THEN
        CALL MAPROJ('LC',PLAT,PLON,ROTA)
C  LAMBERT EQUAL-AREA---4
      ELSE IF (IABS(JPRJ).EQ.4) THEN
        CALL MAPROJ('LE',PLAT,PLON,ROTA)
C  GNOMONIC---5
      ELSE IF (IABS(JPRJ).EQ.5) THEN
        CALL MAPROJ('GN',PLAT,PLON,ROTA)
C  AZIMUTHAL EQUIDISTANT---6
      ELSE IF (IABS(JPRJ).EQ.6) THEN
        CALL MAPROJ('AE',PLAT,PLON,ROTA)
C  SATELLITE-VIEW---7
      ELSE IF (IABS(JPRJ).EQ.7) THEN
        CALL MAPROJ('SV',PLAT,PLON,ROTA)

C  CYLINDRICAL EQUIDISTANT---8
      ELSE IF (IABS(JPRJ).EQ.8) THEN
        CALL MAPROJ('CE',PLAT,PLON,ROTA)
C  MERCATOR---9
      ELSE IF (IABS(JPRJ).EQ.9) THEN
        CALL MAPROJ('ME',PLAT,PLON,ROTA)
C  MOLLWEIDE TYPE---10
      ELSE IF (IABS(JPRJ).EQ.10) THEN
        CALL MAPROJ('MO',PLAT,PLON,ROTA)

      ENDIF

C  CALL UP MAP-SETTING FOR BOUNDARYS' OPTIONS
C
      IF (IABS(JLTS).EQ.1) THEN
        CALL MAPSET ('MA',PLM1,PLM2,PLM3,PLM4)
      ELSE IF (IABS(JLTS).EQ.2) THEN
        CALL MAPSET ('CO',PLM1,PLM2,PLM3,PLM4)
      ELSE IF (IABS(JLTS).EQ.4) THEN
        CALL MAPSET ('AN',PLM1,PLM2,PLM3,PLM4)
      ELSE IF (IABS(JLTS).EQ.5) THEN
        CALL MAPSET ('PO',PLM1,PLM2,PLM3,PLM4)
      ENDIF
C
C  PUT MERIDIANS AND PARALLELS EVERY JGRID DEGREES IN DOTTED LINEC
      CALL MAPSTI('GR',JGRID)
      CALL MAPSTI('DA',3)
C
C  OUTLINES OPTIONS
C
      IF (IABS(IOUT).LE.1) THEN
        IF ((JPRJ.GE.0).AND.(IOUT.EQ.0)) THEN
          CALL MAPSTC ('OU','CO')
        ELSE IF ((JPRJ.GE.0).AND.(IABS(IOUT).EQ.1)) THEN
          CALL MAPSTC ('OU','US')
          CALL MAPSTC ('OU','CO')
        ELSE IF ((JPRJ.LT.0).AND.(IOUT.EQ.0)) THEN
          CALL MAPSTC ('OU','NO')
        ELSE IF ((JPRJ.LT.0).AND.(IABS(IOUT).EQ.1)) THEN
          CALL MAPSTC ('OU','US')
        ENDIF
```

```
      ELSE IF (IABS(IOUT).GT.1) THEN
        IF (IOUT.EQ.-2) THEN
          CALL MAPSTC ('OU','NO')
        ELSE IF (IOUT.EQ.2) THEN
          CALL MAPSTC ('OU','CO')
        ELSE IF (IOUT.EQ.3) THEN
          CALL MAPSTC ('OU','US')
        ELSE IF (IOUT.EQ.4) THEN
          CALL MAPSTC ('OU','PS')
        ELSE IF (IOUT.GE.5) THEN
          CALL MAPSTC ('OU','PO')
        ENDIF
      ENDIF
C
C   SOLID(0) ,DOTTED(1), DASHED(2), OR DOT-DASHED(3) OUTLINES
      IF (IDOT.EQ.0) THEN
        CALL MAPSTI ('DO',0)
      ELSE IF (IDOT.EQ.1) THEN
        CALL MAPSTI ('DO',1)

      ELSE IF (IDOT.EQ.2) THEN
        CALL MAPSTI ('DO',2)
      ELSE IF (IDOT.EQ.3) THEN
        CALL MAPSTI ('DO',3)
      ENDIF
C
C   CALL UP DRAWING ROUTINE
      CALL MAPDRW
C
C   CALL UP ERROR MESSAGE ROUTINE
      CALL MAPGTI('ER',IERR)

      RETURN
      END
```

Appendix D

PROGRAMMING METHODS USED TO PRODUCE ECMWF FIELDS

The CCM processor code will execute on either the CRAY-1 or the CRAY X-MP from a job deck maintained on the NCAR IBM 4381. The entire submission deck for the CCM processor can be summarized in two job steps. The first part is a CRAY job control language (JCL) deck used to acquire and run the processor code (Figure D.1). The second part consists of user modified input control parameters (ICPs), used to specify how you want the CCM processor to manipulate the ECMWF data sets. ICPs are used to select the desired history tapes, perform functions such as time averaging, and output graphics. An example of ICP coding is shown in Figure D.2

Input Control Parameters are organized under a "keyword" concept. Each keyword used in the processor code controls a function performed by the CCM processor. For example, the keyword TIMAVGA set to "YES" will cause the processor to perform a time average on the data selected as user specified case A. The desired time period is selected by calling history tapes and requesting specific days using the DAYA keyword. The keyword HPCINT set equal to ' T ', 500. , 5. tells the processor to plot and contour the 500 mb temperature field on a horizontal projection with a contour interval of five degrees farenheit. By setting the projection keyword to POLAR, northern and southern hemisphere polar sterographic projections may be obtained. An unabridged

1987). Several simple examples of ICP structure and usage are presented in the CCM tutorial (Dias, 1987).

```
===== JOB,JN=VR02,US=648835081140,OLM=100,T=250,*MS,CL=BG1.
===== ACCOUNT,AC=648835081140.
===== DISPOSE,DN=$OUT,DEFER,DC=ST,DF=CH,TEXT='FLNM=EZMAP,FLTY=OUT'.
===== *
===== *SET(G0='CHECK'H)
===== *THIS ALLOWS A CHECK RUN TO CHECK SYNTAX ETC OK; RUN EXP CLASS
===== * SET G1 TO NUMBER OF JOBSTEPS
===== SET(G1=1)
===== * INITIALIZE G2 AS A COUNTER OF STEPS
===== SET(G2=1)
===== * G3 IS NO. OF PLOT FRAMES IN CURRENT SET
===== SET(G3=0)
===== * INITIALIZE G4 AS THE PLOT DISPOSE GROUP
===== SET(G4=1)
===== PROC.
===== DISPLOT,STAT.
===== IF(G3.GT.0)THEN
=====   PRSIM,I=PINDEX,O=PLTD.
=====   REWIND,DN=$PLT.
=====   COPYD,I=$PLT,O=PLTD.
=====   REWIND,DN=PLTD.
=====   IF(&STAT.EQ.'ABORT')
=====      DISPOSE,DN=PLTD,DF=BI,MF=IO,DC=PT,NOWAIT,^
=====             TEXT='MDS,TITLE=PROC02 PLOTS - ABORT'.
=====   ELSE.
=====      DISPOSE,DN=PLTD,DF=BI,MF=IO,DC=PT,NOWAIT,^
=====              TEXT='MDS,TITLE=PROC02 PLOTS'.
=====   ENDIF.
=====   SET(G3=0)
===== ENDIF.
===== ENDPROC.
===== ACQUIRE,DN=ABPROC,PDN=CCMPROC02CXAB,MF=MS,TEXT='FLNM=/CCMPROC/02/CX/AB'.
===== ACQUIRE,DN=$DEBUG,PDN=CCMPROC02CXDB,MF=MS,TEXT='FLNM=/CCMPROC/02/CX/DB'.
===== LOOP.
=====   EXITLOOP(G2.GT.G1)
=====   ABPROC.
=====   SET(G2=G2+1)
===== ENDLOOP.
===== DISPLOT,'NORM'.
===== EXIT.
===== DUMPJOB.
===== DEBUG,BLOCKS,PAGES=50.
===== DISPLOT,'ABORT'.
===== EXIT.
===== DISPLOT,'ABORT'.
===== \EOF
```

Figure D.1: JCL Used to access the CCM Processor.

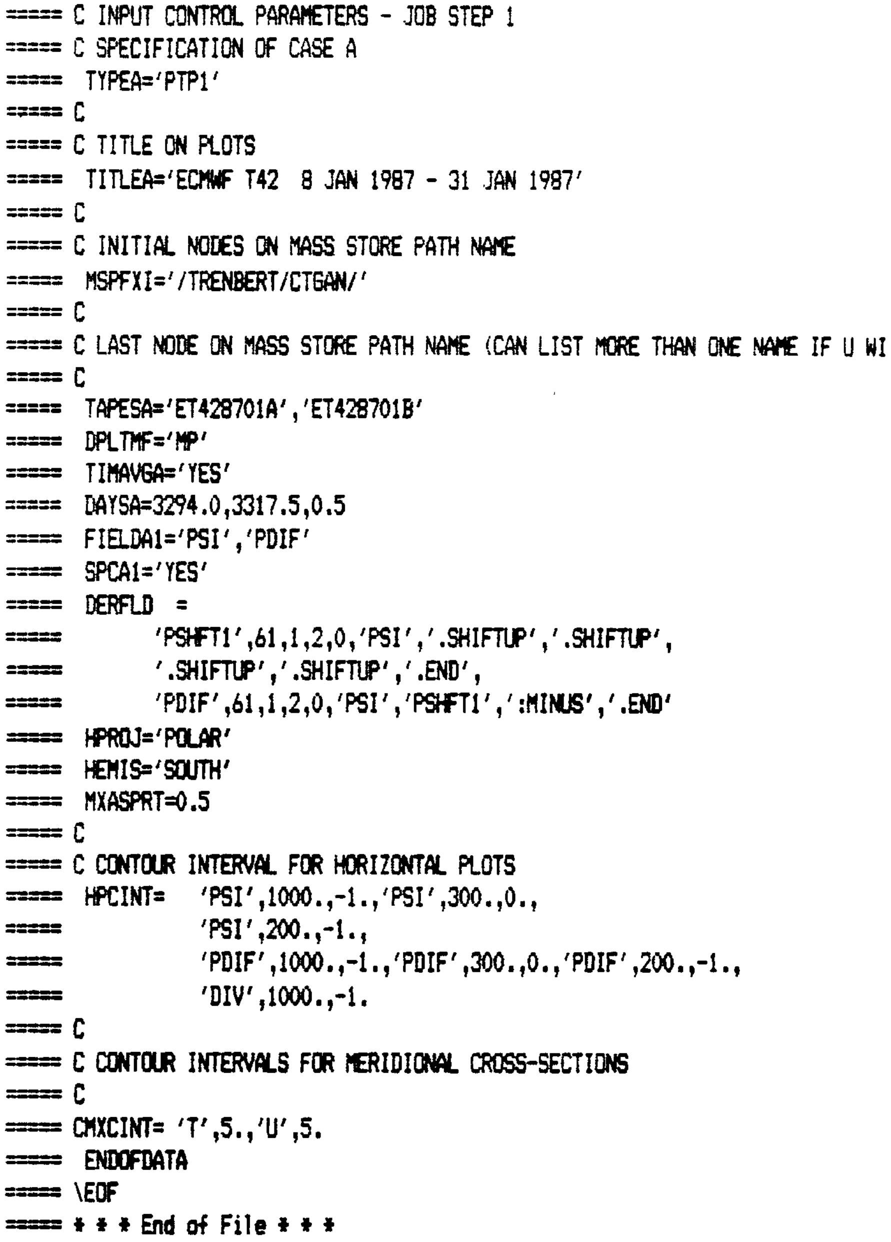

```
===== C INPUT CONTROL PARAMETERS - JOB STEP 1
===== C SPECIFICATION OF CASE A
=====  TYPEA='PTP1'
===== C
===== C TITLE ON PLOTS
=====  TITLEA='ECMWF T42  8 JAN 1987 - 31 JAN 1987'
===== C
===== C INITIAL NODES ON MASS STORE PATH NAME
=====  MSPFXI='/TRENBERT/CTGAN/'
===== C
===== C LAST NODE ON MASS STORE PATH NAME (CAN LIST MORE THAN ONE NAME IF U WI
===== C
=====  TAPESA='ET428701A','ET428701B'
=====  DPLTMF='MP'
=====  TIMAVGA='YES'
=====  DAYSA=3294.0,3317.5,0.5
=====  FIELDA1='PSI','PDIF'
=====  SPCA1='YES'
=====  DERFLD  =
=====        'PSHFT1',61,1,2,0,'PSI','.SHIFTUP','.SHIFTUP',
=====        '.SHIFTUP','.SHIFTUP','.END',
=====        'PDIF',61,1,2,0,'PSI','PSHFT1',':MINUS','.END'
=====  HPROJ='POLAR'
=====  HEMIS='SOUTH'
=====  MXASPRT=0.5
===== C
===== C CONTOUR INTERVAL FOR HORIZONTAL PLOTS
=====  HPCINT=   'PSI',1000.,-1.,'PSI',300.,0.,
=====            'PSI',200.,-1.,
=====            'PDIF',1000.,-1.,'PDIF',300.,0.,'PDIF',200.,-1.,
=====            'DIV',1000.,-1.
===== C
===== C CONTOUR INTERVALS FOR MERIDIONAL CROSS-SECTIONS
===== C
===== CMXCINT= 'T',5.,'U',5.
=====  ENDOFDATA
===== \EOF
===== * * * End of File * * *
```

Figure D.2: Sample Input Control Parameters, requests CCM processor to manipulate ECMWF data sets.